



Università degli Studi di Cagliari

PhD Degree

in Physics Department

FIS/03 Material Physics, XXXII Cycle

Title of the PhD Thesis

Photophysics and solar cell devices of two dimensional perovskites

PhD student

Qingqian Wang

Supervisor

Prof. Michele Saba

Coordinator of PhD school

Prof. Paolo Ruggerone

Contents

1. Introduction.....	3
1.1. Perovskite structure	4
1.2. Tunable bandgap (E_g)	4
1.3. High absorption coefficient.....	6
1.4. Charge recombination.....	7
1.5. Metal halide perovskite solar cells	10
1.6. Two dimensional hybrid perovskite	12
1.7. Lead free hybrid perovskite	16
1.8. Scope of this thesis	19
2. Synthesis and characterization	21
2.1. Perovskite thin film deposition	21
2.1.1. Spin-coating method.....	21
2.1.2. Vapor deposition.....	23
2.2. X-ray diffraction (XRD).....	23
2.3. Optical absorption	24
2.4. Time-resolved photoluminescence (TRPL).....	25
2.5. Pump-probe spectroscopy.....	27
3. Quasi-2D lead perovskite solar cells	29
3.1. Experimental section	30
3.1.1. Film deposition and device fabrication	30
3.1.2. Film characterizations	31
3.2. Results and discussion	33
3.2.1. Solar cells with different hole transport layers	33
3.2.2. Comparison of two deposition methods for mixed solvent	40
4. Photophysics of 2D tin perovskite.....	47
4.1. Experimental section	47
4.1.1. Synthesis of $BA_2MA_{n-1}Sn_nI_{3n+1}$ thin films	47

4.1.2. Film characterization.....	47
4.2. Results and discussion	49
4.2.1. Synthesis for single phase.....	49
4.2.2. Optical absorption and free energy	50
4.2.3. Ultrafast spectroscopy measurements	56
4.2.4. Conclusion	59
5. Summary and outlook.....	60
Supporting information to chapter 3	62
Supporting information to chapter 4	68
References.....	70

1. Introduction

The organic-inorganic trihalide perovskites have attracted much attention for their amazing achievements in the application for solar cells.[1-4] The power conversion efficiency (PCE) of perovskite solar cells has increased from 3.8% to more than 25% in the past ten years.[5-10] They have been proved to be great active materials for different optoelectronic devices.[11-17] With tunable bandgap, high absorption coefficient, long carrier lifetime and the low cost, easy processing procedures for thin film devices, perovskites are very potential for the next generation photovoltaics.[18-27]

In this thesis, I summarize the evolution of perovskite solar cells concisely and demonstrate the research results on two dimensional perovskites. First part shows the orientation and phase control about the 2D lead perovskite $\text{PEA}_2\text{MA}_4\text{Pb}_5\text{I}_{16}$, and novel hole transport layer that is beneficial for solar cell devices. The PCE of this perovskite solar cell achieves beyond 14%. Then ultrafast spectroscopy and pump-probe researches on 2D tin perovskite $\text{BA}_2\text{MA}_{n-1}\text{Sn}_n\text{I}_{3n+1}$ with $n=1$ and 2 are revealing the carrier behavior in these samples. Results show in $n=1$ sample, the carriers are mainly excitons whereas in $n=2$ sample, the carriers are mainly free carriers.

1.1. Perovskite structure

Perovskite, initially representing the metal oxide compound calcium titanium oxide (CaTiO_3), was named after Russian mineralogist Lev Perovski. Now, all the compounds with the formula ABX_3 could be called perovskites.[28] **Figure 1.1** shows the ideal structure. In this case, the crystal structure is perfectly cubic with B cation surrounded by six X anions, forming $[\text{BX}_6]^{4-}$ octahedron. Those octahedra connect each other in all three dimensional directions enclosing A cation in the centre of eight octahedra.

Two factors are necessary to maintain this unique structure. One is *Goldschmidt tolerance factor* t given by the equation below,

$$t = \frac{R_A + R_X}{\sqrt{2} (R_B + R_X)}$$

where R_A , R_B and R_X are radii of A, B and X ions respectively; the other is *octahedron factor*, $\mu = R_B/R_X$. Only when t ranging from 0.81 to 1.11 and μ ranging from 0.44 to 0.90 are both satisfied, the perovskite structure could be stable with little distortion. If t is valued in the range of 0.89-1.0, the structure will be cubic and lower t values lead to tetragonal or orthorhombic structures.[29-32]

For metal halide perovskites, X is selected from Cl^- , Br^- and I^- , while Cs^+ , methylammonium (CH_3NH_3^+ , MA) and formamidinium ($\text{HC}(\text{NH}_2)_2^+$, FA) could be used as A cations. Thus the B cation should be bivalent, it can be selected from 14 different elements (rare earth, alkaline earth and IV main group), most commonly are Pb^{2+} and Sn^{2+} .[33-37]

1.2. Tunable bandgap (E_g)

Since there are several different choices for A, B and X, by substituting or mixing of

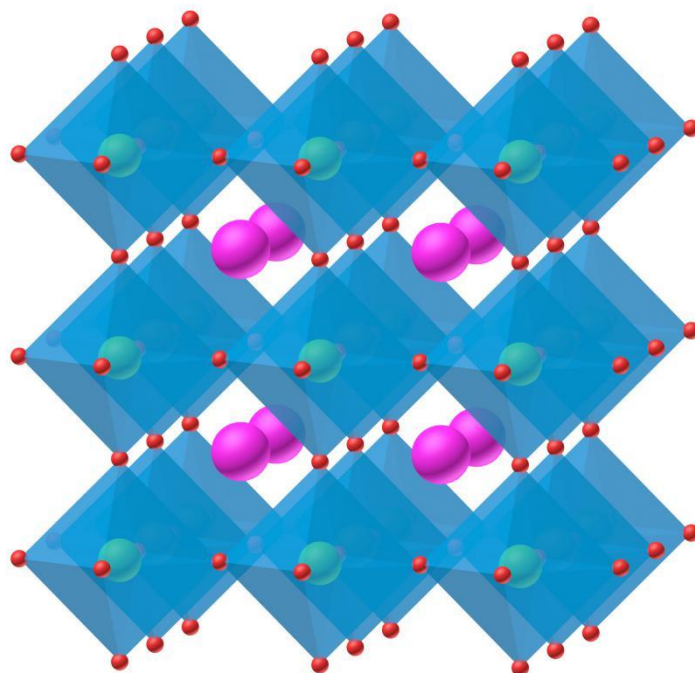


Figure 1.1 Perovskite structure, the big pink spheres represent A cations, the green spheres inside octahedra are B cations, small red spheres are X anions and the blue octahedra are $[BX_6]$.

them, perovskite with very a wide range of bandgap (from 1.24 eV to 3.10 eV, which is the light range from 400 nm to 1000 nm, in **Figure 1.2**) could be achieved.[38-48]

With given A and B cations, the bandgap decreases with the increasing of X anion radii, that is $E_g(\text{Cl}) > E_g(\text{Br}) > E_g(\text{I})$. By mixing different X anions, perovskite with different bandgaps could be obtained. For instance, the bandgap of MAPbBr_3 is about 2.3 eV, but introducing Cl and I in, the bandgap could vary from 1.57 eV to 3.17 eV, corresponding to $\text{MAPbBr}_a\text{I}_{3-a}$ and $\text{MAPbCl}_b\text{Br}_{3-b}$ (a and b ranging from 0 to 3).[49, 50] Owing to this excellent feature, perovskite could be fabricated with bandgaps varying in almost whole visible light spectrum. Besides, for MAPbI_3 perovskite, by

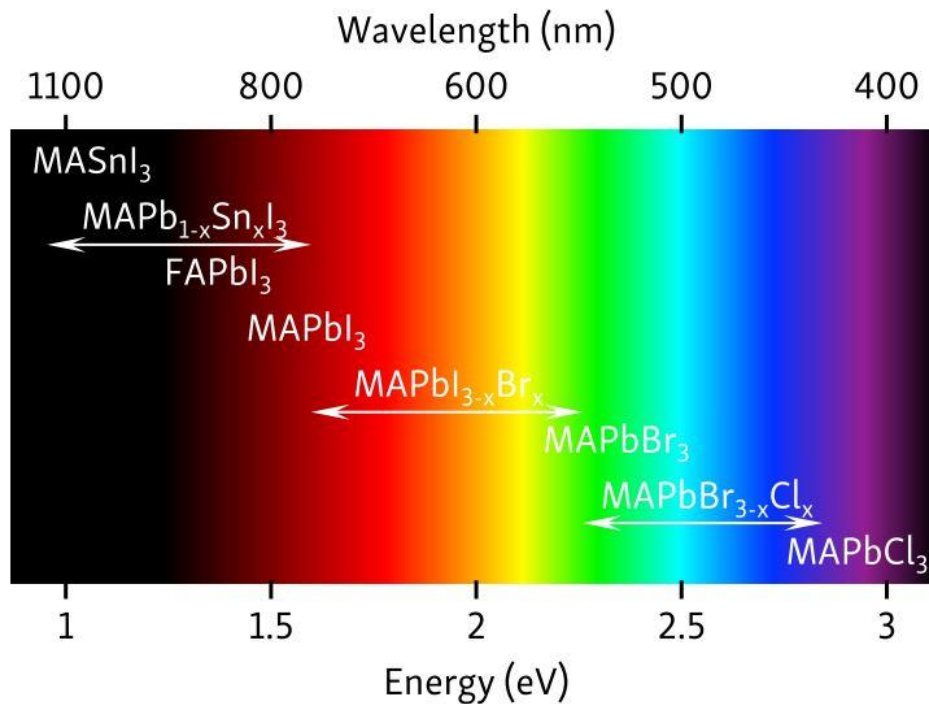


Figure 1.2 Bandgap region covered by different perovskite materials

changing MA cation, from Cs, MA, to FA, the radius increases, from 1.81, 2.70 to 2.79, the correlated bandgap decreases ($E_g(\text{Cs}) = 1.73$ eV, $E_g(\text{MA}) = 1.55$ eV, $E_g(\text{FA}) = 1.48$ eV).[51, 52] The last way to regulate the bandgap is substituting B, metal cation. Pb can be doped or replaced by Sr, Ca, Cd, Sn, Ge and so forth. Both calculation and experimental studies demonstrate the decrease of bandgap.[53-55]

1.3. High absorption coefficient

For the first and second generation solar cells, to collect most of the light from the sun, the light absorber layers should be around 300 μm and 2 μm respectively.[56, 57]

Figure 1.3 demonstrates the optical absorption mechanism of different solar cells. For Si, the first generation, although the absorption at band edge is from Si p orbitals to Si p and s orbitals, the indirect bandgap nature determines low absorption coefficient and very thick absorber layer to utilize majority of sunlight.

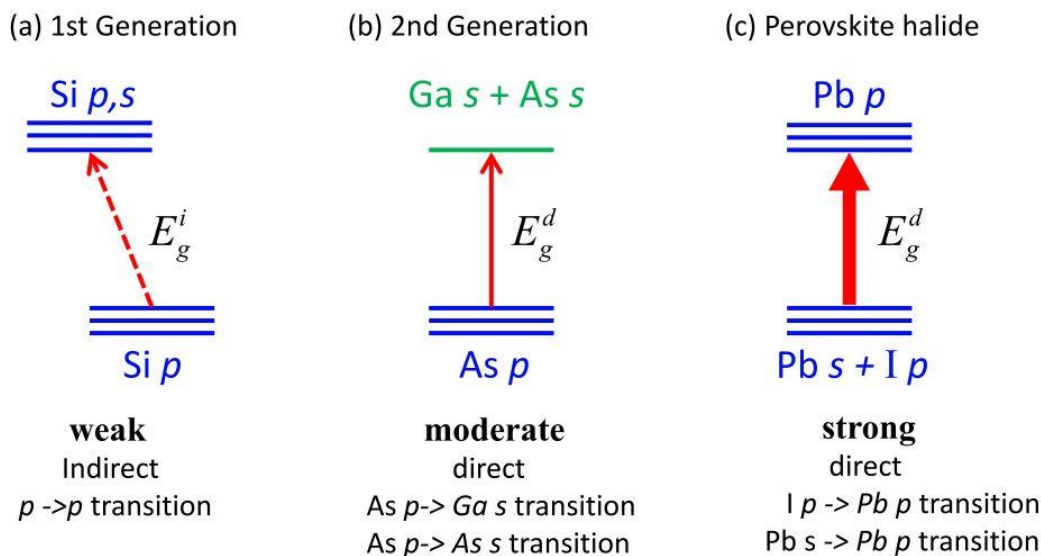


Figure 1.3 The schematic optical absorption of (a) first generation, (b) GaAs as prototypes for second generation, (c) perovskite solar cell absorber.[23]

GaAs, as one of the second generation, possesses direct bandgap, which is beneficial for light absorber. However, the conductive band minimum is composed by s orbitals of Ga and As, leading to lower electronic density of states. Thus, the optical absorption is still not so high.

Differently, perovskites have direct bandgap and the conductive band minimum is derived from Pb p orbitals. With higher density of states, the absorption coefficient is 2 to 4 times higher than GaAs at visible light range. MAPbI₃ has the absorption coefficient at order of $2 \times 10^5 \text{ cm}^{-1}$ at 500 nm, which means 300 to 500 nm thickness of MAPbI₃ could absorb the excitation light thoroughly. This thinner absorber layer also means less material cost for solar cells.[58]

1.4. Charge recombination

In metal halide perovskites, the initial decay at low excitation carrier density is approximately monoexponential corresponding to monomolecular decay.[59, 60] But

perovskite ^a	deposition method ^b	film architecture ^c	charge-carrier mobility ^d [cm ² (V s) ⁻¹]	recombination constants		
				k ₁ ^e [s ⁻¹]	k ₂ ^f [cm ³ s ⁻¹]	k ₃ ^g [cm ⁶ s ⁻¹]
MAPbI _{3-x} Cl _x	solution	meso Al ₂ O ₃	12	5 × 10 ⁶	0.9 × 10 ⁻¹⁰	1.0 × 10 ⁻²⁸
MAPbI _{3-x} Cl _x	2-source vapor	flat film	33	12 × 10 ⁶	1.1 × 10 ⁻¹⁰	0.2 × 10 ⁻²⁸
MAPbI ₃	solution	meso Al ₂ O ₃	8	14 × 10 ⁶	9.2 × 10 ⁻¹⁰	1.3 × 10 ⁻²⁸
MAPbI ₃	solution	flat film	35	15 × 10 ⁶	0.6 × 10 ⁻¹⁰	1.6 × 10 ⁻²⁸
FAPbI ₃	solution	flat film	27	7 × 10 ⁶	1.1 × 10 ⁻¹⁰	0.2 × 10 ⁻²⁸
FAPbBr ₃	solution	flat film	14	21 × 10 ⁶	11 × 10 ⁻¹⁰	1.5 × 10 ⁻²⁸
MASnI ₃	solution	meso TiO ₂	1.6	8 × 10 ⁹	14 × 10 ⁻¹⁰	

Table 1 ^aChemical formulae, where MA is CH₃NH₃ (methylammonium) and FA is HC(NH₂)₂ (formamidinium). ^bThrough a solution precursor or via dual-source vapor deposition under vacuum. ^cPerovskite flat films or infusions into a mesoporous metal oxide matrix. ^dCharge-carrier mobility at terahertz frequencies. ^eMonomolecular rate constant. ^fBimolecular rate constant. ^gAuger rate constant.

with the increasing of excitation carrier density, the initial decay time becomes shorter.[61] This dynamics can be depicted by the equation of time dependent carrier density n:

$$\frac{dn}{dt} = -k_1n - k_2n^2 - k_3n^3$$

where k_1n is monomolecular recombination with rate k_1 , k_2n^2 is bimolecular recombination with rate k_2 and k_3n^3 is Auger recombination with rate k_3 . **Table 1** summarizes the results of k_1 , k_2 and k_3 through global fitting of different materials.[62]

The monomolecular recombination is defined by a process generated by a single particle which can be an electron in CB, a hole in VB (trap-assisted recombination) or an exciton meaning bounded electron-hole pair (excitonic recombination). Bimolecular recombination, depending on both electrons and holes, can be viewed as intrinsic photon-radiative recombination correlated to the reverse process of light absorption. Auger recombination process involves three carriers, energy coming from the recombination of electron and hole is absorbed by third carrier, leading to the excitation of this carrier to higher energy level. Then the carrier relaxes to the bottom

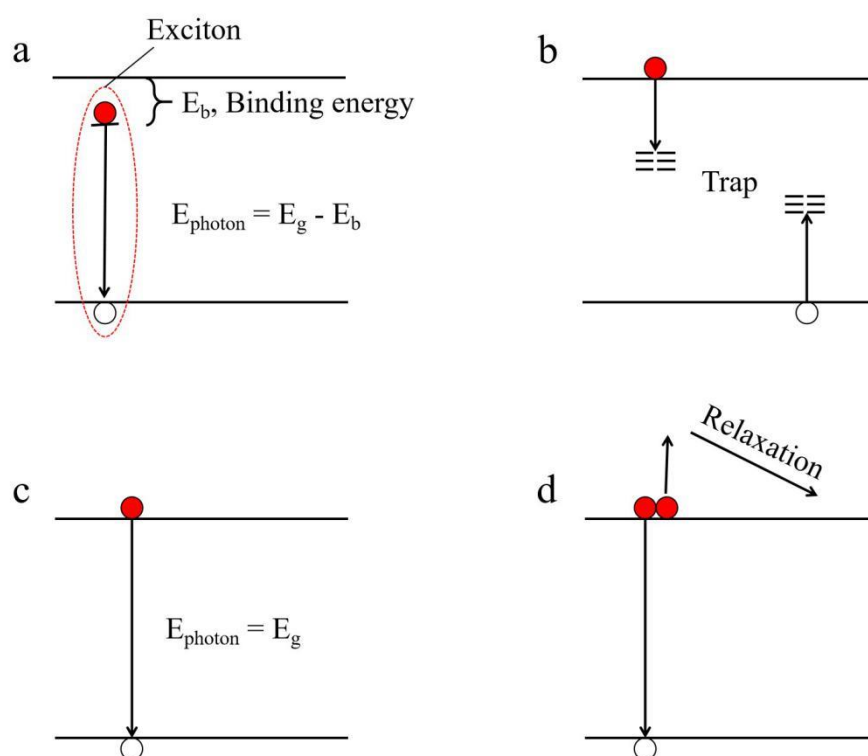


Figure 1.4 Recombination mechanisms, monomolecular recombination, including excitonic recombination (a) and trap-assisted recombination (b); bimolecular recombination (c); Auger recombination (d).

of conductive band with thermalization process. **Figure 1.4** depicts the scheme of the three different recombinations.

Generally, at very low carrier density, most of the perovskite materials make the monomolecular recombination the dominant process. However, with carrier density of 10^{17} - 10^{18} cm^{-3} , the recombination is mainly bimolecular recombination. Auger recombination can only be observed at very high carrier density $>10^{19}$ cm^{-3} . [63-67] It is noticeable that the photophysics of perovskite films is very different from of perovskite solar cell devices. Actually, the recombination lifetime of perovskite film can reach to several microseconds whereas the lifetime measured in perovskite device is sub-microsecond, even in optimized devices with PCE>20%. [68] This is mainly

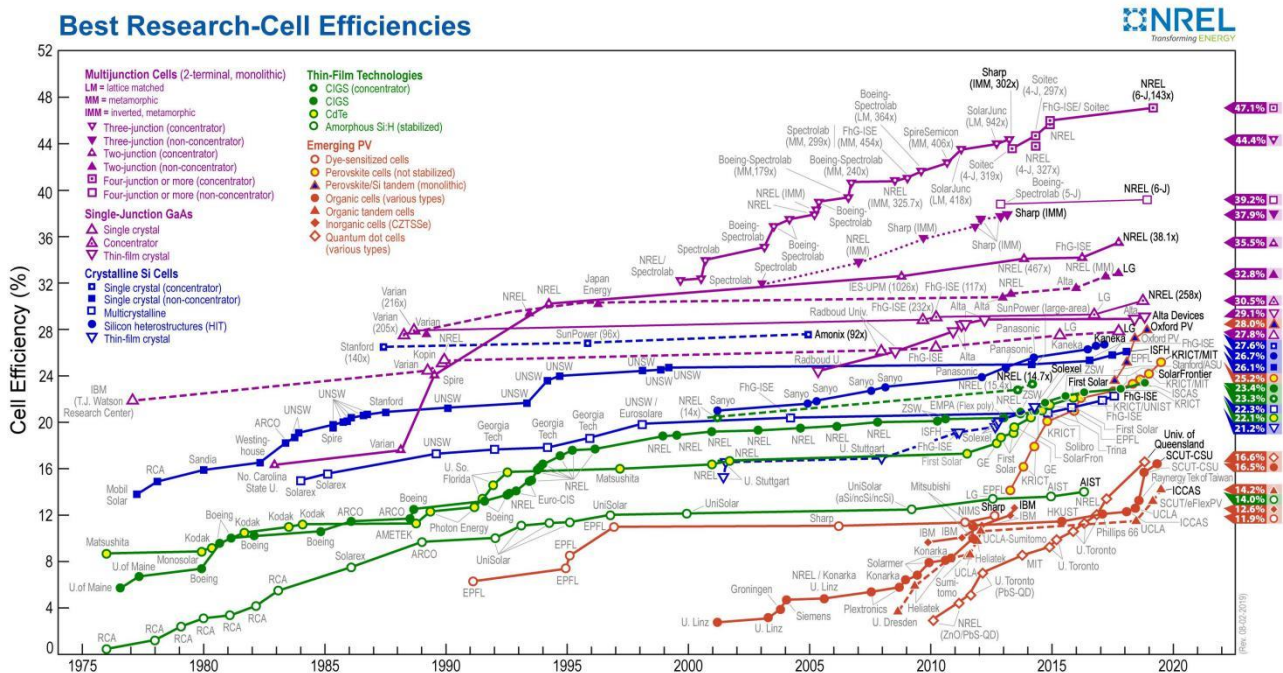


Figure 1.5 Highest confirmed power conversion efficiency of all different solar cells every year. The yellow circle with red outline represents perovskite solar cells (not stabilized). [3]

attributed to the separation of photo-generated electrons and holes caused by charge transport layers. As a result, the photoluminescence is really so weak that cannot be accurately measured by TRPL measurements. Considering the commonly observed correlation between the lifetime and device PCE, TRPL lifetime is still a reasonable parameter for defect density and suitability for solar cells. [69]

1.5. Metal halide perovskite solar cells

In 2009, Miyasaka and coworkers firstly applied MAPbBr_3 and MAPbI_3 as light absorbers in solar cells. Efficiency reached to 3.13% and 3.81% respectively.[5] Subsequently, Park and colleagues improved the PCE to 6.54% with MAPbI_3 quantum dots as light sensitizer in 2011. But the perovskite could dissolve into the redox electrolyte gradually, leading to about 80% degradation in 10 min.[70]

To improve the stability, liquid electrolytes must be substituted. In 2012, Park, Grätzel and coworkers introduced a solid state hole transport layer (HTL), spiro-OMeTAD, which increased PCE to 9.7% and significantly enhanced device stability.[71] Simultaneously, Snaith and colleagues found perovskite itself might transport electrons effectively, then they substituted TiO_2 electron transport layer (ETL) by insulating Al_2O_3 . The results exhibited an increased PCE of 10.7% and lower energy loss, 1.1V open circuit voltage with 1.55eV band gap. On this basis, they employed vapor deposition method to fabricate perovskite in a planar heterojunction device structure and achieved PCE of 15.4%.[72, 73]

After those pioneer works, more and more researches sprung up and the PCE of perovskite solar cells increased rapidly.[74-79] In 2014, Seok and coworkers boosted the PCE to 16.2% with no hysteresis by a solvent-engineering technology for depositing extremely uniform perovskite film.[80] Soon after, Yang and colleagues suppressed the carrier recombination in absorber by controlling formation of perovskite and careful choice of other charge transport layers. The PCE of their devices achieved to 19.3%.[81]

More recently, this year in 2019, You and coworkers added PEAI salt on FA-MA mixed perovskite films and found reduced defects and suppressed non-radiative recombination. The PCE of their devices reached to 23.32%.[82] Only several months later, from the newest NREL statistics, the record PCE has increased to 25.2%, accomplished by KRIST/MIT shown in **Figure 1.5**. All these breakthroughs are showing the bright prospects for the industrialization of perovskite photovoltaics.[83, 84]

However, despite the quickly increased PCE of devices, stability is a big issue that limits the industrialization.[85] As can be seen in **Figure 1.5**, only perovskite solar

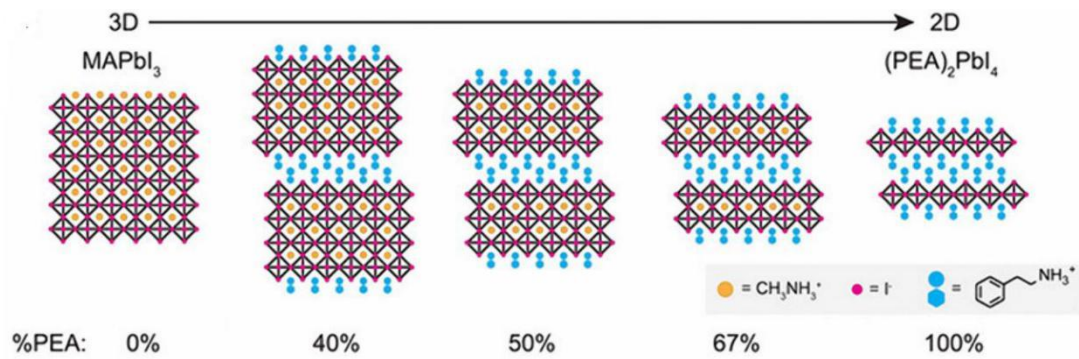
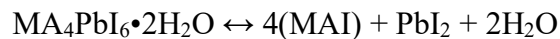
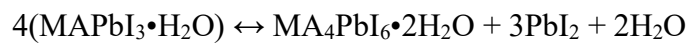


Figure 1.6 2D perovskite structures, from right to left are structures with n number 1, 2, 3, 4 which mean layers of $[\text{PbI}_6]^{4-}$ octahedra and infinite, that is 3D.[46]

cell is denoted as “not stabilized”. Moisture, either rain or water vapor can lead to the degradation, the mechanism can be described as below:[86]



Another factor is high temperature, some studies imply that at temperature higher than 100°, the surface of MAPbI₃ decomposes to PbI₂, CH₃I and NH₃. Finally, Pb²⁺ will be easily oxidized to Pb⁴⁺ when exposed to ambient condition.[87, 88]

Additionally, the toxicity level of Pb²⁺ is even higher than conventional Cd²⁺ in CdTe. Due to the stability in ecosystem, once the lead and its compounds are releasing into the environment, the harm will be almost eternal.[54, 89] To protect environment and implement sustainable development, it is necessary to replace lead by other non-toxic, environment friendly metal element.

1.6. Two dimensional hybrid perovskite

Since the instability is an inevitable constraint for perovskite solar cells, developing stable perovskite attracts more and more attention.[90-93] One of the methods is to reduce the dimension of perovskites. For MAPbI₃ perovskite, $[\text{PbI}_6]^{4-}$ octahedra are

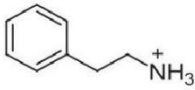

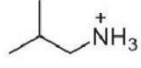
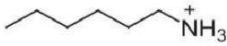
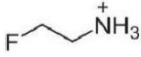

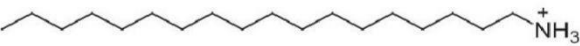
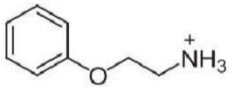
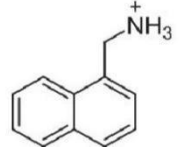
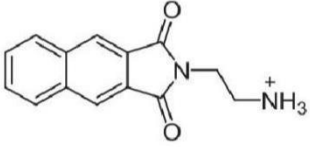
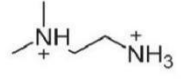
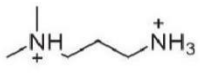
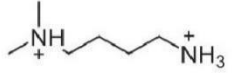
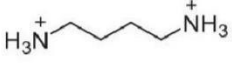

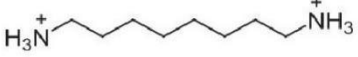
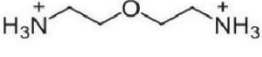
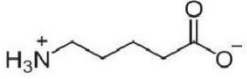
Organic spacer cation	Molecular structure
PEA	
n-BA	
iso-BA	
n-C ₆ H ₁₃ NH ₃	
(FC ₂ H ₄ NH ₃)	
n-C ₈ H ₁₇ NH ₃	
OA	
POEA	
NMA	
NAAB	
DMEN	
DMAPA	
DMABA	
Bd	
Hd	
Od	
EDBE	
Ava	

Table 2 Reported different large organic cations for 2D perovskite structure.[50]

connected to each other in all the three dimensions thus it is called 3D perovskite.

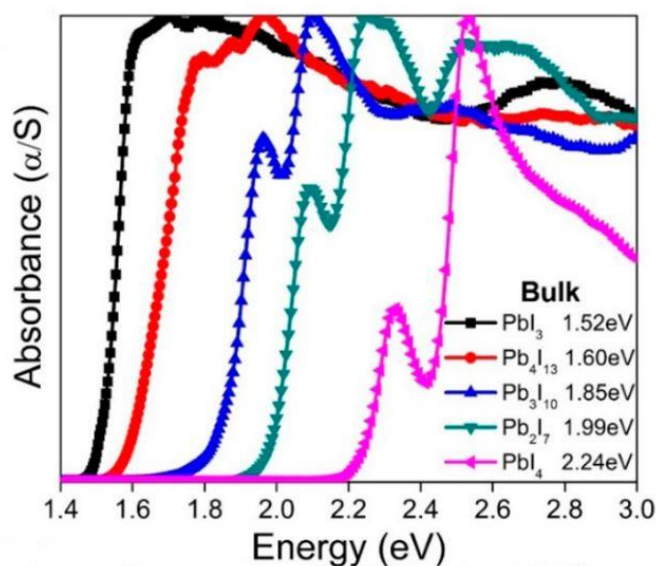


Figure 1.7 Absorbance of different 2D perovskite ($BA_2MA_{n-1}Pb_nI_{3n+1}$) and 3D perovskite ($MAPbI_3$), the bandgap decreases with the increase of n number.[51]

When some of the MA are exchanged by much larger organic cations, then the octahedra will separate, leading to a lower-dimensional structure, including 2D, 1D and even 0D.[94, 95]

Among the different structures, 2D perovskites are very good candidates for solar cells. The formula of those kind of 2D perovskites is $A'_2A_{n-1}B_nX_{3n+1}$, where A, B and X are the same with their 3D counterparts, while A' is an organic cation much larger than A, such as phenethylammonium (PEA, $C_6H_5CH_2CH_2NH_3^+$) and butylammonium (BA, $CH_3CH_2CH_2CH_2NH_3^+$).[96, 97] Different kinds of A' are summarized in **Table 2**. [98] Thus, by regulating the molar ratio of the precursors, different 2D perovskites with n layers $[BX_6]^4-$ octahedra separated by 2 layers A' cations could be obtained, from pure 2D ($n = 1$) to 3D ($n = \text{infinity}$), depicted in **Figure 1.6**. [99]

The large organic cation layers confine the charge transport between different octahedral $[BX_6]^4-$ layers, acting as natural insulating “barriers” and the octahedra

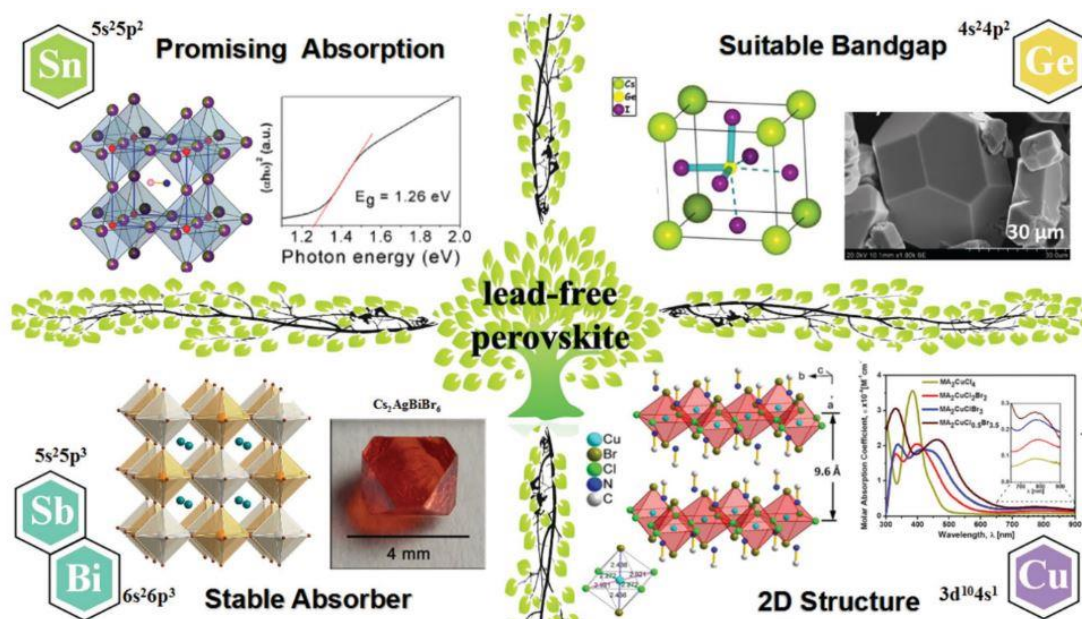


Figure 1.8 Promising metal substitutions for lead free organic inorganic hybrid perovskites.[57]

layers as conductive “wells”. This special structure leads to much broader band gap ~ 2.6 eV than 3D one 1.5 eV for low n , which is not a suitable band gap for solar cells. Differently, from $n = 4$, high n members possess narrower band gap ~ 1.7 eV (**Figure 1.7**) and better stability in the air environment. [97, 100]

Those quasi-2D perovskites are investigated extensively for light absorption materials in solar cell applications in recent years.[101] In 2014, Smith et al firstly employed a 3-layer $\text{PEA}_2\text{MA}_2\text{Pb}_3\text{I}_{10}$ perovskite as light absorber in solar cells, in a n-i-p device structure, with TiO_2 as electron transport layer (ETL) and Spiro-OMeTAD as hole transport layer (HTL).[102] Enhanced stability resulted, but only 4.73% of PCE. Soon after, Cao et al used BA as large organic cation using the same device structure and made $n=1$ to 4 perovskite solar cells with the highest PCE at 4.02%.[100] Those pioneering attempts show the critical issue that is the multiple-quantum-well structure is a great obstacle for out-of-plane charge transport. Thus, to control the growth orientation of “wells”, to make them perpendicular to ETL and HTL is highly

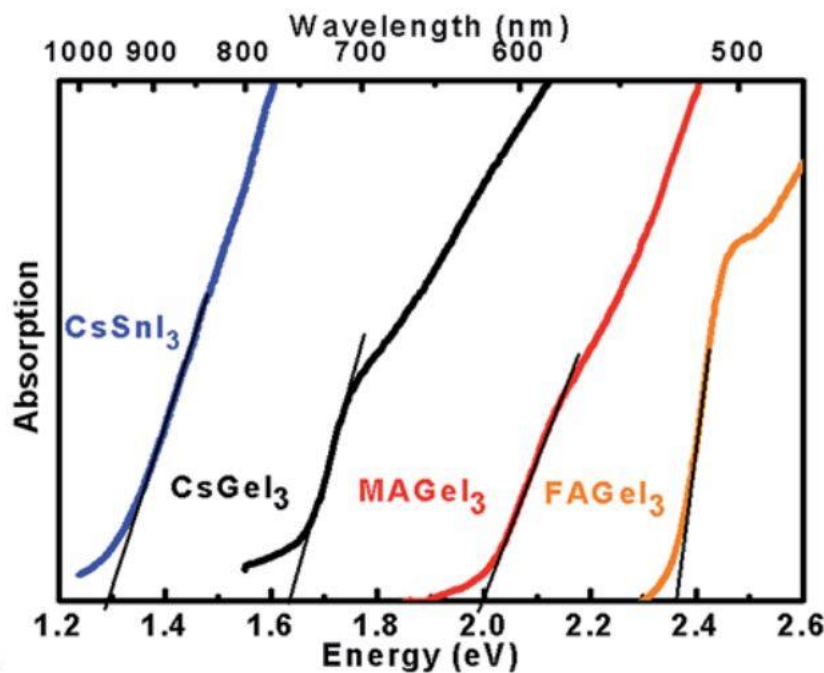


Figure 1.9 Absorption spectra of CsGeI_3 , MAGeI_3 and FAGeI_3 hybrid perovskites, with CsSnI_3 as comparison.[61]

advantageous for charge transport and electron-hole separation. To achieve this goal, several methods have been developed. Tsai et al applied hot-casting method when depositing $\text{BA}_2\text{MA}_3\text{Pb}_4\text{I}_{13}$ ($n=4$) thin films on substrates, before deposition of perovskite thin films, the substrates are preheated to a temperature of $\sim 150^\circ\text{C}$. They successfully fabricated oriented 2D thin films and increased the PCE to 12.52%.[103] Other efforts, such as Cesium doping, adding additive in perovskite precursor solution and so forth, also achieved some excellent results.[104-107] All these achievements imply that 2D perovskites are promising substitutions for solar cells.[108, 109]

1.7. Lead free hybrid perovskite

Not many choices can be select to replace Pb in perovskites, not only because the tolerance factor constraint, but also the electronic structure of Pb. Pb is rather important to stabilize the structure according to theoretical calculation studies. To date,

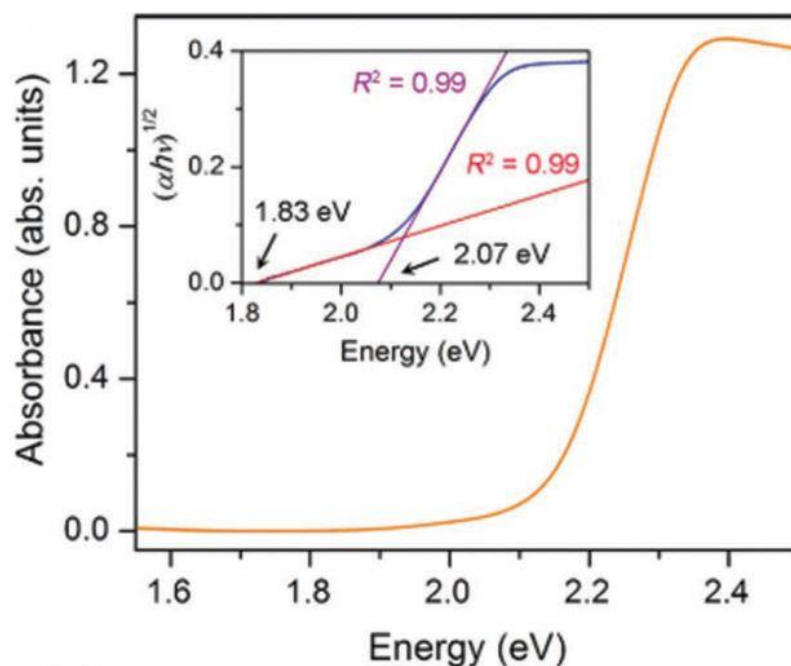


Figure 1.10 Optical absorption of $\text{Cs}_2\text{AgBiBr}_6$. Inset: Tauc plot showing optical bandgap of 1.95 eV with phonon of 0.12 eV.[65]

only Sn, Ge, Cu and some double perovskites are proved that can be potential candidates (**Figure 1.8**).[110]

As in the same main group, Sn is similar to Pb. The radii of Sn and Pb are 1.35 Å and 1.49 Å respectively, which encourages to be a substitution. [111-113] Snaith et al firstly reported MASnI_3 solar cells in 2014.[114] Studies exhibit that MASnI_3 possess highly symmetrical α -phase of $P4mm$ group even at room temperature. The absorption edge is much broader than MAPbI_3 , approximate to 1000 nm with bandgap estimated at 1.23 eV. But the PCE is much lower compared to Pb counterpart, only 6.4%. Almost the same time, Kanatzidis et al developed mixed $\text{MASnI}_{3-x}\text{Br}_x$ as light absorber material.[115] With the increasing of x, the absorption blue shift from 950nm (MASnI_3) to 577nm (MASnBr_3), leading to the film color changing form dark brown to bright yellow. The best PCE is achieved by MASnIBr_2 solar cells, which is 5.73%. Since the low PCE of pure tin perovskite, lots of people start to research on Sn-Pb mixed perovskites. However, more recently, Loi et al applied FASnI_3 as active

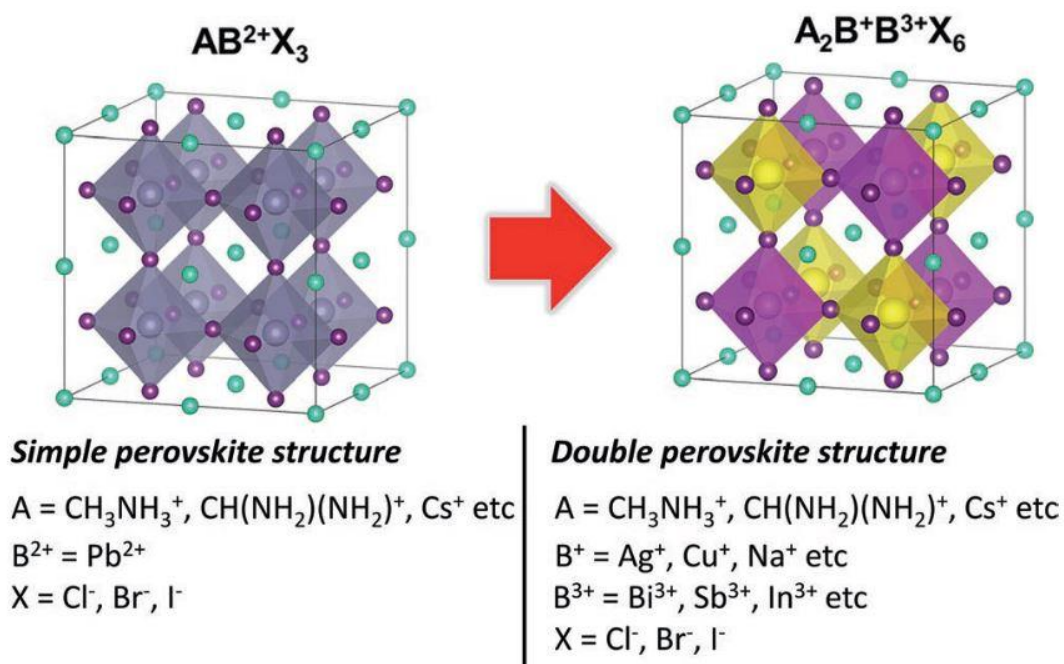


Figure 1.11 Schematic representation of double perovskite structure and the variety of different metal elements, normal 3D perovskite as comparison.

layer for solar cells. By inducing a small amount of 2D tin perovskite, the perovskite thin film showed high crystallinity and preferable orientation. Compare to the pristine 3D thin film, this 2D/3D thin films got reduced number of grain boundaries, suppressed tin vacancies and longer carrier lifetimes. As a result, device with PCE of 9.0% was achieved, which is the highest PCE of tin perovskite solar cells so far.[116]

Ge (germanium), is another similar element that may replace Pb for perovskites. The radius of Ge^{2+} is 0.73 Å, and the tolerance factor of $MAGeCl_3$, $MAGeBr_3$ and $MAGeI_3$ are 1.005, 0.988, and 0.965 respectively, which are all in ideal range for perovskite structure.[117, 118] Stoumpos et al reported a series of Ge perovskite, $CsGeI_3$, $MAGeI_3$, $FAGeI_3$ etc in 2015.[117] Studies exhibited that the bandgap is strongly affected by the A cations, ranging from 1.63 to 2.8 eV. Bandgaps of $CsGeI_3$, $MAGeI_3$, $FAGeI_3$ are 1.63, 2.0 and 2.35 eV, as shown in **Figure 1.9**.[119] Although Ge is suitable for ideal tolerance factor, but it is so small that cannot fit the $[GeI_6]^{4-}$

octahedron well, leading to structural distortions. So far, very few studies have been reported because of the instability of Ge^{2+} , even worse than Sn^{2+} . The PCE of works done by Krishnamoorthy et al and Kopacic et al are all less than 1%. [119, 120] Further researches still need to be carried on for revealing material properties and improving solar cell PCE of Ge perovskites.

Recently, Karunadasa et al reported a double perovskite, $\text{Cs}_2\text{AgBiBr}_6$, incorporating Bi^{3+} in a 3D perovskite framework for the first time in 2016. [121] This is a new line of thoughts to solve the issues of mostly studied Pb perovskites. The absorption region of $\text{Cs}_2\text{AgBiBr}_6$ starts from 1.8 eV and at 2.1 eV there is a sharp increase. The Tauc plot exhibits that it possess an indirect bandgap of 1.95 eV with phonon energy 0.12 eV, which may be useful for tandem solar cells (**Figure 1.10**). With different permutation and combination of B^{I} and B^{III} elements, different double perovskite can be obtained (**Figure 1.11**). [122, 123] The biggest advantage is this kind of perovskite is rather stable. Woodward et al synthesized $\text{Cs}_2\text{AgBiBr}_6$ and $\text{Cs}_2\text{AgBiCl}_6$ perovskite and found that they were rather stable to light irradiation or moisture. [124] However, the indirect bandgap nature again implied future use for tandem solar cells. Giustino et al reported direct bandgap double perovskite, $\text{Cs}_2\text{AgInCl}_6$. [125] The measured optical bandgap is 3.3 eV with a very weak absorption at 2.1 eV. And it is very interesting that there is a reversible color changing from white to orange under UV light irradiation. After these pioneer researches on double perovskite material properties, some solar cell devices were fabricated. However, same as Ge perovskite solar cells, the PCE is very low, which is not higher than 3%, not the stability, the main constraint is the not suitable bandgap. Future works should be focused on this issue.

1.8. Scope of this thesis

In this thesis, considering the two disadvantages of perovskite, efforts were made on

stability and non-toxicity.

First of all, quasi-2D lead perovskite ($n=5$, $\text{PEA}_2\text{MA}_4\text{Pb}_5\text{I}_{16}$) solar cells were fabricated. Vacuum assisted method was employed to deposit the perovskite thin films. Since it is not easy to obtain pure $n=5$ perovskite, XRD (X-ray diffraction) and GIWAXS (grazing incident wide angle X-ray scattering) measurements were performed to confirm the phases of the perovskite thin film and the crystal growth orientation. Results show that films deposited by conventional method show much $n=2$ phase at the bottom side which is not beneficial to charge transport, whereas films deposited by vacuum method show mainly $n=5$ phase with little $n=2$ phase. The vacuum-films also exhibit more compact morphology with less grain boundaries and cracks. Then, by introducing a novel, pH neutral hole transport layer into the devices, PCE increases to above 14%.

Secondly, 2D tin perovskite thin films were fabricated ($n = 1, 2, 3$, $\text{BA}_2\text{MA}_{n-1}\text{Sn}_n\text{I}_{3n+1}$). With conventional method for film deposition, it is fine to get rather pure $n=1$ and $n=2$ samples, but not for $n=3$. Still by using vacuum assisted method single phase of $n=3$ can be achieved. Then TRPL (time-resolved photoluminescence) and pump-probe spectroscopy measurements were carried on to detect the behavior of photo generated carriers in the samples. The results of TRPL exhibit in $n=1$ sample, the photo generated carriers are mainly excitons while in $n=2$ sample, the carriers are free carriers. The $n=3$ sample is not really clear because of the low reproducibility which made the results unreliable. In addition, pump-probe results furtherly confirmed the results of TRPL measurements. Besides the fast degradation of the samples in the air may also be one of the reasons for uncertainty for $n=3$ sample, all the samples degraded more than 50% within 30 min.

2. Synthesis and characterization

2.1. Perovskite thin film deposition

Perovskite thin film deposition is very important in making solar cell devices.[126, 127] The quality of film directly determines the PCE of the devices.[128] A smooth, compact with less grain boundaries thin film is beneficial to solar cell devices. Various methods have been developed to achieve this goal.

2.1.1. Spin-coating method

Spin-coating may be the most widely used method to deposit perovskite thin films.[129-133] This technique includes one-step, two-steps and anti-solvent method, scheme depicted in **Figure 2.1**.

One-step spin-coating. This should be the easiest for operation. For instance, to deposit MAPbI₃ film, first of all, precursor chemical MAI and PbI₂ are dissolved in DMF (Dimethylformamide), DMSO (Dimethyl sulfoxide) or GBL (γ -Butyrolactone) solvent. After the precursors dissolve in the solvent homogeneously, for a 3×3 cm substrate, 2 or 3 drops (80-120 μ L) will be enough for spin-coating. Then by regulating the spin speed, film with different thickness will be fabricated. Besides, the concentration and solvent type will also affect the thickness. After the deposition, the as prepared film should be heated to $\sim 100^\circ$ for further crystallization. Films fabricated in this way usually has an issue of coverage, besides the film morphology is also not with high quality.

Two-steps spin-coating. This method is separated in two steps. First, PbI₂ in DMF is deposited on the substrate at specified temperature, after cooling down, the substrate with PbI₂ thin film is soaked in MAI/IPA solution to react to MAPbI₃ thin film.

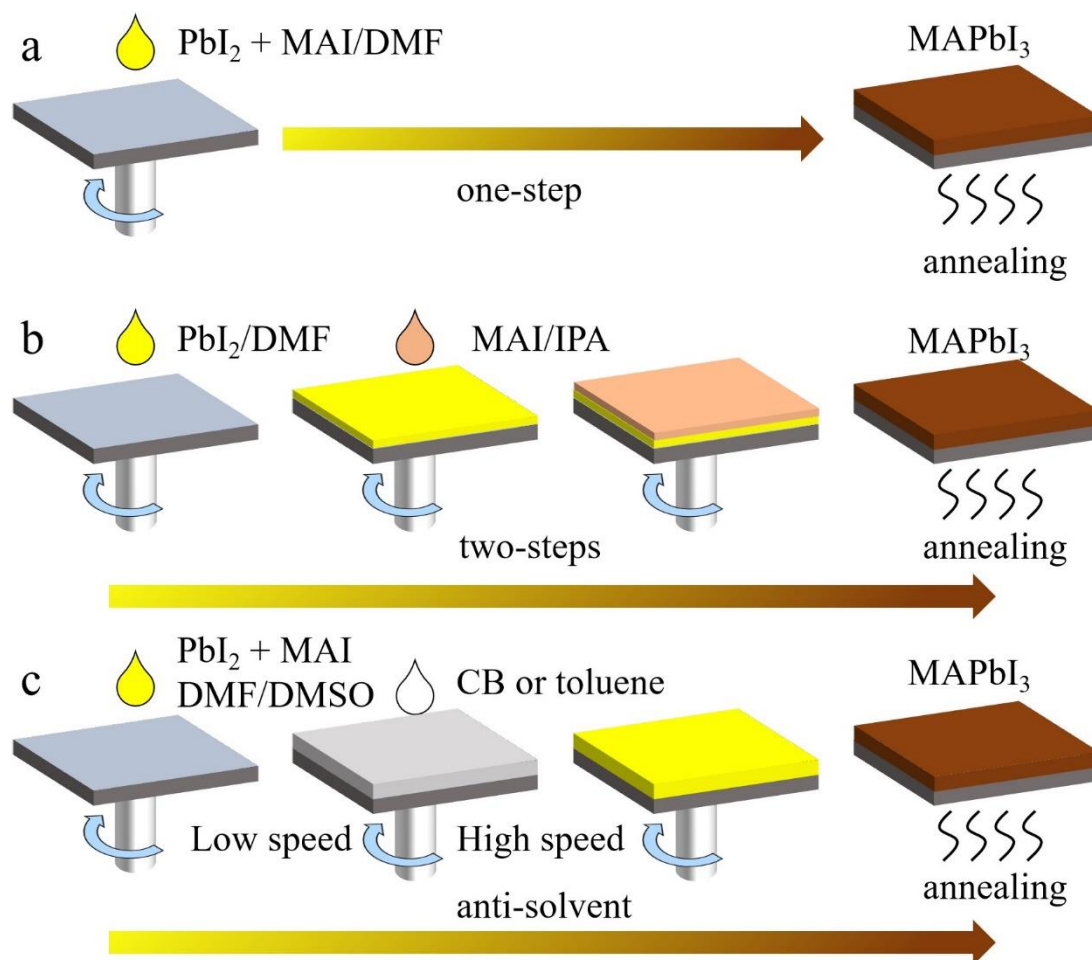


Figure 2.1 Scheme for different spin-coating method to deposit MAPbI₃ thin films, (a) is one-step, (b) is two-steps, IPA represents iso-propanol alcohol and (c) is anti-solvent technique, anti-solvent can be CB (chlorobenzene), toluene, diethyl ether etc.

Another way is still spin-coating MAI on the substrates following the PbI₂ deposition step. Finally, same as one-step, the film is annealed at ~100°.

Anti-solvent method. Anti-solvents can change the supersaturation, the nucleation and also the crystal growth rates, thereby they will strongly affect the crystallization kinetics and final morphology. Generally, this method is processed in two spin-coating speed, a very short time for low speed (within 2 s) and a long time for high speed (up to 60 s). Anti-solvent is added at high speed. Proficiency of adding anti-solvents is important in this process, because too fast leading to washed away of perovskite in the center of the thin films while too slow leading to very large cracks of the final thin film that can be seen by eyes.[134] Crystallization starts when

anti-solvent is added, by annealing is still necessary for totally crystallization.

Comparing the three solution-process methods, one-step is the easiest one for operation, but thin films fabricated in this way are difficult to form uniform morphology and high coverage. In contrast, two-steps and anti-solvent method are preferable to get smooth, compact films, but they need higher proficiency level for operation, especially the anti-solvent method.[135-137]

2.1.2. Vapor deposition

Scalable and highly reproducible fabrication is indispensable for industrialization, comparing to the uncertainty with solution processing methods, vapor deposition can completely satisfy those requests. In double sources vapor deposition, MAI and PbI₂ are evaporated to compacted TiO₂ at 120° and 325° in high vacuum degree (~10⁻⁷ mbar) chamber simultaneously. Different from solution processing, the homogeneity of the final films is remarkably improved.[73] Yang et al modified the procedure and avoid high temperature and high vacuum. They spin-coated PbI₂ on compacted TiO₂, followed by heating the substrate inside MAI vapor with nitrogen. By this way, they achieved good morphology for films and 12.1% PCE for solar cells.[138]

2.2. X-ray diffraction (XRD)

In 1912, on the basis of theoretical prediction, Laue confirmed that the atoms at a distance from tens to hundreds picometers to each other in crystal materials are periodically arranged. This periodically arranged structure can become diffraction gratings for X-ray and the experiment becomes the first milestone of X-ray diffraction. When a beam of monochromatic X-rays is incident on the crystal, since the crystals are composed of unit cells which are regularly arranged by atoms, the distance between these regularly arranged atoms is the same order of magnitude as the X-ray diffraction analysis of the incident X-ray wavelength, so it is scattered by different atoms. The X-rays interfere with each other and produce strong X-ray diffraction in

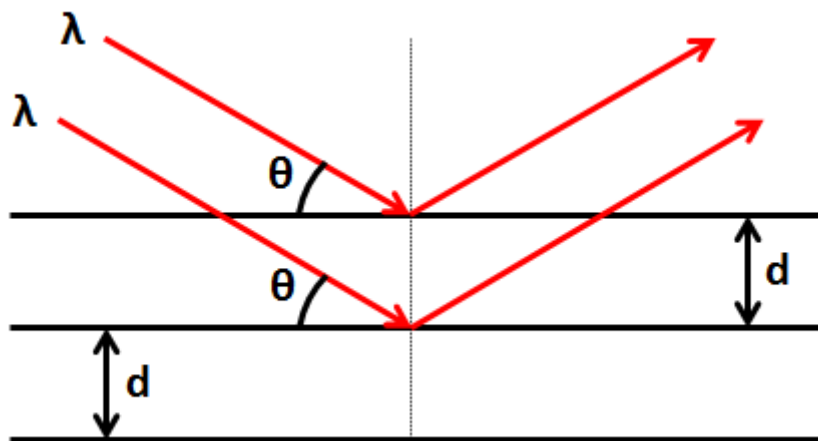


Figure 2.2 Scheme for X-ray diffraction

some special directions. The orientation and intensity of the diffraction lines in the spatial distribution are closely related to the crystal structure. The diffraction patterns produced by each crystal reflect the atoms arrangement rules inside the crystal. This is the basic principle of X-ray diffraction, scheme in **Figure 2.2**. [139]

The diffraction can be described by Bragg's Law, $2d \sin\theta = n\lambda$, where d is the distance of diffraction planes, θ is the angle of incident X-ray and diffraction planes, n is any integer, and λ is the wavelength of the X-ray. The angle of incidence of X-ray and transmission is 2θ . Different diffraction planes can be denoted by d_{hkl} , where hkl are called Miller Indices. With different θ , X-ray can be diffracted by all the planes (if there is the plane growing in the crystal). Then, after comparing the hkl from experiments with standard reference patterns, we can determine the phase of the samples.

2.3. Optical absorption

Absorption spectrum is commonly used for bandgap determination of semiconductor materials. When the incident light photon energy is larger than the bandgap of the semiconductor, the light will be absorbed by the semiconductor, leading to the

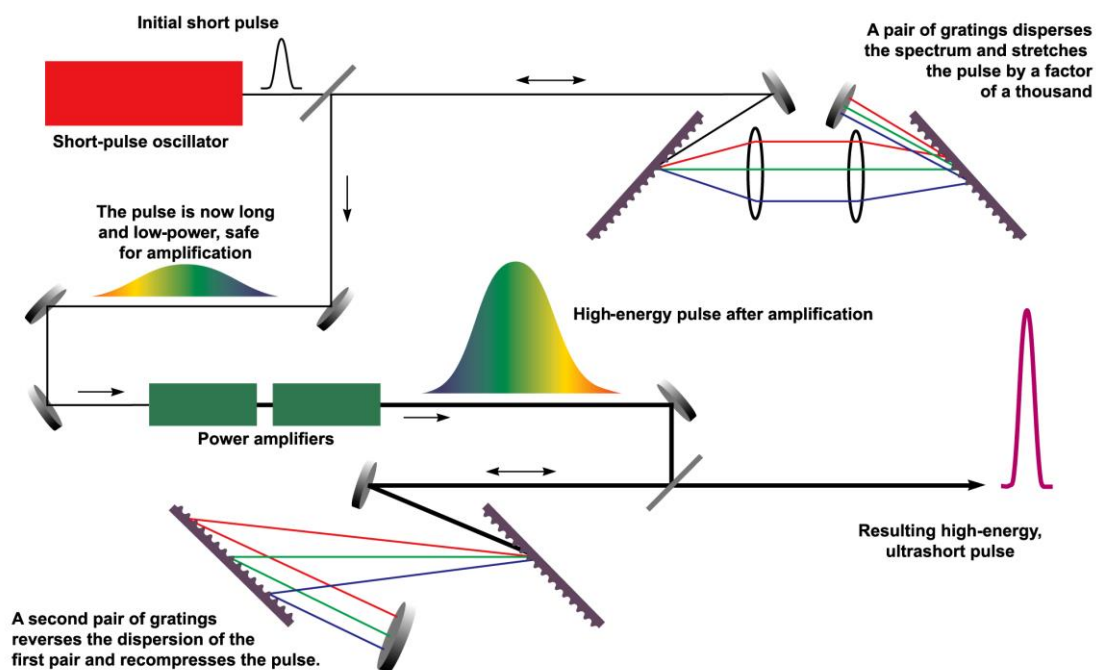


Figure 2.3 Scheme of chirped pulse amplifier.

electron transition from the valence band to conduction band. The basic principle is given by Beer-Lambert law, $A = \epsilon lc$, where A is the absorbance, ϵ is the molar attenuation coefficient, l is the optical path length, that is how long does the light pass in the sample, and c is concentration of the attenuating species.[140]

Absorption spectra of 2D tin perovskite films are measured with a UV/Visible Perkin Elmer Lambda 950 spectrometer. Using this spectrometer, absorbance data can be measured directly, and then after the film thickness is measured, we can get the Tauc plot.

2.4. Time-resolved photoluminescence (TRPL)

TRPL is one of the measurements of ultrafast spectroscopy and the core of the measurement is the laser.[141, 142] The first question is how to change continuous wave laser to ultra short laser pulse. Depending on the duration and energy of the pulses we want to produce, two engineering solutions are available: Q-switch or a

variable attenuator inside the laser cavity (usually resulting in high energy pulses with the duration of several nanoseconds); mode-locking of the light modes inside the laser cavity (for obtaining pico- and femtosecond pulses). In the case of this thesis, mode-locking is applied to generate laser pulse and the laser is from Ti:Sapphire oscillator.

After generated laser pulse, we need to amplify the laser pulse since the laser come from the oscillator has very high repetition and narrow tuning range. To obtain higher pulse energies, a technique called chirped pulse amplification is employed (**Figure 2.3**). In this technique, the initial short laser pulse is stretched in time by a factor of a thousand through a pair of gratings. Then the power of the pulse is amplified. Finally, a second pair of gratings reverses the stretching process and compresses the pulse.

Now we have the last question, the tuning range is only from 700-1000 nm. The next is to amplify the energy range. Optical parametric amplification is used for this process.

First of all, the laser beam (denoted as pump) with frequency ω_p is split into two beams with frequency ω_s and ω_i which are signal and idler. The relation is given by equation $\omega_p = \omega_i + \omega_s$. This effect is achieved using a non-linear crystal. The wavelengths of the signal and idler are determined by the phase matching condition, which can be modified by changing the angle between the incident pump laser and the optical axes of the crystal. This means that signal's wavelength can be tuned just turning the crystal using a stepper motor. In the special case of $\omega_s = \omega_i$, we have the exact reverse of the second-harmonic generation, which is called degenerate parametric amplification.

After the signal has been produced, the OPA will amplify it, using again nonlinear processes in crystals. A pump photon excites the system to a virtual energy level, whose decay is stimulated by a signal photon. Therefore, another photon is emitted

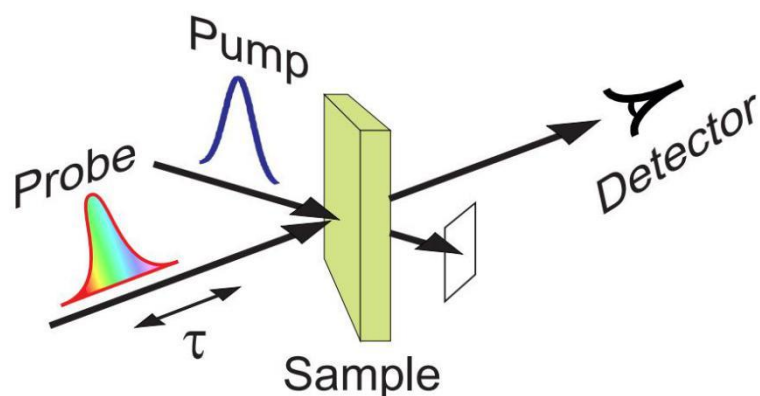


Figure 2.4 *Diagram of pump-probe measurement.*

with the same direction, energy and phase of the signal one. Since we are interested in a monochromatic beam, the idler is filtered and only the signal can escape the OPA. Due to the conservation of energy, it follows that it is impossible to obtain a signal with a wavelength lower than the pump. This can be obtained doubling the signal using second-harmonic generation. Now we have the laser that can perform TRPL measurements.

2.5. Pump-probe spectroscopy

The diagram of a general pump-probe measurement is shown in **Figure 2.4**.^[143] In pump-probe system, the laser pulse is split to two pulse by a beam splitter. The two split beams are called pump pulse and probe pulse, generally the pump pulse is much more powerful than the probe pulse and also has a larger size of beam spot that can totally cover probe beam spot. There is a time delay system to regulate the time delay between pump and probe and the two laser beams must be temporally coincident on the sample. The strong pump excites the sample and changes the state of the sample, then the weak probe detects the perturbation changes.^[142, 144] By measuring the differential transmission with different delay time, we can know the dynamic process of the material. In this experiment, the $\Delta T/T$ is measured. The experiment set up is shown in **Figure 2.5**.



Figure 2.5 Pump-probe spectroscopy set up for the experiments.

There are three phenomenon can be observed in this measurement. First one is named ground state photobleaching, with the spectral shape of ground state absorption after thermalization. In this case, the pump pulse reduces the number of absorbing molecules in the ground state inducing an absorption decrease at probe frequencies equal or higher than the ground state absorption. The result is the increasing of $\Delta T/T$. The second one is stimulated emission, which leads to an increasing of photons with the same direction, wavelength and phases. The pump pulse populates the excited state, the probe photon can stimulate it to emit back to the ground state. In this case the $\Delta T/T$ is still increased. The third one is called photoinduced absorption, that is in this case, the probe excited electron from excited state to higher excited level. Thus, the transmission is decreased and $\Delta T/T$ shows a negative value.

3. Quasi-2D lead perovskite solar cells

2D perovskites are being studied by more and more researches since their stability. Various film processing methods were developed to improve the device PCE. But the device structure has not been optimized so much, especially for the hole transport layer. Generally, solar cells are employing spiro-OMeTAD or PEDOT: PSS as hole transport layer (HTL) in solar cells and they are also the most commonly used in 2D perovskite solar cells. But the drawbacks are apparent, the conductivity of spiro-OMeTAD is really low ($\sim 10^{-5}$ S cm⁻¹), and in this kind of structure TiO₂ or other metal oxides will be used as electron transport layer (ETL) which need very high temperature ($\sim 300^\circ\text{C}$) for deposition. PEDOT: PSS is widely used in p-i-n structure which has easy device fabrication process and possess higher conductivity ($\sim 1.35 \times 10^{-3}$ S cm⁻¹). [84, 88, 102, 145] But it's not a pH neutral material, the acidity is corrosive to the anode which may cause device defect, decreasing the device performance. [146] Thus, a suitable HTL with pH neutral, high conductivity and matched work function is needed for improving the solar cell performance. [147, 148] Herein, we report on how the different HTL affect the device of p-i-n 2d perovskite (PEA₂MA₄Pb₅I₁₆) solar cells.

In this part, we prepared quasi-2D lead perovskite and by XRD, absorption spectroscopy and GIWAXS measurements confirmed the composition phases of the film. By a different processing method, the orientation of film growth was controlled to charge transport preferable direction. PCP-Na [149] (structure in **Figure A7**) was employed as the HTL for solar cells and PEDOT: PSS was chosen as the control experiment. PCP-Na possesses an electrical conductivity (1.66×10^{-3} S cm⁻¹) a little bit higher than PEDOT: PSS. The HOMO level of PCP-Na (-5.22 eV) is closer to the valence band of PEA₂MA₄Pb₅I₁₆ perovskite (-5.3 eV) comparing to PEDOT: PSS (-5.11 eV) which results in the enhancement of open circuit voltage of solar

cells.[150]

3.1. Experimental section

3.1.1. Film deposition and device fabrication

Materials. PEDOT: PSS water dispersion (Clevios VP AI 4083) was acquired from Heraeus. PEAI, MAI (>98%) and PbI_2 (>99.99%) were purchased from TCI EUROPE N.V. PCBM was purchased from Solenne BV. C_{60} (>99.9%), BCP (99.99%), DMF (99.8%), and DMSO (99.8%) were purchased from Sigma Aldrich. All the materials were used as received without further purification. PCP-Na was synthesized following a previously reported method.[149]

Perovskite film deposition. The precursor solution was mixed by 0.4 mmol PEAI, 0.8 mmol MAI, 1 mmol PbI_2 and 0.4 mmol ammonium thiocyanate (NH_4SCN) in 1 mL DMF solvent or DMF/DMSO mixed solvent with ration of 1:2. The 2D perovskite precursor solution in pure DMF was deposited at a speed of 5000 rpm for 45 s followed by 100 °C annealing for 10 min on the hotplate. The solution with mixed solvent was deposited at a speed of 5000 rpm for 20 s, The above films were immediately annealed at 100 °C for 10 min (conventional method) or put in vacuum for 5 min and then annealed at 100 °C for 10 min (vacuum assisted method). The as-prepared films on glass were for further characterizations.

Device fabrication and Characterizations. ITO glasses were cleaned in soap water ultrasonication, followed by washing with water, acetone, isopropyl alcohol in sequence. Then the substrates were treated by UV-ozone for 10 min to remove organic residues which may affect the deposition of hole transport layers. PEDOT: PSS was spin-coated on the cleaned ITO substrates at a speed of 3000 rpm for 60 s. PCP-Na was dissolved in solvent mixture of water and methanol with the volume ratio of 3:7 and was spin-coated on the substrates at a speed of 3000 rpm for 30 s. The

HTL coated substrates were dried at 140 °C for 15 min. Then the substrates were transferred to a glove box filled with nitrogen. On those substrates, $\text{PEA}_2\text{MA}_4\text{Pb}_5\text{I}_{16}$ films were deposited in the same way above. Then PCBM solution in chlorobenzene of 20 mg mL⁻¹ was deposited at a speed of 1000 rpm for 60 s. 20 nm of C₆₀, 6 nm BCP and 100 nm aluminum were sequentially evaporated on top of PCBM layer under vacuum degree 10^{-7} mbar. The $J-V$ curves of the devices were measured at 295 K using a Keithley 2400 source meter under simulated AM 1.5 G solar illumination using a Steuernagel Solar constant 1200 metal halide lamp in a nitrogen-filled glove box. The light intensity was calibrated to be 100 mW cm⁻² by using a Si reference cell and correcting the spectral mismatch. A shadow mask (0.04 cm²) was used to exclude lateral contributions beyond the device area.

3.1.2. Film characterizations

Absorbance, XRD patterns and SEM measurements. The absorbance of the perovskite films was recorded on Shimadzu UV-vis-NIR spectrophotometer (UV 3600). XRD patterns were recorded in air on a Bruker D8 Advance X-ray diffractometer with a Cu K α source ($\lambda = 1.54 \text{ \AA}$) and a Lynxeye detector. SEM images of perovskite films were taken in vacuum on an FEI NovaNano SEM 650 with an acceleration voltage of 5 kV.

GIWAXS measurement. Grazing incidence wide-angle X-ray scattering (GIWAXS) measurements were performed using a MINA X-ray scattering instrument built on a Cu rotating anode source ($\lambda=1.5413 \text{ \AA}$). 2D patterns were collected using a Vantec500 detector (1024x1024 pixel array with pixel size 136x136 microns) located 93 mm away from the sample. The perovskite films were placed in reflection geometry at certain incident angles α_i with respect to the direct beam using a Huber goniometer. GIWAXS patterns were acquired using an incident angle of 2° in order to probe the thin film structure at an X-ray penetration depth of the entire film thickness. For an ideally flat surface, the value of the X-ray penetration depth (i.e. the depth into the

material measured along the surface normal where the intensity of X-rays falls to 1/e of its value at the surface) depends on the X-ray energy (wavelength λ), the critical angle of total reflection, α_c , and the incident angle, α_i , and can be estimated using the relation: $\Lambda = \frac{\lambda}{4\pi} \sqrt{\frac{2}{(\alpha_i^2 - \alpha_c^2)^2 + 4\beta^2 - (\alpha_i^2 - \alpha_c^2)}}$, where β is the imaginary part of the complex refractive index of the compound. The direct beam center position on the detector and the sample-to-detector distance were calibrated using the diffraction rings from standard silver behenate and Al_2O_3 powders. All the necessary corrections for the GIWAXS geometry were applied to the raw patterns using the FIT2D and the GIXGUI Matlab toolbox. The reshaped GIWAXS patterns, taking into account the inaccessible part in reciprocal space (wedge-shaped corrected patterns), are presented as a function of the vertical and parallel scattering vectors q_z and q_r . The scattering vector coordinates for the GIWAXS geometry are given by:

$$q = \begin{cases} q_x = \frac{2\pi}{\lambda} (\cos(2\theta_f) \cos(\alpha_f) - \cos(\alpha_i)) \\ q_y = \frac{2\pi}{\lambda} (\sin(2\theta_f) \cos(\alpha_f)) \\ q_z = \frac{2\pi}{\lambda} (\sin(\alpha_i) + \sin(\alpha_f)) \end{cases}$$

where $2\theta_f$ is the scattering angle in the horizontal direction and α_f is the exit angle in the vertical direction. The parallel component of the scattering vector is thus calculated as $q_r = \sqrt{q_x^2 + q_y^2}$. [151]

PL measurement. The samples were excited at laser wavelength 400 nm by the second harmonic of a mode-locked Ti:sapphire (Mira 900) laser delivering pulses of 150 fs. The laser repetition rate is 76 MHz; a pulse picker was inserted in the optical path to reduce the repetition rate. A 150 mm focal length lens was used to focus the beam, and the emission was collected by a spectrometer with a 50 lines mm^{-1} grating. The steady-state PL was recorded with a CCD camera from Hamamatsu (Hamamatsu, Japan). Time-resolved PL was measured with the streak camera.

3.2. Results and discussion

3.2.1. Solar cells with different hole transport layers

3.2.1.1. Film morphology and structure

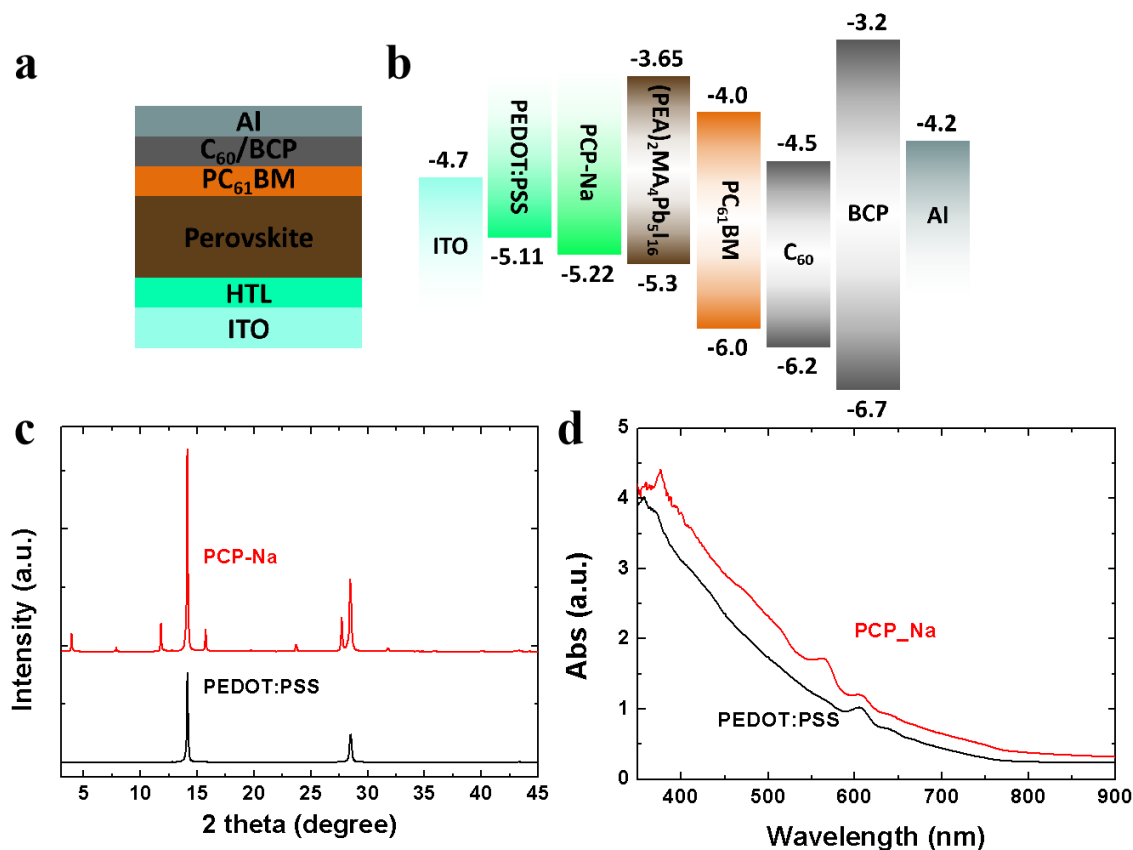


Figure 3.1 (a) device structure of the solar cells, (b) work function of different layers correlated to device structure, (c,d) XRD patterns and UV-vis absorption of the different samples.

The device structure is shown in **Figure 3.1a** and **Figure 3.1b** shows the related work function respectively. X-ray diffraction (XRD) patterns are shown in **Figure 3.1c**. Diffraction patterns for both the thin films on PEDOT: PSS and PCP-Na demonstrate oriented growth. The two main peaks at 2θ around 14.17° and 28.54° are assigned to (110) and (220) facets respectively. The small peaks in PCP-Na sample at 3.96° , 7.88° , 11.82° , 15.74° , 19.72° , 23.70° , 27.73° and 31.77° are correlated to (002), (004), (006),

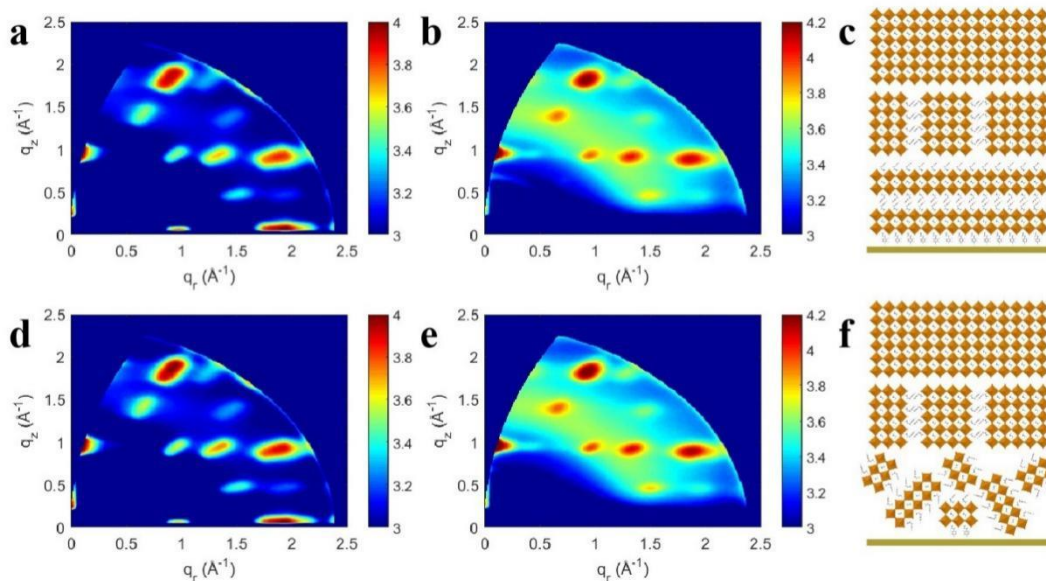


Figure 3.2 GIWAXS images of PEDOT: PSS sample (a, b) and PCP-Na sample (d, e) investigated at 0.25° and 2° , respectively and related structure of the thin films (c, f).

(008), (0010), (0012), (0014) and (0016) facets, indicating the presence of $n=2$ member. The optical absorbance of thin films grown on different HTLs is shown in **Figure 3.1d**. The small ripples at 564 nm, 608 nm and 643 nm belong to low $n=2, 3$, and 4 members respectively, indicating different phases exist in the thin films.

The pattern for the thin film on PCP-Na exhibits higher crystallinity than on PEDOT: PSS, indicating PCP-Na as supporting layer is better for 2d perovskite crystallization. To furtherly confirm the growth orientation of the thin films, grazing incidence wide-angle X-ray scattering (GIWAXS) measurements were carried on. Results are shown in **Figure 3.2**, with all the panels showing sharp, discrete Bragg spots. At the lowest incident angle of 0.25° , probing the first several tens of nanometers on the top surface of the thin films, the images of thin films grown on PEDOT: PSS (**Figure 3.2a**) and PCP-Na (**Figure 3.2c**) are very similar. The Bragg spot at around $q_z=1 \text{ \AA}^{-1}$ represents the (110) plane grown along in-plane direction which is much stronger than $q_y=1 \text{ \AA}^{-1}$ representing (110) plane grown along out-of-plane direction. It means that the (110) plane is mainly growing along in-plane direction indication the $[\text{PbI}_6]^{4-}$

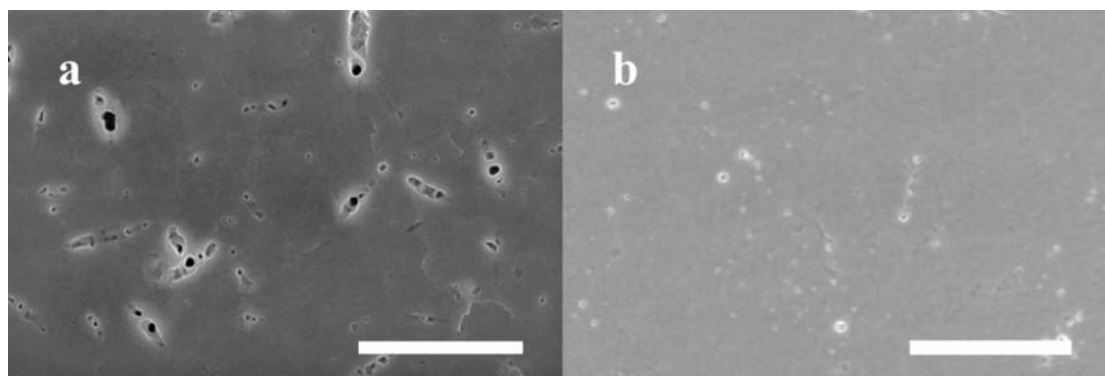


Figure 3.3 SEM images of 2D perovskite thin films on PEDOT: PSS (a) and PCP-Na (b) substrates, the scale-bar is 2 μm .

octahedron layers are perpendicular to the substrates. The results measured at highest incident angle of 2° , probing the last several tens of nanometers on the bottom surface of the thin films, are shown in **Figure 3.2b** (PEDOT: PSS) and **3.2d** (PCP-Na). Still they are very similar but in **Figure 3.2b**, at around $q_z=0.75 \text{ \AA}^{-1}$, there appears a small Debye-Scherrer ring indexed as the (006) plane of $n=2$ phase. But the Debye-Scherrer ring means that at this part of the thin films, the “wells” and “barriers” are growing randomly way lead to form defects determined to charge transport from bottom to upper layers.

The morphology of the thin films grown on PEDOT: PSS and PCP-Na were measured by scanning electron microscope (SEM). As shown in **Figure 3.3a**, $\text{PEA}_2\text{MA}_4\text{Pb}_5\text{I}_{16}$ grown on PEDOT: PSS substrate has some large pinholes and obvious grain boundaries on the film, which may cause current leakage by forming shunts and trap-assisted recombination. Furthermore, the HTL and ETL may contact each other directly through pinholes, short-circuiting the device. On the other hand, in **Figure 3.3b**, the film grown on PCP-Na shows much better quality, less pinholes and more uniform surface which may help to reduce trap states.

3.2.1.2. Photoluminescence measurements

To further understand the charge recombination process in perovskite thin films,

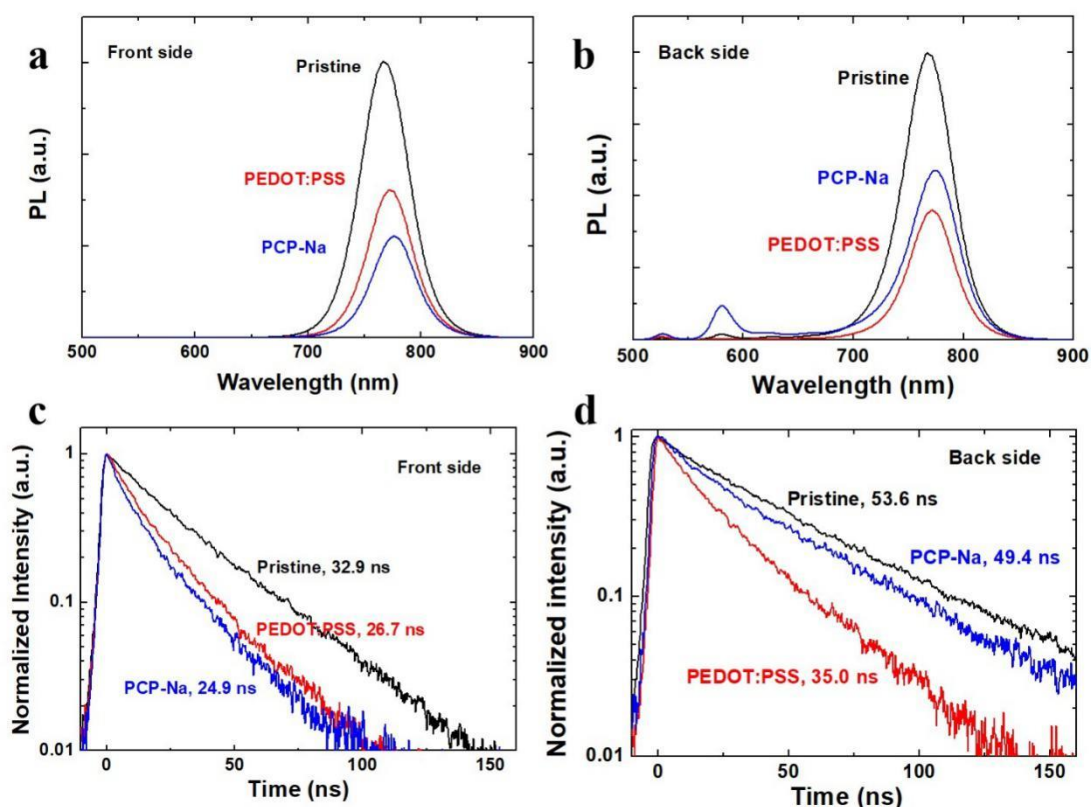


Figure 3.4 (a) and (b) are steady state photoluminescence of 2D perovskite thin films in DMF solvent precursors grown on different substrates, glass, glass/PEDOT:PSS and glass/PCP-Na. Front side means on perovskite side, back side means on glass side. (c) and (d) are time resolved PL spectra correspond to (a) and (b).

steady state and time-resolved photoluminescence (TRPL) measurements were performed on pristine perovskite on glass and on different HTLs. Results are shown in **Figure 3.4**. Steady state PL (**Figure 3.4a, b**) intensity, measured from the two different sides of the samples, is reduced in the presence of HTLs, indicating efficient charge transfer from perovskite to HTL. In **Figure 3.4b**, the spectra measured from backside display weak peaks at 526 nm and 581 nm which are corresponding to $n=1$ and $n=2$ phase (details in semilogarithmic plots of **Figure A1**). The TRPL spectra measured from frontside (**Figure 3.4c**) are very similar to samples on different HTLs. The lifetime are 26.7 ns for PEDOT: PSS sample and 24.9 ns for PCP-Na sample. But the PL decay measured from backside, the lifetime for PCP-Na sample is 49.4 ns

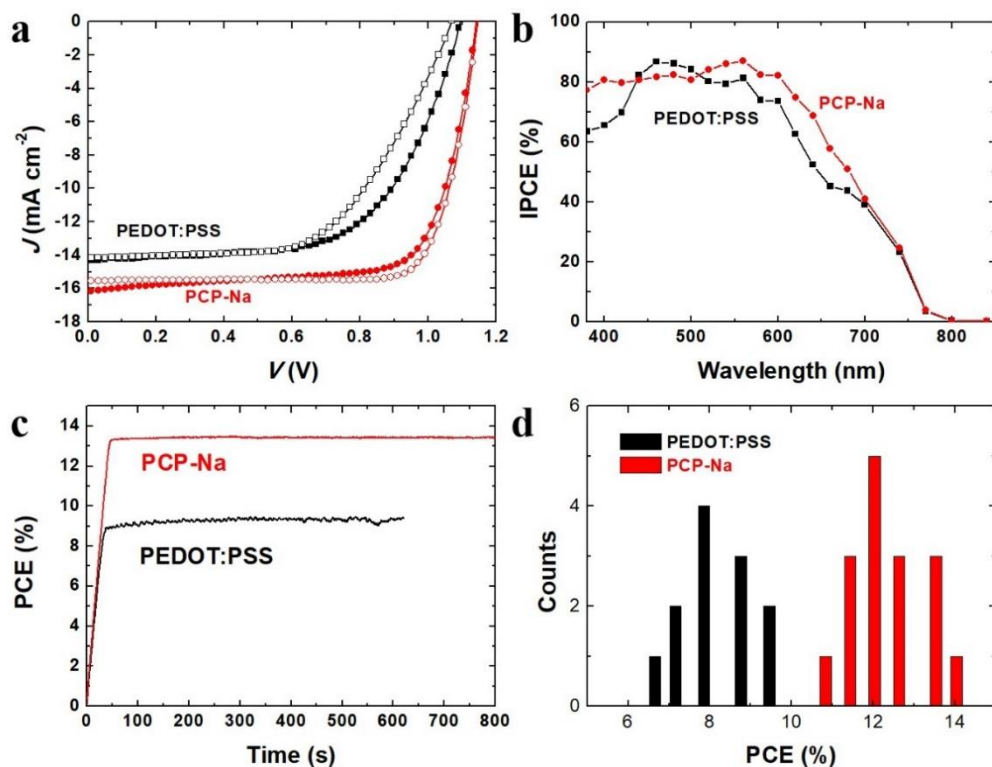


Figure 3.5 (a) J - V curves, (b) IPCE spectra, (c) Max power point track, and (d) PCE distribution of devices using different HTL.

Device	V_{oc} (V)	J_{sc} (mA cm ⁻²)	FF	PCE (%)
PEDOT: PSS F	1.09	14.30	0.61	9.62
PEDOT: PSS R	1.07	14.16	0.58	8.76
PCP-Na F	1.15	15.54	0.79	14.12
PCP-Na R	1.14	16.17	0.72	13.35

Table 3. Performance parameters of devices using different HTL.

which is significantly longer than PEDOT: PSS sample 35.0 ns. This effect may attribute to the less oriented growth of PEDOT: PSS film, leading to the low efficient charge transport and more recombination of charge carriers.

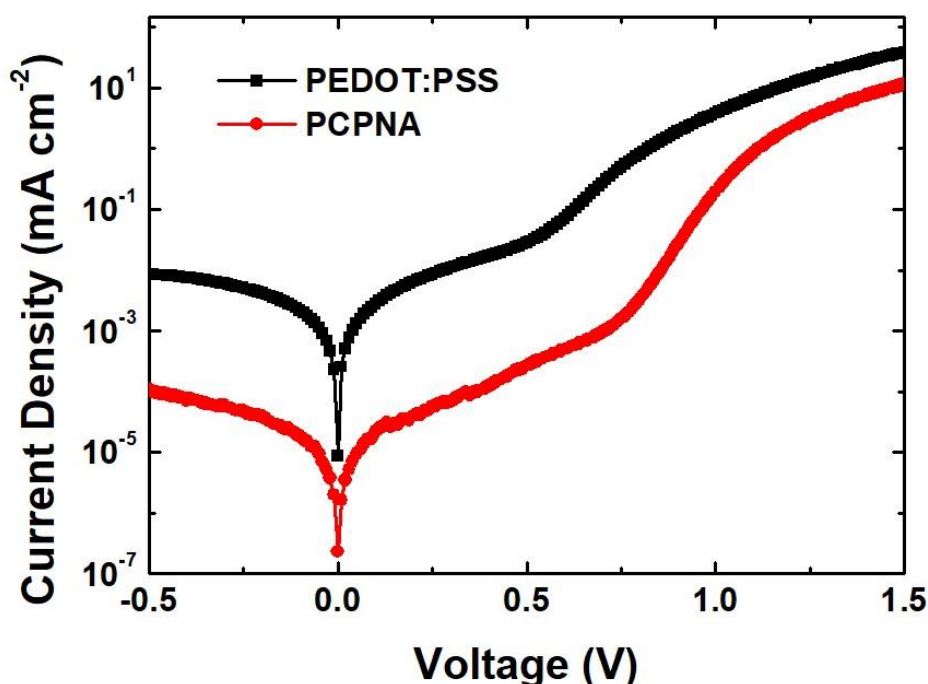


Figure 3.6. Dark J - V curves of two different solar cell devices.

3.2.1.3. Device performance

To investigate the solar cell performance, a p-i-n architecture was employed, namely ITO/(PEDOT: PSS or PCP-Na)/Perovskite/PCBM/C₆₀/BCP/Al. **Figure 3.5a** shows the J - V curve of the solar cells using different HTLs and the relevant parameter details are summarized in **Table 3**. The best performance is obtained for the device using PCP-Na as HTL, with a V_{OC} value of 1.15 V, a J_{SC} of 15.54 mA cm⁻², a FF of 0.79 and a PCE of 14.12% in forward scan. In reverse scan, the device shows a V_{OC} of 1.14 V, a J_{SC} of 16.17 mA cm⁻², an FF of 0.71 and a PCE of 13.35%. As a comparison, the device using PEDOT: PSS as HTL shows a V_{OC} of 1.09 V, a J_{SC} of 14.30 mA cm⁻², a FF of 0.61 and a PCE of 9.62% in forward scan and a V_{OC} of 1.07 V, a J_{SC} of 14.16 mA cm⁻², a FF of 0.58 and a PCE of 8.76% in reverse scan. The tracks of max power point of the devices are shown in **Figure 3.5b**, the steady state PCE are 13.44% and 9.42% for PCP-Na and PEDOT: PSS, respectively. **Figure 3.5c** shows the external

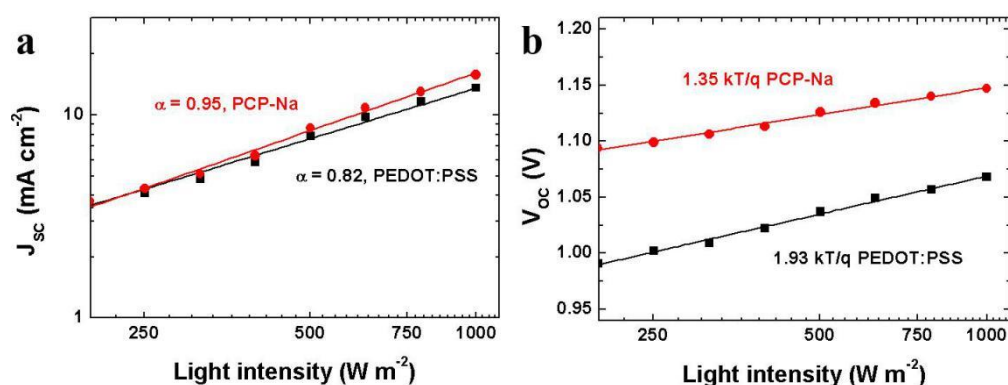


Figure 3.7 Light intensity dependence of J_{SC} (a) and V_{OC} (b) of the devices using different HTL.

quantum efficiency spectra of the different devices. The current density integrated from the spectra are 15.97 mA cm^{-2} and 14.70 mA cm^{-2} corresponding to PCP-Na and PEDOT: PSS respectively, which closely match the J_{SC} value obtained by J - V curves.

Dark current refers to the reverse direct current generated when the P-N junction is under reverse bias conditions with no incident light. It is generally caused by the diffusion of carriers or defects on the surface and inside of the device and impurities. The principle of diffusion is that inside the P-N junction, there are many electrons in the N region, and there are many holes in the P region. Because of the difference in concentration, electrons in the N region are diffused into the P region, and holes in the P region are diffused into the N region, despite the P-N junction. The built-in electric field prevents this diffusion, but in reality, the diffusion has been going on, only to achieve a dynamic equilibrium, which is the formation of diffusion current. In addition, when there are defects on the surface and inside of the device, the defect level acts as a recombination center. When electrons and holes are captured by the defect level, the movement of carriers forms an electric current. The impurity also functions as a recombination center in the device, with the same principles as defects. The dark J - V curves (**Figure 3.6**) are showing under dark condition, PCP-Na device generates dark current much smaller than PEDOT: PSS samples. This indicates that the PCP-Na device has less defect density than PEDOT: PSS one which is

corresponded to the SEM and GIWAXS measurements.

To further understand the recombination in presence of different HTL, we measured the light-intensity dependence of J_{SC} and V_{OC} . The results are shown in **Figure 3.7**. In **Figure 3.7a**, the J_{SC} to light intensity plot of PCP-Na has a slope closer to 1, and **Figure 3.7b** shows the semilogarithmic plots of the V_{OC} to light intensity of the devices, the PCP-Na device exhibits a much smaller slope (1.35 kT q^{-1}) than PEDOT:PSS device (1.93 kT q^{-1}). These results indicate more equal trapping recombination of electrons and holes occurs in PEDOT:PSS device, which is corresponded to the SEM and GIWAXS measurements. The air stability of the thin films was also evaluated. In **Figure A2**, after 80 days in the air, the thin films still remain good crystallization and the images of the thin films exhibit one edge of the film on PEDOT:PSS turn yellow while the film on PCP-Na is still dark brown.

In addition, I also applied this new HTL in 3D lead perovskite to see if it could improve the performance of solar cell devices. $(\text{FAPbI}_3)_{0.87}(\text{MAPbBr}_3)_{0.17}$ was employed as the active perovskite layer. The device performance is improved from PCE of 12.32% (PEDOT:PSS) with J_{SC} 19.75 mA cm^{-2} , V_{OC} 0.87 V, FF 0.72 to PCE of 15.73% (PCP-Na) with J_{SC} 21.03 mA cm^{-2} , V_{OC} 0.99 V, FF 0.75 (J - V curves in **Figure A3**).

3.2.2. Comparison of two deposition methods for mixed solvent

3.2.2.1. Film morphology and structure

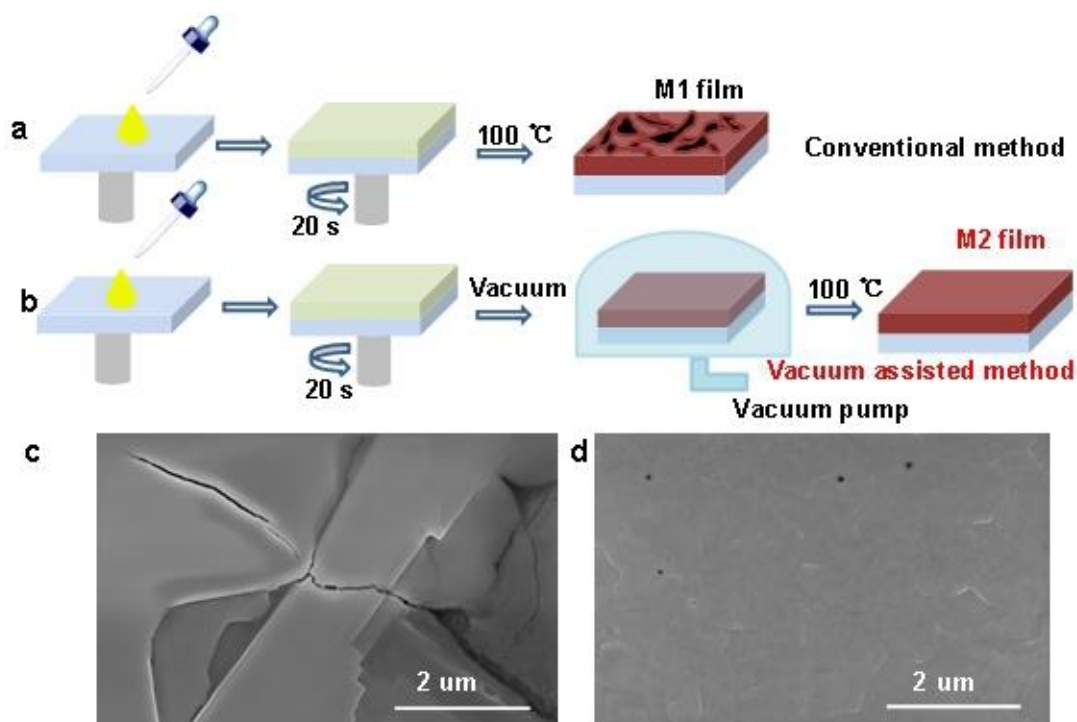


Figure 3.8 Preparation scheme and SEM images of conventional method (a,c) and vacuum assisted method.

In the conventional method, the wet films were put on a hot plate at 100 °C immediately after spin-coating, and they turned dark red after 10 seconds due to fast evaporation of the solvent (**Figure 3.8a**). These films appear very rough, non-uniform and not very reflective to the eye. In vacuum assisted method, the films were placed in vacuum immediately after the same spin-coating procedure, after 5 minutes in the chamber they appear as dark red, uniform and very reflective (**Figure 3.8b**). The films were then put on the hot plate at 100 °C for 10 min. The morphology of the thin films is shown in **Figure 3.8c, d**. The conventional sample film (denoted as M1) forms large grains but also with very large cracks and pinholes, resulting open grain boundaries and increased defect densities. Differently, vacuum sample film (denoted as M2).

The absorption spectra of the thin films in **Figure 3.9** exhibit an absorption onset at around 780 nm resembling of 3D MAPbI₃ films. They show several higher energy

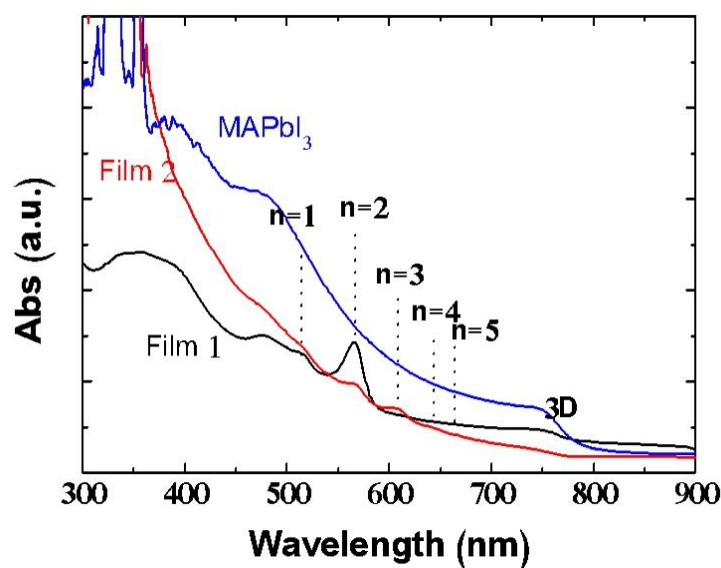


Figure 3.9 UV-vis absorption of M1 film (black), M2 film (red) and 3D MAPbI₃ film.

peaks due to strong excitonic absorption associated with 2D phases. These features suggest that the quasi-2D films consist of multiple perovskite phases. Perovskite M1 film exhibits much stronger absorption corresponding to the n=2 phase at 569 nm and weak absorption consistent with the n=1 phase at 514 nm. Perovskite M2 film displays a much weaker absorption from the n=1 and 2 phases, but absorption corresponding to the n=3 (609 nm), 4 (640 nm) and 5 (663 nm) phases are observed. Such distinctive features in the absorption spectra imply the presence of domains of different phase composition in these RPP films.

The two type of perovskite films display rather distinct X-ray diffraction (XRD) patterns (**Figure 3.10**). M1 film exhibits two intense diffraction peaks at $2\theta = 14.15^\circ$ and 28.48° , which are assigned to the (110) and (220) crystallographic planes, respectively. It also exhibits several evenly spaced peaks at $2\theta = 3.96^\circ, 7.88^\circ, 11.82^\circ, 15.76^\circ, 19.72^\circ, 23.70^\circ$ and 27.725° , which are indexed as the (002) (004)...to (0014) planes of the n=2 phase. In addition, another two very weak peaks at low reflection angles ($2\theta = 5.48^\circ$ and 10.72°) are assigned to the (002) and (004) planes of the n=1 phase. The n=3, 4, 5 phases do not show any peaks at low diffraction angle ($2\theta <$

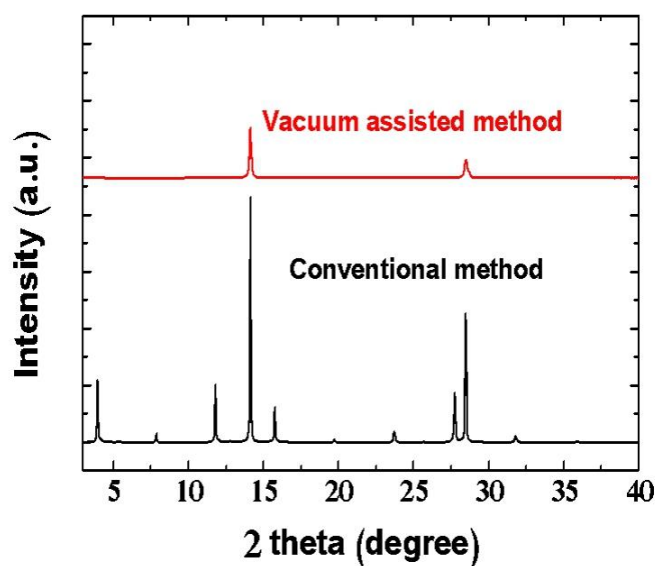


Figure 3.10 XRD patterns of M1 film (black) and M2 film (red).

14.15°), most probably due to their preferential orientation. M2 film exhibits two dominant peaks from the (110) and (220) planes, indicating preferential orientation of the perovskite domains. Diffraction peaks from the $n=1$ and 2 phases are visible but very weak due to their small volume fractions. Similar to the M1 film, the $5 \geq n \geq 3$ phases have the same preferential orientation, exhibiting dominant (110) and (220) planes.

In order to probe the orientation of the perovskite phases with respect to the substrate, we carried out grazing incidence wide-angle X-ray scattering (GIWAXS) measurements at incident angles of 0.25° and 2° (**Figure 3.11**). Both M1 and M2 films show remarkably sharp Bragg spots at different X-ray penetration depths. Indexing the intense Bragg spot at $q_z \approx 0.89 \text{ \AA}^{-1}$ confirms that the infinity $\geq n \geq 3$ phases in these films are oriented with their (110) planes packing in the out-of-plane direction, thus the octahedron layers are perpendicular to the substrate. The Bragg spot at $q_y \approx 0.89 \text{ \AA}^{-1}$ assigned to the in-plane-oriented (110) plane is much weaker than that at $q_z \approx 0.89 \text{ \AA}^{-1}$, indicating the dominant vertical orientation of the infinity $\geq n \geq 3$ phases. This is a common feature of the M1 and M2 films.

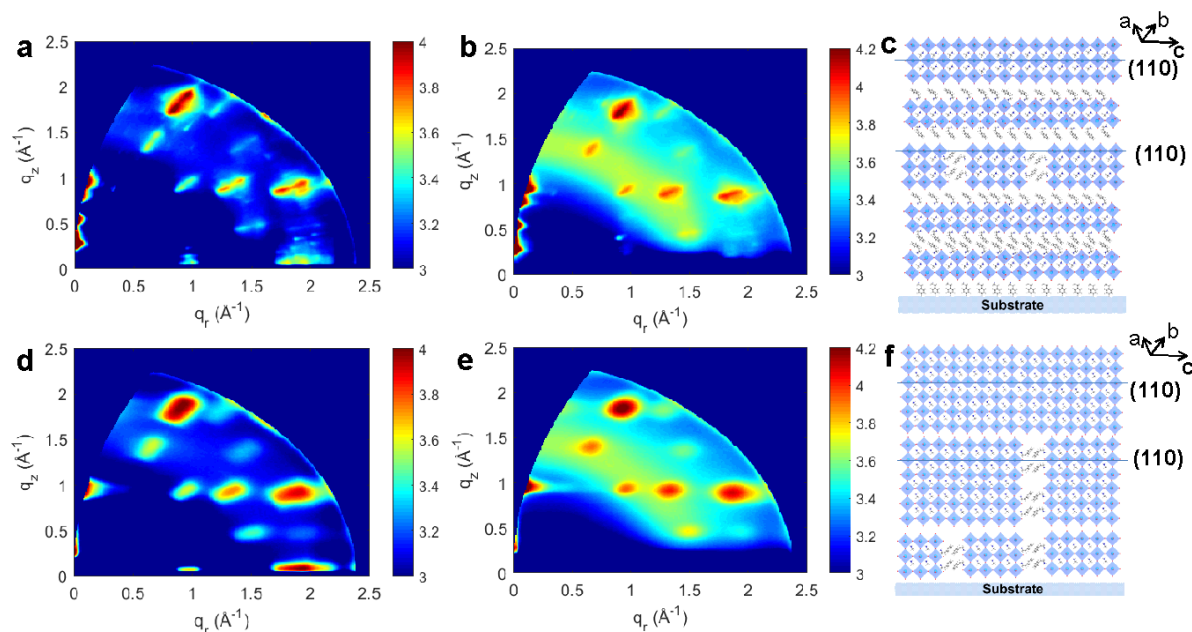


Figure 3.11 GIWAXS images of M1 film (a,b) and M2 film (c,d), measured on 0.25 and 2, which is on bottom and top of the film, respectively. Structure illustration of M1 film (c) and M2 film (f).

The M1 film shows intense Bragg spots at $q_z \approx 0.25 \text{ \AA}^{-1}$, 0.54 \AA^{-1} and 0.78 \AA^{-1} in the entire film, which are indexed as the (002), (004) and (006) planes of the $n=2$ phase with octahedron layers parallel to the substrate (**Figure 3.11a-c**). In addition, a Bragg spot at $q_z \approx 0.39 \text{ \AA}^{-1}$ is observed belonging to the (002) plane of the $n=1$ phase parallel to the substrate. Since PEA organic double layers is a potential barrier for charge transport, such preferential parallel alignment of the $n \leq 2$ phases inhibits charge transport and collection of charges in the vertical direction of the solar cells. The M2 film does not show any diffraction spots from $n=1$ and 2 phases at shallow X-ray penetration depth (**Figure 3.11d-f**). Very weak diffraction signal of the $n=2$ phase is observed in the out-of-plane direction at the bottom of the film (**Figure 3.11e**) due to its small volume fraction. Therefore, the vertically oriented octahedron layers in M2 film, facilitate charge transport and collection in the corresponding solar cells.

3.2.2.2. Device performance

Device	V_{oc}/V	$J_{sc}/\text{mA cm}^{-2}$	FF	PCE/%
PEDOT_M1 F	0.81	7.97	0.37	2.40
PEDOT_M1 R	0.74	7.93	0.30	1.79
PEDOT_M2 F	1.06	15.50	0.65	10.57
PEDOT_M2 R	1.06	15.82	0.66	11.07
PCP-Na_M1 F	0.99	6.31	0.53	3.31
PCP-Na_M1 R	0.96	6.63	0.57	3.65
PCP-Na_M2 F	1.10	17.09	0.73	13.70
PCP-Na_M2 R	1.10	17.52	0.73	14.14

Table 4. Devices with perovskite films M1 and M2 on different hole extraction layers under one sun condition.

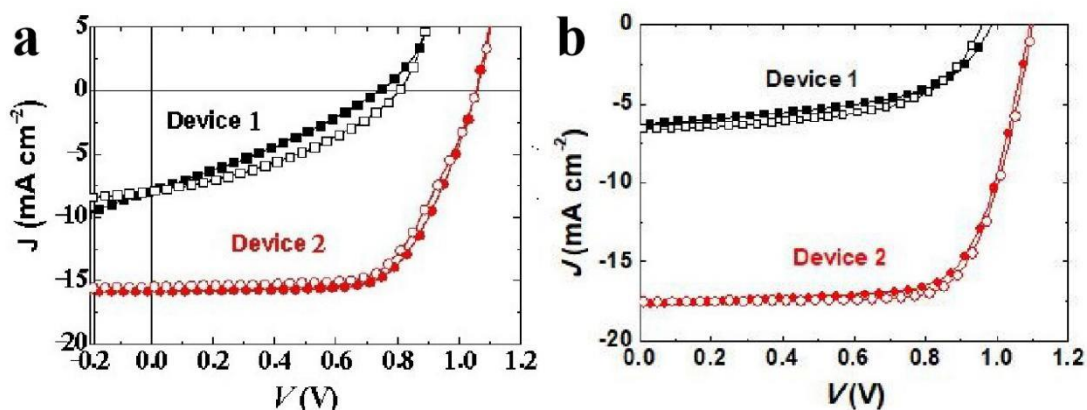


Figure 3.12. J - V curves of devices using different hole transport layers, PEDOT: PSS (a) and PCP-Na (b). M1 device film shown in black and M2 film device shown in red.

The device structure is same with the one shown in **Figure 3.1a**. Both M1 and M2 are employed in PEDOT: PSS and PCP-Na devices. Results are obvious that M2 devices

possess higher PCE than M1 devices (**Figure 3.12**). In PCP-Na devices, device with M2 film exhibits a V_{OC} valued of 1.10 V, a J_{SC} of 17.09 mA cm⁻², an FF of 0.73 and a PCE of 13.70% in forward scan. In reverse scan, the device shows a V_{OC} of 1.10 V, a J_{SC} of 17.52 mA cm⁻², an FF of 0.73 and a PCE of 14.14%. While the M1 device shows a V_{OC} of 0.985 V, a J_{SC} of 6.31 mA cm⁻², a FF of 0.53 and a PCE of 3.31% in forward scan and a V_{OC} of 0.959 V, a J_{SC} of 6.63 mA cm⁻², a FF of 0.57 and a PCE of 3.65% in reverse scan. In PEDOT: PSS devices, they show the same trend with M2 device PCE 10.57% (11.07%), much higher than M1 2.40% (1.79%). Detailed data of J-V curves are summarized in **Table 4**.

3.2.2.3. Conclusion

In this chapter, we developed a vacuum-assisted fabrication method for quasi-2D perovskite (PEA₂MA₄Pb₅I₁₆) thin films which is rather useful to improve the film morphology with mixed solvent precursors. Films deposited in this method have shown very smooth and reflective surface with compact and less grain boundary morphology. It also can improve the phase distribution and growth orientation to become more preferable for charge transport at in-plane direction. The stability of those thin films can be up to more than 2 months with little degradation.

Meanwhile, a novel hole transport layer, PCP-Na was employed to replace PEDOT: PSS. PCP-Na is pH neutral and possess an electrical conductivity (1.66×10^{-3} S cm⁻¹) a little bit higher than PEDOT: PSS (1.35×10^{-3} S cm⁻¹). The HOMO level of PCP-Na (-5.22 eV) is closer to the valence band of PEA₂MA₄Pb₅I₁₆ perovskite (-5.3 eV) comparing to PEDOT: PSS (-5.11 eV) which results in the enhancement of open circuit voltage of solar cells. With these improvements, PCE of solar cells was improved beyond 14%.

4. Photophysics of 2D tin perovskite

Different from the lead counterpart, studies on tin perovskite are not so many. Although the approximate 10% has appealed plenty of studies, there still exists various issues need to be solved and the photophysics needs to be elucidated.[152-157] In this part, 2D tin perovskites $\text{BA}_2\text{MA}_{n-1}\text{Sn}_n\text{I}_{3n+1}$ with different n numbers were fabricated and the photogenerated carriers were studied through ultrafast systems to understand the carrier behaviors in the perovskite.

4.1. Experimental section

4.1.1. Synthesis of $\text{BA}_2\text{MA}_{n-1}\text{Sn}_n\text{I}_{3n+1}$ thin films

The thin films were deposited by spin-coating method. Stoichiometric MAI, BAI and SnI_2 were dissolved in DMF, that is 0:2:1 for BA_2SnI_4 ($n=1$), 1:2:2 for $\text{BA}_2\text{MASn}_2\text{I}_7$ ($n=2$) and 2:2:3 for $\text{BA}_2\text{MA}_2\text{Sn}_3\text{I}_{10}$ ($n=3$). The concentration of Sn^{2+} was 0.5 M. The glass substrates were cleaned by soap water with ultrasonic at 50°C for 10 min, then washed by deionized water. After that, the substrates were washed by acetone and isopropanol with ultrasonic for 10 min subsequently. The precursor solutions were then heated to 70°C for 30 min and spin-coated at a speed of 3000 rpm for 30 s with an acceleration of 1500 rpm/s. Then the thin films were annealed at 75°C for 10 min.

4.1.2. Film characterization

X-ray diffraction. X-ray diffraction measurement was carried at room temperature using a Bruker D8-Discover diffractometer (Bragg-Brentano geometry) for crystals with parallel beam geometry and Cu K α wavelength ($\lambda=1.5418\text{\AA}$), operated at 40 kV and 40 mA using a step size of 0.05° and a time per step of 1 s. For $n=1$ sample, the Bragg angle was scanned from 5 to 40. For $n=2$ sample, it was 3 to 40 and 2 to 40 for $n=3$ sample.

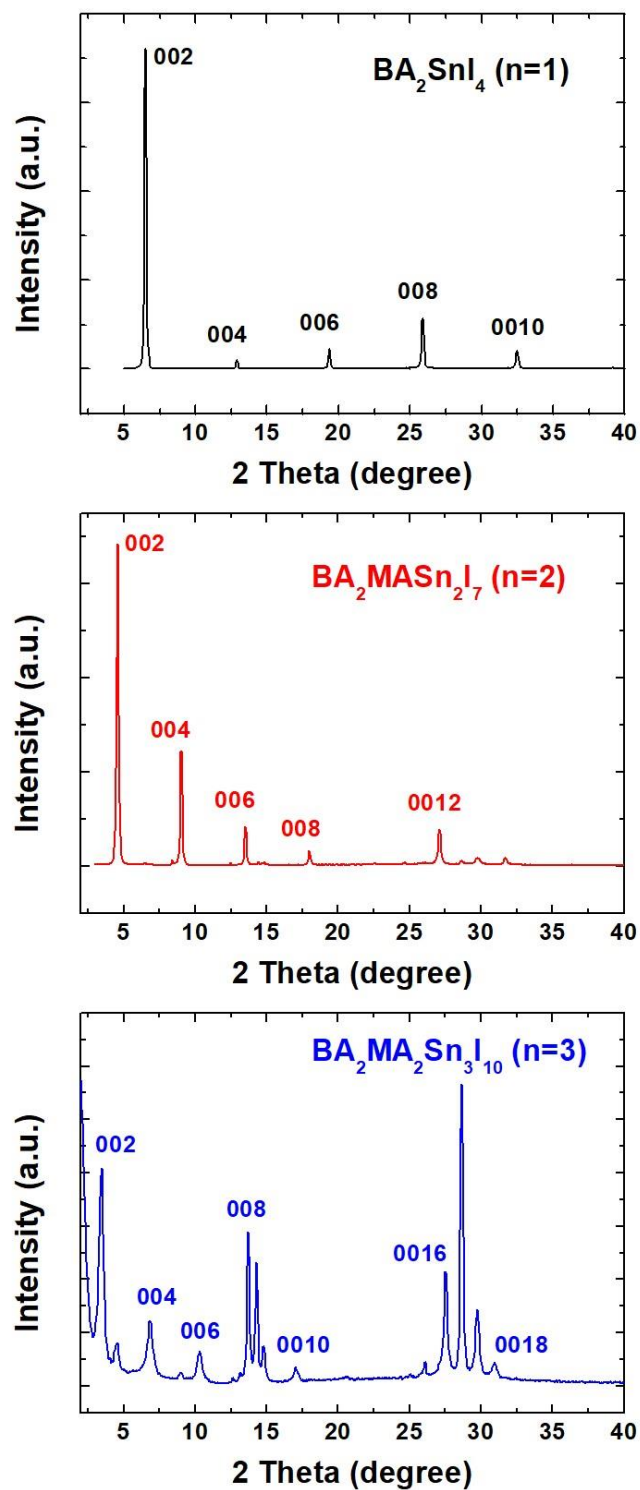


Figure 4.1. XRD patterns for BA_2SnI_4 ($n=1$), $BA_2MASn_2I_7$ ($n=2$) and $BA_2MA_2Sn_3I_{10}$ ($n=3$) thin films deposited by normal spin-coating method, arranged from up to down.

AFM and UV-vis absorption. Film morphology and thickness is roughly measured

by atomic force spectroscopy with a NT-MDT Solver P47H-Pro in semicontact mode by a high-resolution non-contact silicon tip. Absorption spectra of perovskite films are measured with a UV/Visible Perkin Elmer Lambda 950 spectrometer. The wavelength range is from 350nm to 1100nm.

Time-resolved photoluminescence. Since tin perovskites are even more unstable than lead perovskites, all the samples were measured in vacuum circumstance. Samples were excited with a regenerative amplified laser (Coherent Libra) delivering 130-fs-long pulses at a repetition rate of 1 KHz. Photoluminescence was dispersed with a grating spectrometer (Princeton Instruments Acton SpectraPro 2300i equipped with a 50 gr mm⁻¹ grating blazed) and detected by a streak camera (Hamamatsu).

4.2. Results and discussion

4.2.1. Synthesis for single phase

Generally, for 2D perovskites, it is rather tough to get a very pure phase of target material. The n=1 sample, since there is only large organic cation, can be pure phase. When trying to increase the n number, as described in chapter 3, the n=5 sample is actually a mixture of 3D and different 2D phases. Here, in this experiment, first of all, all the films were deposited by the normal method and XRD results are shown in **Figure 4.1**.

The n=1 is obvious pure material, and the peaks at 2θ of 6.5°, 12.9°, 19.35°, 25.9° and 32.5° can be indexed as the (002), (004), (006), (008) and (0010) planes respectively. In n=2 sample, things become different. The main peaks at 4.55°, 9.05°, 13.55°, 18° and 27.1° belong to (002), (004), (006), (008) and (0012). Besides, there are also some weak peaks, only the two ripples at 22.55° and 31.7° are (0010) and (0014) of n=2 material. Other ripples are peaks from n=1 or maybe because randomly growth orientation reflectivity. Considering the limit of detection of XRD is 2% and the intensity of the ripples, we can consider the n=2 as a 97% pure material. But for the n=3 sample, the XRD pattern shows many irregular peaks of this film through this

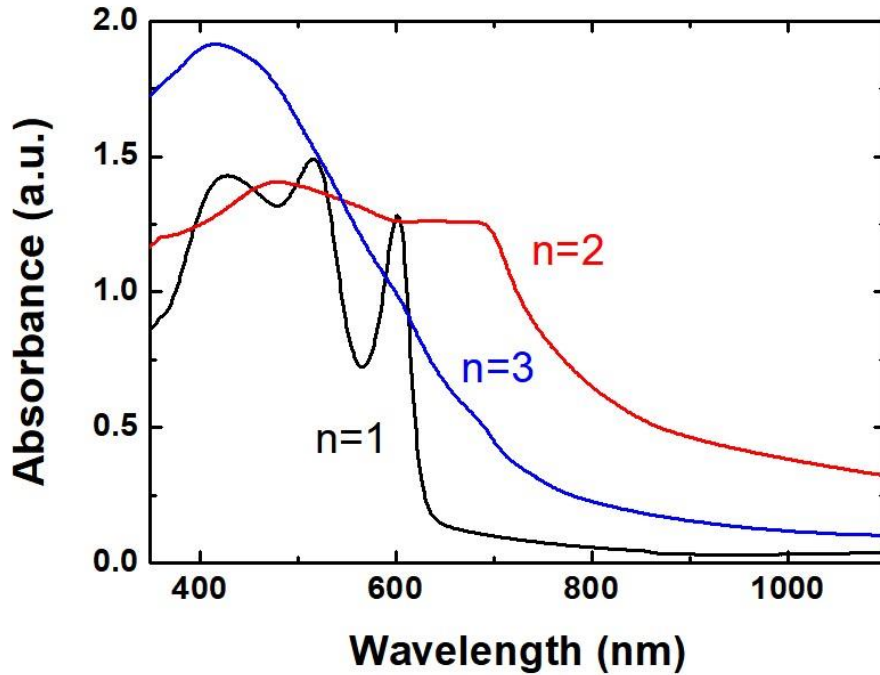


Figure 4.2. Optical absorption of 3 different samples.

deposition method. Despite the (00 l) planes of n=3 phase, some peaks of n=1 and 2 phases are also observed, implying the film is a mixture of different phases.

4.2.2. Optical absorption and free energy

For thin films samples, there is an equation to describe the absorption:

$$I_d = I_0 e^{-\alpha d} \quad (4.1)$$

where I_d is the transmission light, I_0 is the incident light, α is the absorption coefficient of the material, d is the thickness of the film, that is the distance of light passing the sample. As seen in **Figure 4.2**, the Y axis is absorbance, which is given by $\log_{10}(I_0/I_d)$. The shift up of n=2 sample from 750 to 1100 nm might be the roughness of the film (**Figure B1**). The light scatters when arriving on the surface of the film. Since the n=3 sample is a mixture, 2 very small shoulder peaks can be seen at the same wavelength of n=1 and 2 samples which also confirms the mixture phases of the sample. **Figure 4.3** shows the degradation of the samples, from the absorption spectra,

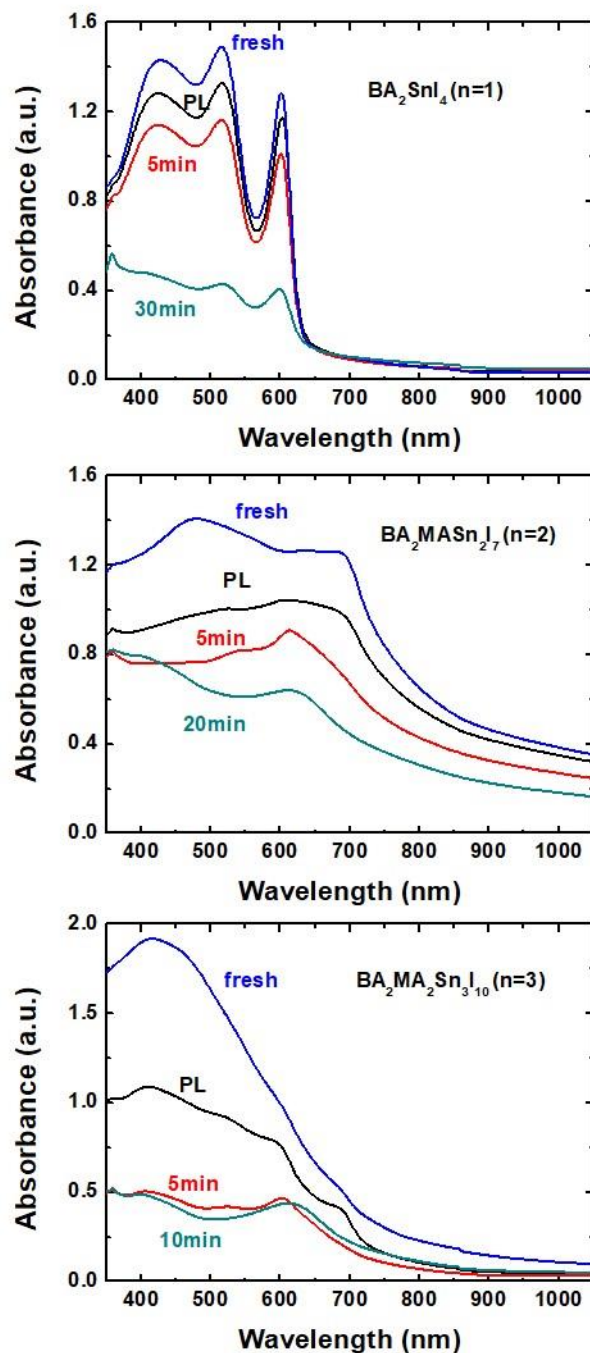


Figure 4.3. Optical absorption degradation of 3 different samples. Blue is fresh sample, black is after TRPL measurement in vacuum, others are exposed to air:

we can see all the samples degrades very fast in the air circumstance. Within 30 min, the absorption of all the samples degrade more than 50%.

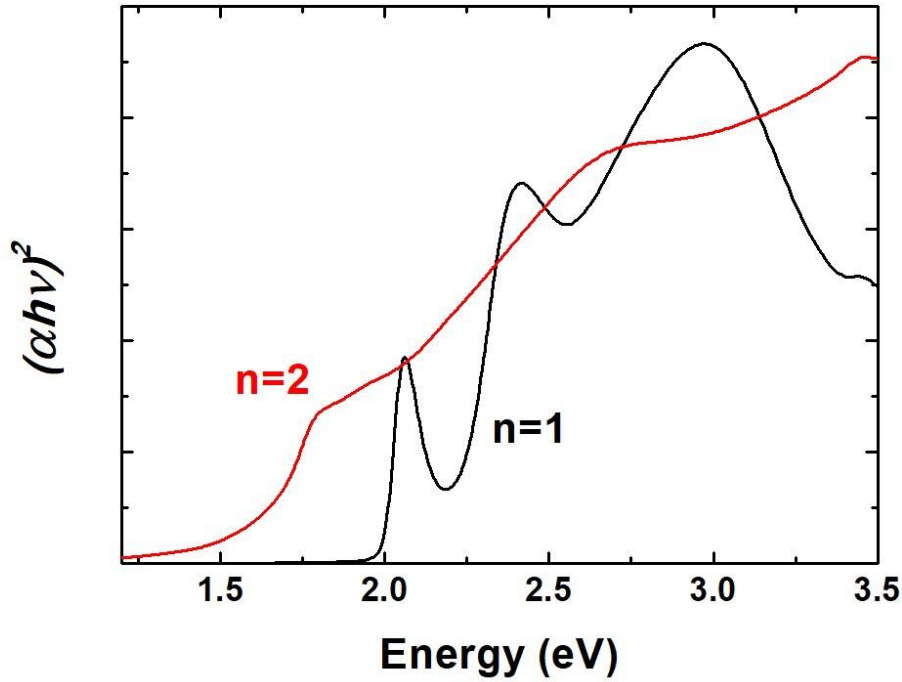


Figure 4.4. Tauc plot from absorption of $n=1$ and 2 samples.

To determine the bandgap of the materials, Tauc to Energy plot of the samples are extracted from the absorbance data.[158] The Tauc and Davis-Mott relation can be written by

$$(\alpha h\nu)^n = K(h\nu - E_g) \quad (4.2)$$

This relation is usually used to probe the optical bandgap energy for materials. In this equation, α is the absorption coefficient, $h\nu$ is the photon energy, K is an energy independent constant, E_g is the optical bandgap energy and n represents the nature of transition. Its value is fixed, 2 for direct allowed transition, 0.5 for indirect allowed transition, 2/3 for direct forbidden transition and 1/3 for indirect forbidden transition. For the Y axis, $(\alpha h\nu)^n$, $h\nu$ can be given by $1240/\text{wavelength}$ with unit eV ; α , with the Beer-Lambert absorption equation, can be given by $2.303 \cdot \text{absorbance}/d$ with unit cm^{-1} , and for these 2D tin perovskite samples, the n is 2. The X axis is just $h\nu$. Thus, we extract the Tauc plot data from absorbance data. **Figure 4.4** shows the Tauc plot of

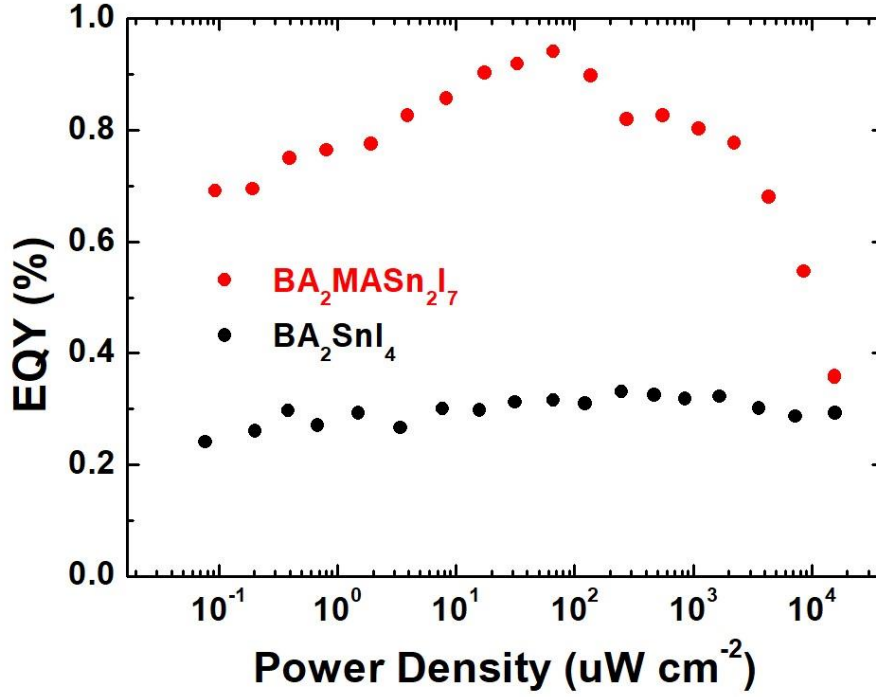


Figure 4.5. External photoluminescence quantum yield as a function of excitation intensity of $n=1$ and 2 samples.

the $n=1$ and $n=2$ samples and from the absorption peak we can know the bandgap should be 2.00 eV and 1.72 eV respectively.

The free energy (μ_{oc}) of the perovskites are given by optical method with the external photoluminescence quantum yield (EQY).[159] The μ_{oc} is equal to the energy splitting of quasi-fermi level of electrons in conductive band and holes in valence band.[160, 161] According to the Kirchhoff's law of radiation, which represents the detailed balance between emission and absorption, generalized by Würfel to account for non-equilibrium electron and hole populations[162]:

$$J_{PL} = \int \alpha(\omega) \frac{\Omega}{4\pi^2 \hbar^3 c_0^2} \frac{(\hbar\omega)^2}{e^{\frac{\hbar\omega - \mu}{kT}} - 1} d(\hbar\omega) \approx J_{0,rad} e^{\frac{\mu}{kT}} \quad (4.3)$$

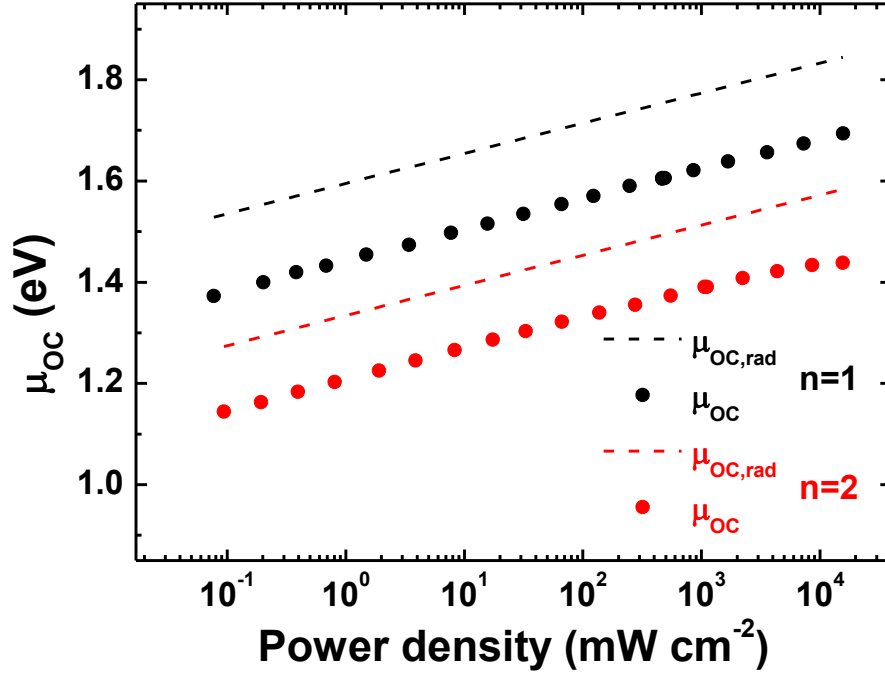


Figure 4.6. Free energy (μ_{OC}) and maximum ($\mu_{OC,rad}$) as a function of excitation intensity of $n=1$ and 2 samples.

where J_{PL} is the emitted photon current density, which is proportional to the external photoluminescence intensity; $\alpha(\omega)$ is absorptivity depending on the absorption coefficient and thickness of the sample; Ω is the effective external emission angle; c_0 is the speed of light; T is the temperature. The right side of the equation holds for excitation levels typical of solar illumination when Bose function can be substituted by Boltzmann distribution. For further calculation, J_{PL} can be described by EQY, for $EQY = J_{PL}/J_{ex}$. Then equation (4.3) can be written by

$$\mu = kT \ln \frac{J_{PL}}{J_{0,rad}} = kT \left[\ln \frac{J_{ex}}{J_{0,rad}} + \ln(EQY) \right] = \mu_{OC,rad} + kT \ln(EQY) \quad (4.4)$$

where $\mu_{OC,rad}$ is the maximum of the free energy when the EQY is 1, which means only radiative recombination happens under open circuit condition.

Sample	Bandgap (eV)	EQY (%)	$\mu_{oc,rad}$ (eV)	μ_{oc} (eV)
BA₂SnI₄	2.00	0.32±0.08	1.701	1.552±0.006
BA₂MASn₂I₇	1.72	0.9±0.2	1.440	1.319±0.006

Table 5. Summary of bandgap, EQY and free energy of the two samples.

If all photons with energy higher than bandgap are absorbed, the $\frac{\mu_{oc,rad}}{e}$ will be the SQ limit of open circuit voltage. The non-radiative recombinations only affect the EQY, with 10 drop the free energy will lost 60 meV under the temperature of 300K. With the previous work in our group, the $\mu_{oc,rad}$ can be given by the equation below:

$$\mu_{oc,rad} = E_{gap} \frac{T_{sun} - T}{T} + kT \ln \frac{T_{sun}}{T} + kT \ln [f(T, T_{sun}, E_{gap}) \frac{\Omega_{sun} \bar{a}_{sun}}{\Omega \bar{a}_T}] \quad (4.5)$$

In this equation, k is Boltzmann constant, T_{sun} is 5541 K, T is 300 K, $\Omega_{sun}/\Omega = 6.8 \cdot 10^{-5}/\pi$. \bar{a}_{sun} and \bar{a}_T are the spectrally averaged film absorptivity, weighted by the black-body radiation spectra at $T_{sun} = 5541$ K and $T = 300$ K, respectively. $f(T, T_{sun}, E_{gap})$ is depicted as

$$f(T, T_{sun}, E_{gap}) = \frac{2\left(\frac{kT_{sun}}{E_{gap}}\right)^2 + 2\frac{kT_{sun}}{E_{gap}} + 1}{2\left(\frac{kT}{E_{gap}}\right)^2 + 2\frac{kT}{E_{gap}} + 1} \quad (4.6)$$

Thus, with equation (4.5) and (4.6) we can calculate the $\mu_{oc,rad}$ under 1 sun irradiation which is $66 \mu\text{W cm}^{-2}$, consequently we can get the $\mu_{oc,rad}$ of the whole light intensity series. Then with equation (4.4) we can calculate the free energy after measuring the EQY of the sample. Unless EQY is unit, the free energy is equal to $\mu_{oc,rad}$, or the free energy will be less than $\mu_{oc,rad}$.

Figure 4.5 is the EQY of the samples, measured by integrating sphere method. Under

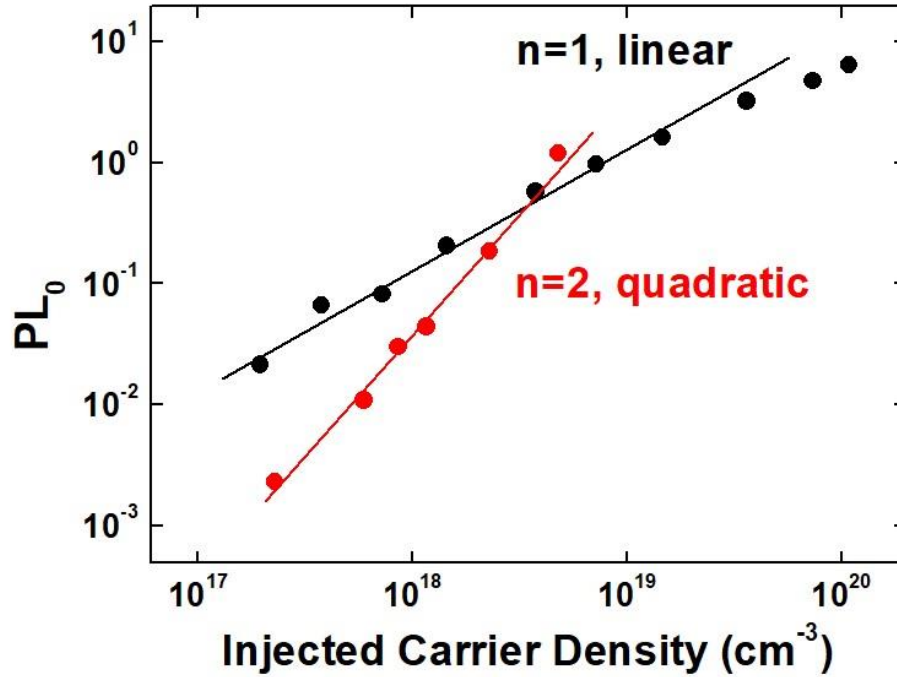


Figure 4.7. Photoluminescence intensity at decay time 0 as a function of injected carrier density

1 sun condition ($66 \mu\text{W cm}^{-2}$), the EQY of the samples are 0.32% ($n=1$) and 0.9% ($n=2$), the results of free energy are shown in **Figure 4.6**, summarized in **Table 5**.

4.2.3. Ultrafast spectroscopy measurements

Figure 4.7 shows the log-log plot of PL_0 to injected carrier density n_0 . PL_0 is the PL intensity at time 0, which means the initial intensity immediately after the laser pulse strike on the sample. This intensity is measured by TRPL measurement. The injected carriers are photo-generated carriers and the density can be given by the fluence of laser pulse Φ , excitation photon energy $h\nu_{exc}$ and absorption coefficient of the excitation light α_{exc} . The equation is $n_0 = \Phi \alpha_{exc} / h\nu_{exc}$. Φ can be given by laser power divided by frequency and spot area; $h\nu_{exc}$ is the photon energy of 400 nm which is the excitation wavelength; α_{exc} can be given by the absorbance of 400 nm light and the thickness of the sample. Thus we get the plot of PL_0 to injected carrier density. As

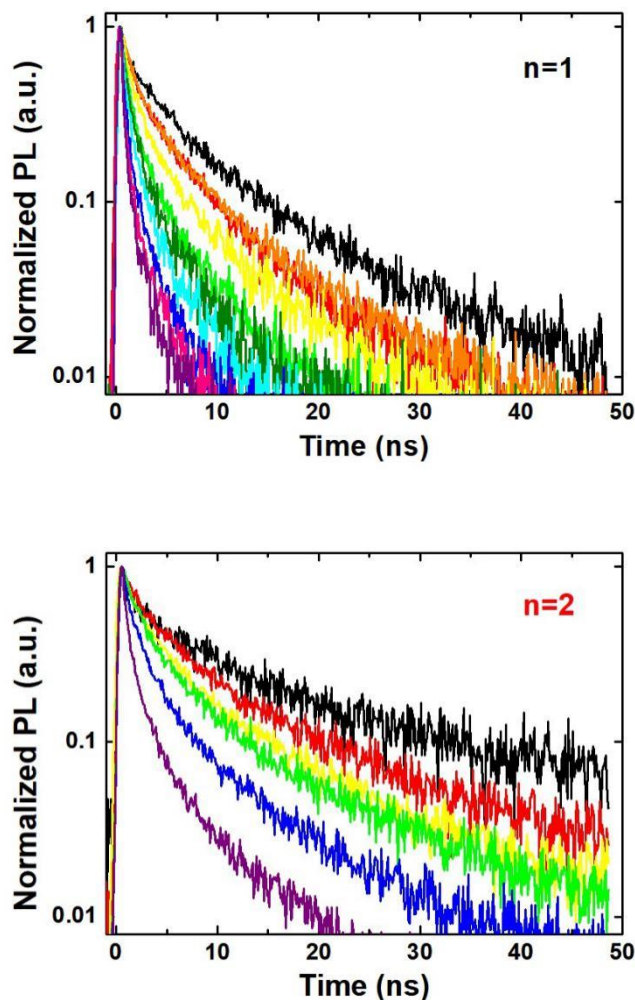


Figure 4.8. TRPL decay of different laser pulse fluence, upper is $n=1$ sample, fluence from 0.65 to $362.61 \mu\text{J cm}^{-2}$; down is $n=2$, fluence from 0.79 to $32.34 \mu\text{J cm}^{-2}$.

seen in the figure, $n=1$ sample shows linear behavior while $n=2$ sample shows quadratic behavior. The light emission of samples are due to the radiative recombination including excitonic recombination and bimolecular recombination. The recombination rate can be described as $R_{rad}=B_1n+B_2n^2$. If in the sample excitons are main charge carriers, then $R_{rad}=B_1n$ and PL_0 is proportional to n and if free carriers are main charge carriers, then $R_{rad}=B_2n^2$ and PL_0 is proportional to n^2 . Thus, according to the results we can consider in $n=1$ sample excitons are main carriers and in $n=2$ sample there are more free carriers. As can be seen in **Figure 4.8**, the decays become shorter with the increasing of laser pulse, and lifetimes extracted from the

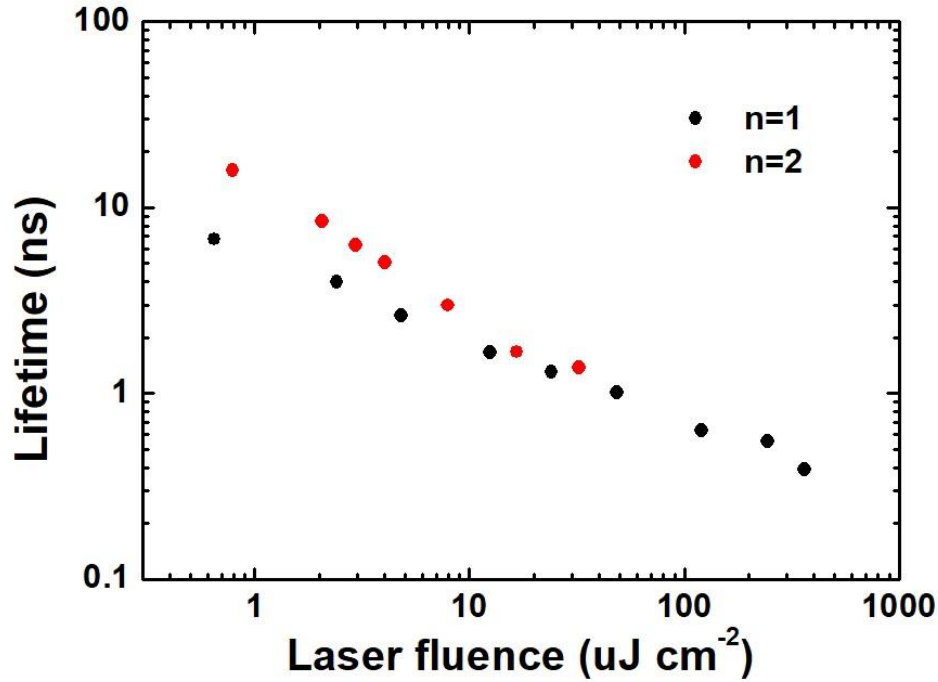


Figure 4.9. TRPL lifetime extracted from **Figure 4.8**, black dots represent $n=1$ sample, and red dots represent $n=2$ sample..

decays in **Figure 4.8** are shown in **Figure 4.9**. The lifetime of $n=2$ sample is decreasing faster than $n=1$ sample.

To further confirm the photo-generated charge carriers in the two samples, pump-probe spectroscopy was carried out. **Figure 4.10** is the plot of $\Delta T/T$ as a function of probe wavelength. For $n=1$ sample, photo-bleaching appears with two bleaching peaks at 522 nm and 603 nm. The 2 negative peaks at 560 nm and 627 nm are because of photoinduced absorption which leads to the excitation of electrons from one excited state to another. In $n=2$ sample, it is very different from $n=1$. Only one broadened positive peak at 685 nm. The result is corresponding to the TRPL measurement that is excitons in $n=1$ sample and free carrier in $n=2$ sample.

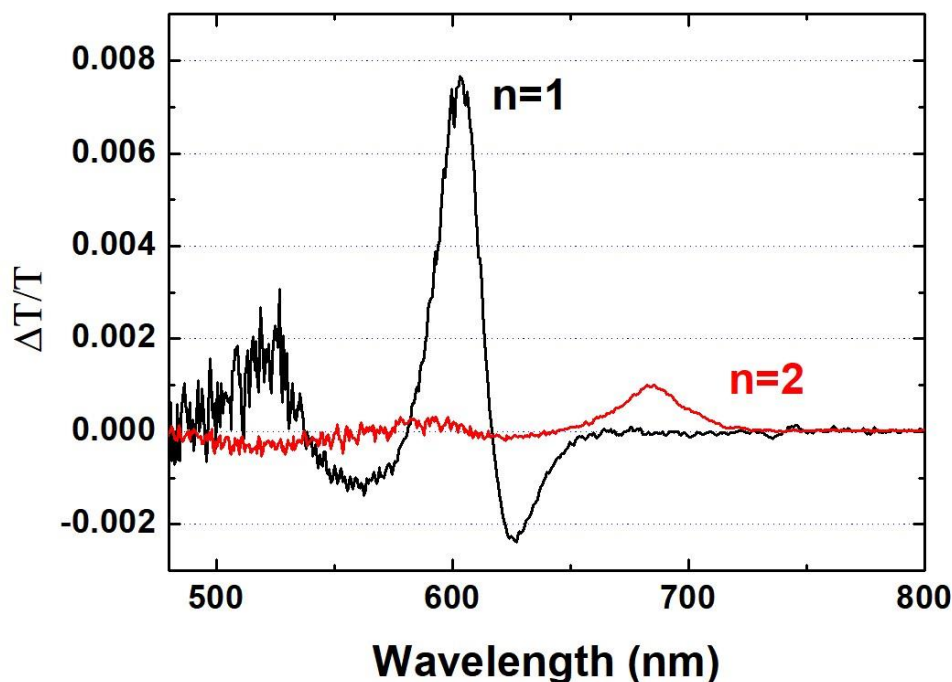


Figure 4.10. Pump-probe spectroscopy of the $n=1$ and $n=2$ samples. Differential transmission of probe pulse as a function of probe wavelength.

4.2.4. Conclusion

In this chapter, BA_2SnI_4 and $\text{BA}_2\text{MASn}_2\text{I}_7$ single phase thin films were fabricated. The absorption spectra determine the bandgaps of them are 2.00 eV and 1.72 eV, indicating higher n number of $\text{BA}_2\text{MA}_{n-1}\text{Sn}_n\text{I}_{3n+1}$ perovskite possess smaller bandgap which will be more suitable for solar cell absorber materials. Besides, TRPL and pump-probe spectroscopy measurements were proceeded to get a good understanding of the photo-generated carriers in the samples.

Further studies need to be accomplished for higher n number tin perovskite to understand the inner nature of this materials. Since the stability of tin perovskite is much worse than lead one, even 2D tin perovskite will degrade in 1h, how to solve the stability issue is another great challenge for tin perovskite solar cells.

5. Summary and outlook

Solar energy is the origin energy needed for life on earth, coming from the photosynthesis of plants. Solar cells is the most direct way to this inexhaustible energy resource. The first and second generation solar cells have been industrialized for several decades. Although the cost of these solar cells have decreased more than 90%, researchers are still contributing to new, simply operated, highly efficient solar cells. Under this circumstance, perovskite comes into everyone's view.

Perovskite have already been studied for 10 year. Too many achievement are accomplished by researchers throughout the world. Despite the more than 25% power conversion efficiency, stability is always the biggest issue as the NREL statistics denoted "not stabilized" for perovskite solar cell every year. Hence, people tried to solve or avoid this problem. 2D perovskite is one of the ideas for improving stability. However, the confinement-well structure is not preferable for charge transport unless the growth orientation can be regulated. In this thesis, we also provided a film deposition method to improve the growth orientation and phase distribution for quasi-2D perovskite. Although result shows the film is mixture of different phases, the PCE is increased beyond 14% and the film is much more stable than those 3D films when exposed to ambient environment.

Another problem is toxicity of lead, which is almost eternal harm when released to the natural environment. Then tin perovskite solar cells have sprung out with highest PCE 9% to date. 3D tin perovskite possess lower bandgap than lead one, leading to high J_{SC} but low V_{OC} . However, the photophysics of tin perovskite materials is still not very clear. Considering 2D tin perovskite should be more stable, we tried to fabricate different 2D tin perovskite thin films. The $n=1$ and $n=2$ films were successfully fabricated. Using time-resolved photoluminescence and pump-probe spectroscopy, the carrier behaviors were monitored and determined excitons for $n=1$ and free carriers for $n=2$. But the stability of 2D tin perovskite is much worse, they will degrade in 1h.

For the future, stability is still the one need to be improved especially for tin perovskite. Also, understanding the natural photophysics of tin perovskite material is another topic. After revealing the photophysics of tin perovskite, it might be possible to improve the PCE to higher level.

Supporting information to chapter 3

Device fabrication of (FAPbI₃)_{0.83}(MAPbBr₃)_{0.17} 3D perovskite

The device structure is the same with quasi-2D perovskite solar cells, and the substrates were prepared in the same way when fabricating 2D perovskite solar cells. The only difference is the perovskite deposition process.

The precursor solution is prepared by mixing stiochiometric of FAI, PbI₂, MABr, PbBr₂ that is the molar ratio of 0.83:0.83:0.17:0.17 in DMF/DMSO 4/1 mixed solvent. The concentration of Pb²⁺ is 1.3M. ITO substrates are washed by deionized water, actone and isopropanol subsequently. Then the substrates are treat by UV-ozone for 10 min followed by deposition of PEDOT:PSS or PCP-Na. Then the coated substrates are dried at 140°C for 20 min. The perovskite film was deposited using the anti-solvent technique, and spin-coated, firstly at a speed of 2000 rpm for 2s, secondly at a speed of 4000 rpm for 30s and 0.2mL chlorobenzene was added as anti-solvent at 13s. Then the thin film was annealed at 100 °C for 10 min. Then PCBM solution in chlorobenzene of 20 mg mL⁻¹ was deposited at a speed of 1000 rpm for 60 s. 20 nm of C₆₀, 6 nm BCP and 100 nm aluminum were sequentially evaporated on top of PCBM layer under vacuum degree <10⁻⁷ mbar.

Device characterization method, XRD, UV-vis absorption, SEM images and photoluminescence were all the same with 2D perovskite solar cells.

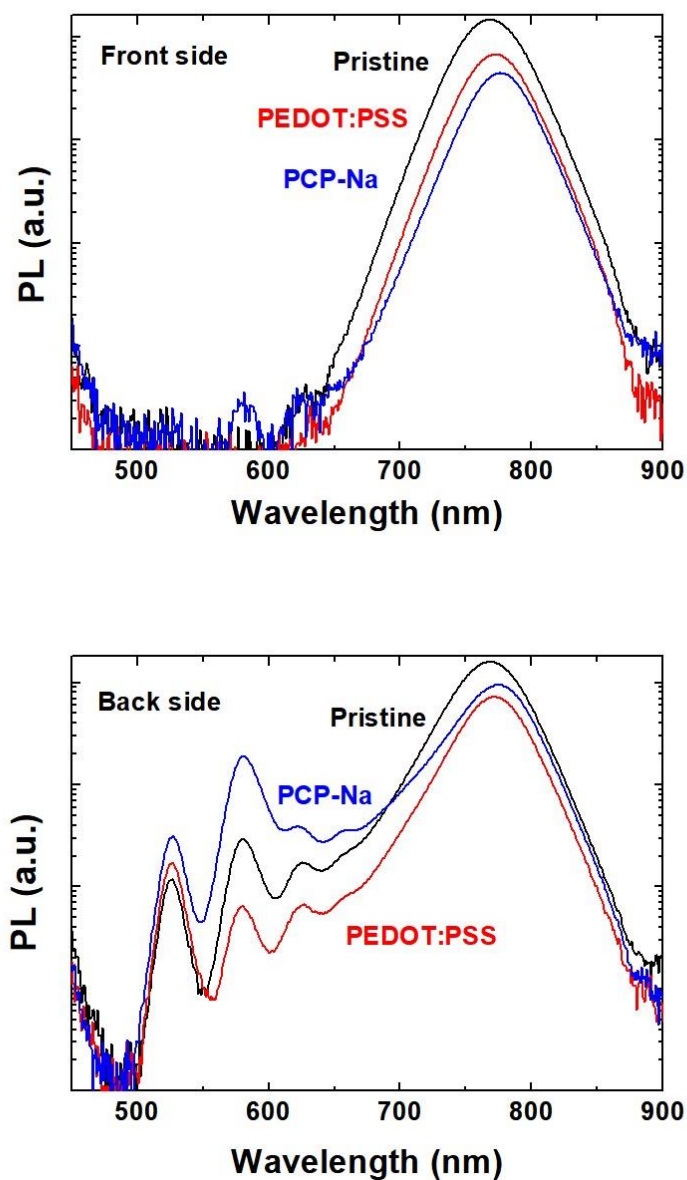


Figure A1. Semilogarithmic plots of steady state spectra of thin films grown on different substrates, glass, glass/PEDOT:PSS, glass/PCP-Na measured from perovskite side (up) and glass side (down).

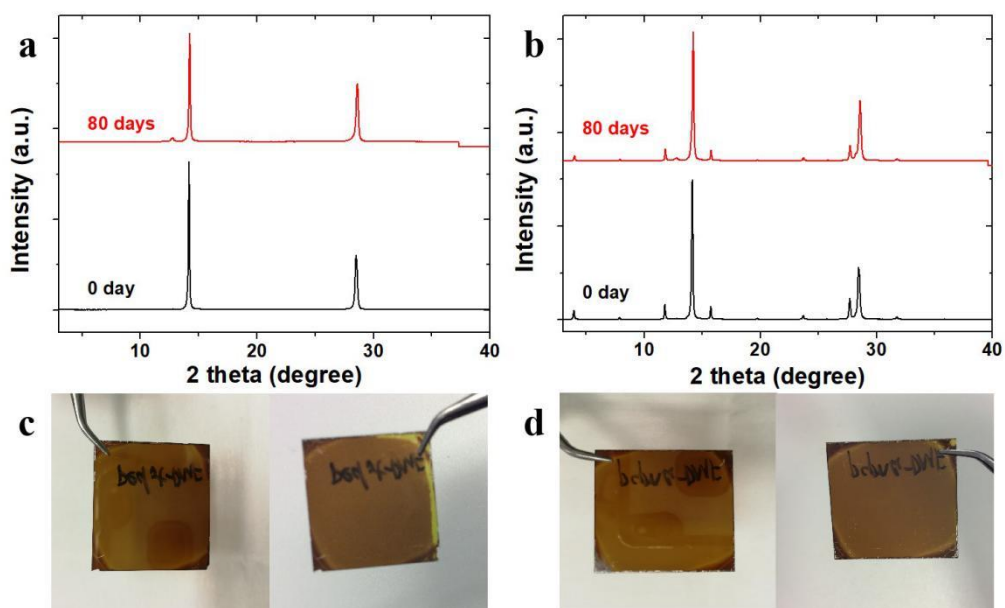


Figure A2. XRD patterns and film images on different HTL of fresh sample and 80 days in the air, (a, c) film on PEDOT: PSS, (b, d) film on PCP-Na.

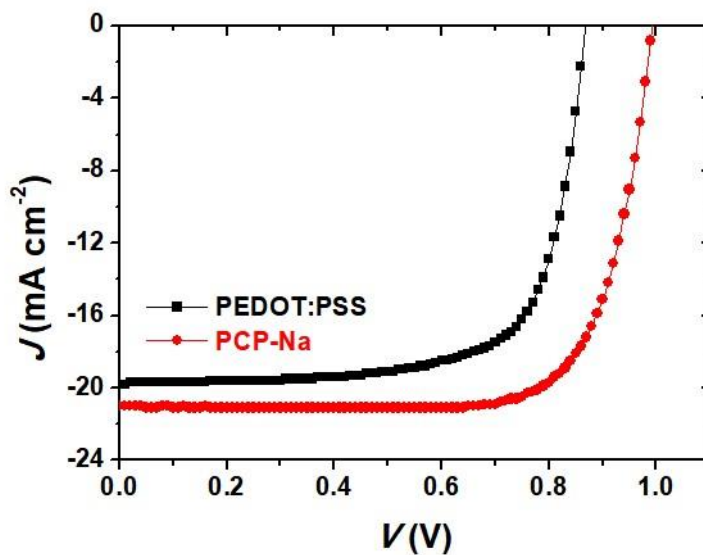


Figure A3. J - V curves of the 3D perovskite solar cells with device structure as: ITO/HTL/(FAPbI₃)_{0.83}(MAPbBr₃)_{0.17}/PC61BM/C60/BCP/Al.

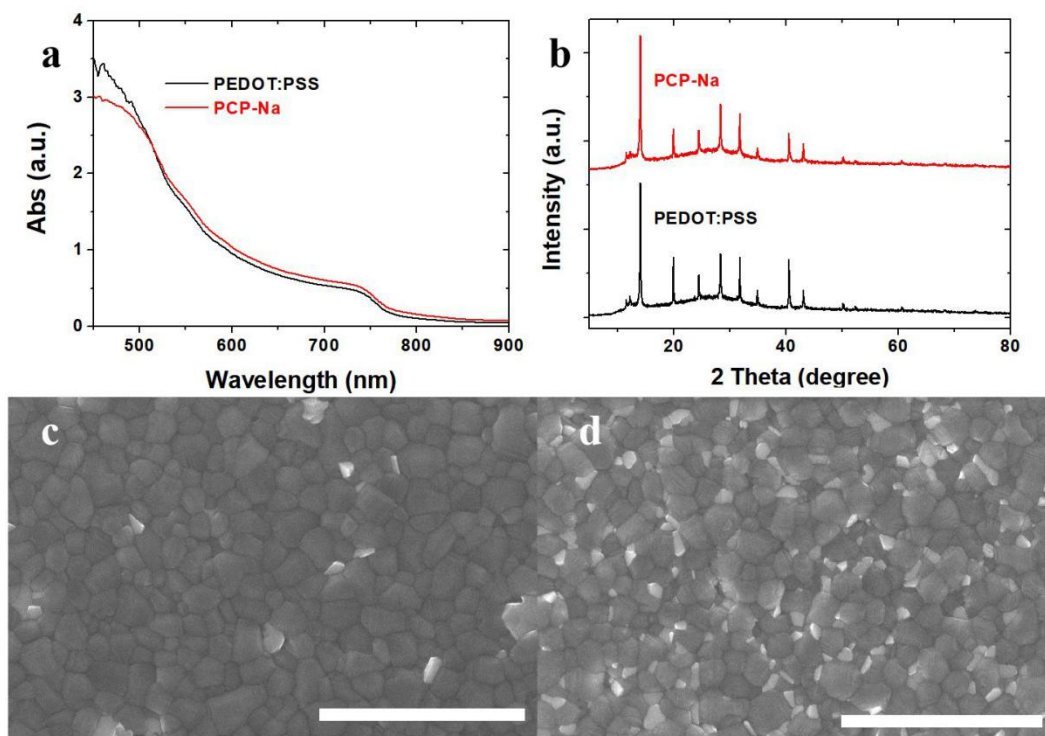


Figure A4. UV-vis absorption (a), XRD patterns (b) and SEM images (c) for PEDOT: PSS sample and (d) for PCP-Na sample. The scale-bar of SEM images is 2 μm .

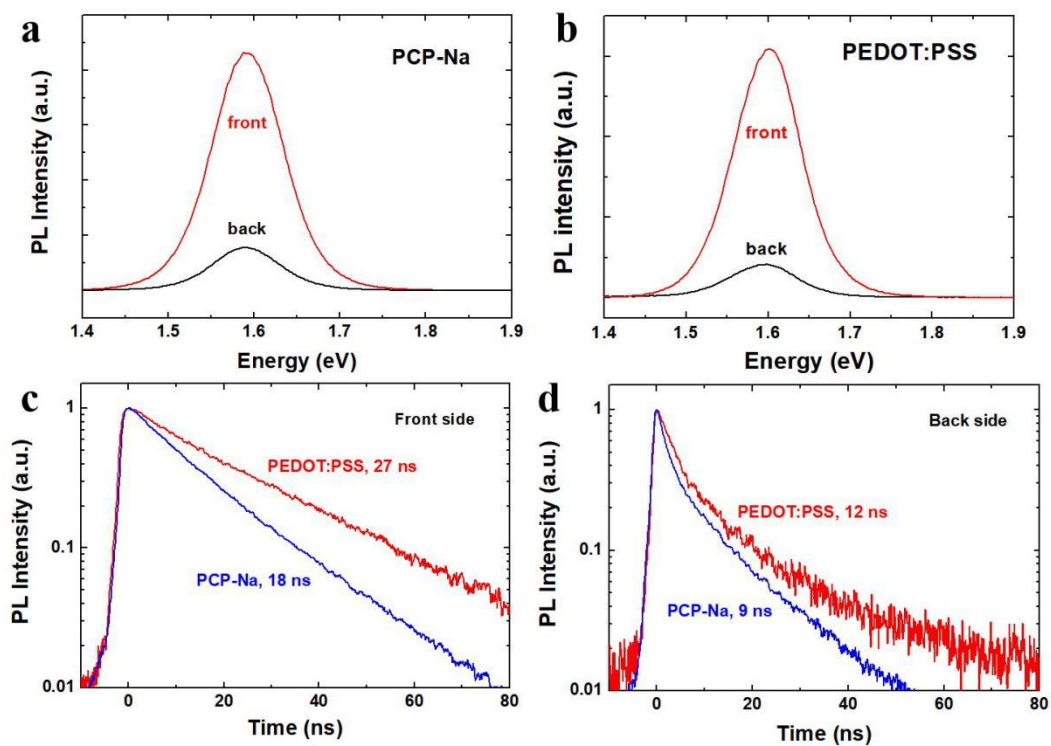
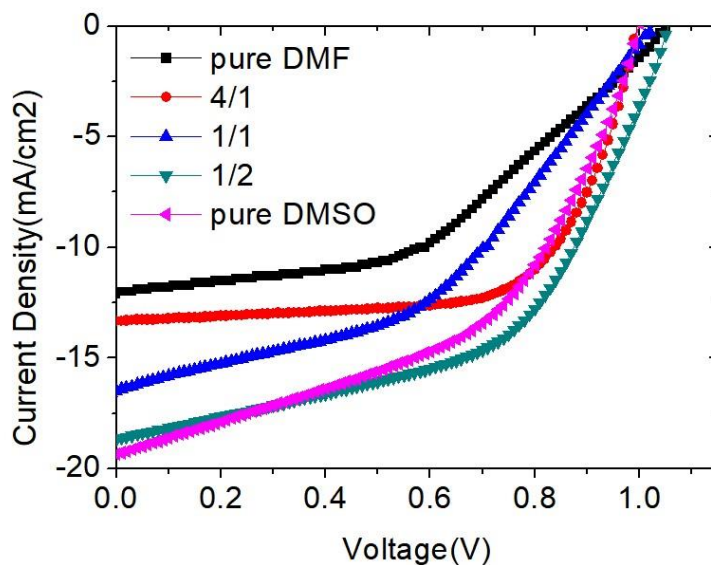


Figure A5. Steady state photoluminescence (a) and TRPL spectra for different samples (b) excited from perovskite side, (c) excited from glass side.



	Jsc(mA/cm ²)	Voc(V)	FF	PCE(%)
in DMF	12.06	1.053	0.47	5.91
4/1	13.33	0.995	0.67	8.89
1/1	16.48	1.026	0.44	7.42
1/2	18.66	1.055	0.53	10.45
DMSO	19.35	0.998	0.49	9.39

Figure A6. Modification of solvent for vacuum assisted deposition method, the DMF/DMSO 1/2 shows the best device performance. The details are in the table below.

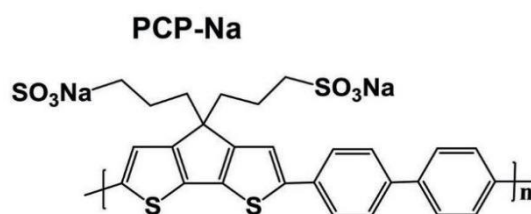


Figure A7. Molecule structure of PCP-Na

Supporting information to chapter 4

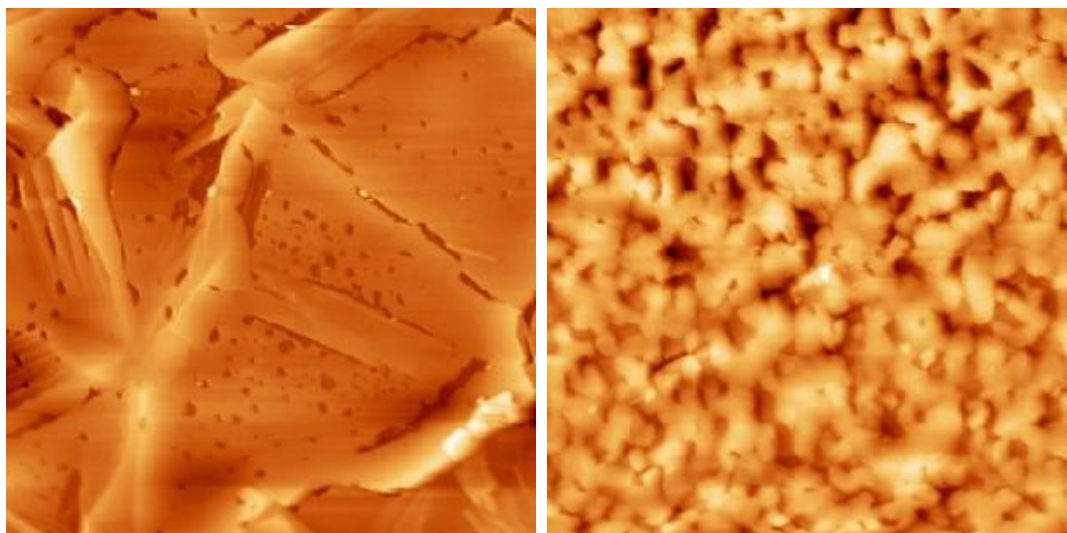


Figure B1. AFM images of $n=1$ (left) and $n=2$ (right) samples, the image size is $50 \times 50 \mu\text{m}$.

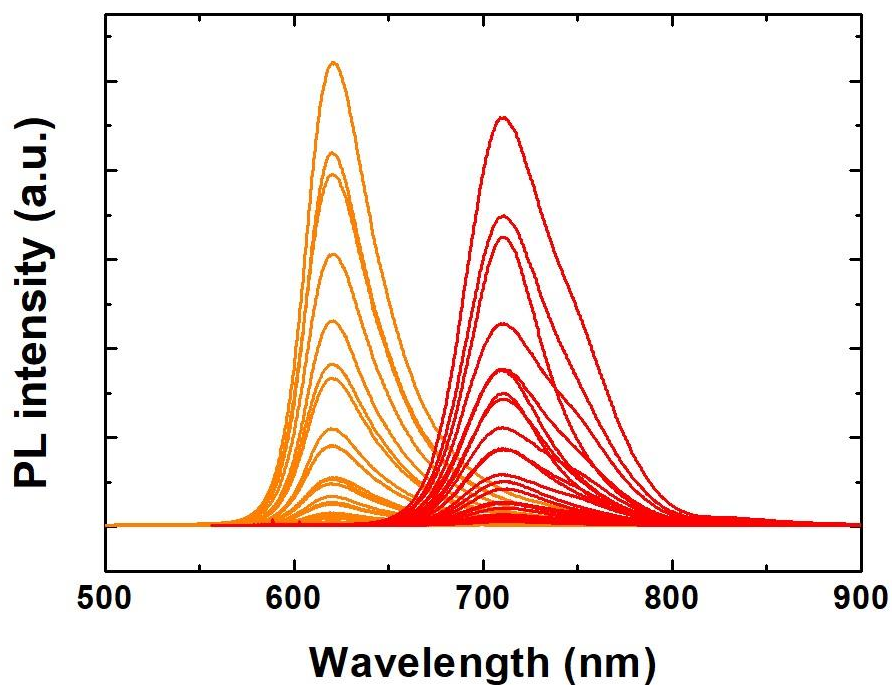


Figure B2. PL spectra of the 2 samples under excitation of continuous-wave laser (405 nm). The orange curves (610.6 nm) belong to $n=1$ sample and red curves (710.8 nm) belong to $n=2$ sample.

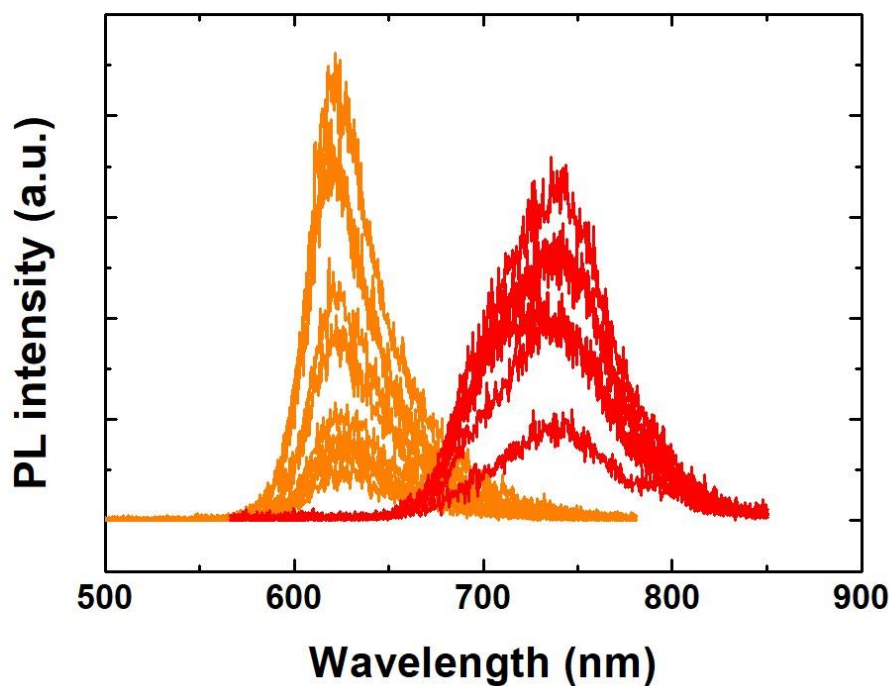


Figure B3. Steady state spectra of $n=1$ and $n=2$ samples corresponding to **Figure 4.8**, under excitation of 400 nm.

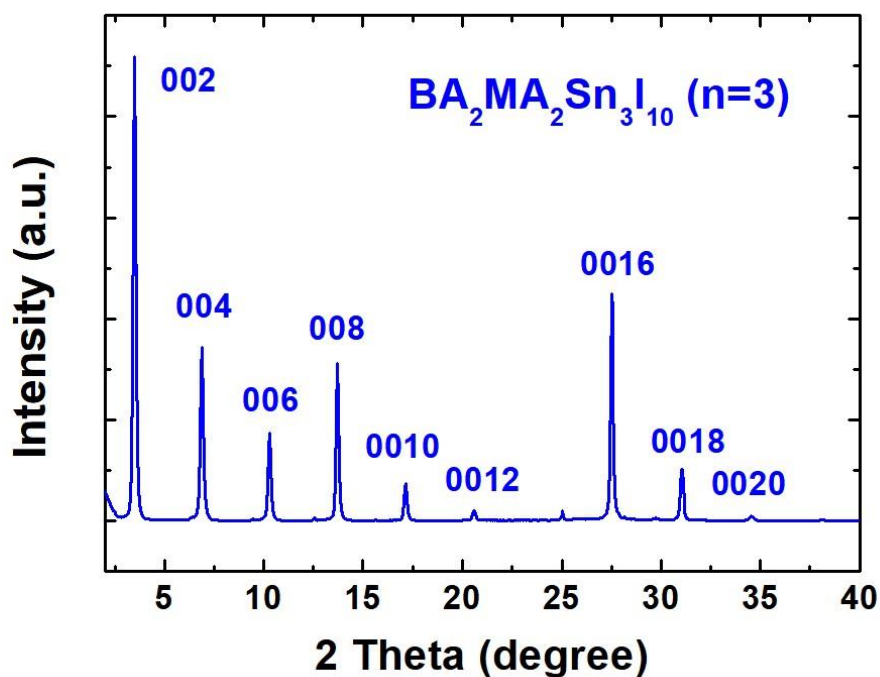


Figure B4. The XRD pattern of $n=3$ thin film that deposited by vacuum-assisted method with some modifications at last. It is very unstable so that the XRD pattern was measured for several times each time with fresh sample.

References

1. Polman, A., M. Knight, E.C. Garnett, B. Ehrler, and W.C. Sinke, *Photovoltaic materials: Present efficiencies and future challenges*. Science, 2016. **352**(6283): p. aad4424.
2. Zhou, W., Z. Wen, and P. Gao, *Less is More: Dopant-Free Hole Transporting Materials for High-Efficiency Perovskite Solar Cells*. Advanced Energy Materials, 2018.
3. Zhang, W., G.E. Eperon, and H.J. Snaith, *Metal halide perovskites for energy applications*. Nature Energy, 2016. **1**(6).
4. Yun, S., X. Zhou, J. Even, and A. Hagfeldt, *Theoretical Treatment of CH₃NH₃PbI₃ Perovskite Solar Cells*. Angew Chem Int Ed Engl, 2017. **56**(50): p. 15806-15817.
5. Kojima, A., K. Teshima, Y. Shirai, and T. Miyasaka, *Organometal Halide Perovskites as Visible-Light Sensitizers for Photovoltaic Cells*. Journal of the American Chemical Society, 2009. **131**(17): p. 6050-6051.
6. www.nrel.gov/pv/assets/pdfs/best-research-cell-efficiencies.20190802.pdf.
7. Yang, W.S., B.-W. Park, E.H. Jung, N.J. Jeon, Y.C. Kim, D.U. Lee, S.S. Shin, J. Seo, E.K. Kim, J.H. Noh, and S.I. Seok, *Iodide management in formamidinium-lead-halide-based perovskite layers for efficient solar cells*. Science, 2017. **356**: p. 1376-1379.
8. Yang, S., W. Fu, Z. Zhang, H. Chen, and C.-Z. Li, *Recent advances in perovskite solar cells: efficiency, stability and lead-free perovskite*. Journal of Materials Chemistry A, 2017. **5**(23): p. 11462-11482.

9. Xiao, J.-W., L. Liu, D. Zhang, N. De Marco, J.-W. Lee, O. Lin, Q. Chen, and Y. Yang, *The Emergence of the Mixed Perovskites and Their Applications as Solar Cells*. *Advanced Energy Materials*, 2017. **7**(20).
10. Xu, W., L. Zheng, X. Zhang, Y. Cao, T. Meng, D. Wu, L. Liu, W. Hu, and X. Gong, *Efficient Perovskite Solar Cells Fabricated by Co Partially Substituted Hybrid Perovskite*. *Advanced Energy Materials*, 2018. **0**(0): p. 1703178.
11. Pedesseau, L., D. Saporì, B. Traore, R. Robles, H.-H. Fang, M.A. Loi, H. Tsai, W. Nie, J.-C. Blancon, A. Neukirch, S. Treiak, A.D. Mohite, C. Katan, J. Even, and M. Kepenekian, *Advances and Promises of Layered Halide Hybrid Perovskite Semiconductors*. *ACS Nano*, 2016. **10**(11): p. 9776-9786.
12. Li, M., Q. Gao, P. Liu, Q. Liao, H. Zhang, J. Yao, W. Hu, Y. Wu, and H. Fu, *Amplified Spontaneous Emission Based on 2D Ruddlesden–Popper Perovskites*. *Advanced Functional Materials*, 2018. **0**(0): p. 1707006.
13. Stolterfoht, M., C.M. Wolff, Y. Amir, A. Paulke, L. Perdigón-Toro, P. Caprioglio, and D. Neher, *Approaching the fill factor Shockley–Queisser limit in stable, dopant-free triple cation perovskite solar cells*. *Energy & Environmental Science*, 2017. **10**(6): p. 1530-1539.
14. Chen, M., M.-G. Ju, A.D. Carl, Y. Zong, R.L. Grimm, J. Gu, X.C. Zeng, Y. Zhou, and N.P. Padture, *Cesium Titanium(IV) Bromide Thin Films Based Stable Lead-free Perovskite Solar Cells*. *Joule*, 2018. **2**: p. 1-13.
15. Jia, Y., R.A. Kerner, A.J. Grede, B.P. Rand, and N.C. Giebink, *Continuous-wave lasing in an organic–inorganic lead halide perovskite semiconductor*. *Nature Photonics*, 2017. **11**(12): p. 784-788.
16. Quan, L.N., Y. Zhao, F.P. Garcia de Arquer, R. Sabatini, G. Walters, O. Voznyy, R. Comin, Y. Li, J.Z. Fan, H. Tan, J. Pan, M. Yuan, O.M. Bakr, Z. Lu, D.H. Kim, and E.H. Sargent, *Tailoring the Energy Landscape in Quasi-2D Halide*

- Perovskites Enables Efficient Green-Light Emission*. Nano Lett, 2017. **17**(6): p. 3701-3709.
17. Abdi-Jalebi, M., Z. Andaji-Garmaroudi, S. Cacovich, C. Stavrakas, B. Philippe, J.M. Richter, M. Alsari, E.P. Booker, E.M. Hutter, A.J. Pearson, S. Lilliu, T.J. Savenije, H. Rensmo, G. Divitini, C. Ducati, R.H. Friend, and S.D. Stranks, *Maximizing and stabilizing luminescence from halide perovskites with potassium passivation*. Nature, 2018. **555**: p. 497.
 18. Correa-Baena, J.-P., A. Abate, M. Saliba, W. Tress, T. Jesper Jacobsson, M. Grätzel, and A. Hagfeldt, *The rapid evolution of highly efficient perovskite solar cells*. Energy & Environmental Science, 2017. **10**(3): p. 710-727.
 19. Antonietta Loi, M. and J.C. Hummelen, *Perovskites under the Sun*. Nature Materials, 2013. **12**: p. 1087.
 20. Yang, X., X. Zhang, J. Deng, Z. Chu, Q. Jiang, J. Meng, P. Wang, L. Zhang, Z. Yin, and J. You, *Efficient green light-emitting diodes based on quasi-two-dimensional composition and phase engineered perovskite with surface passivation*. Nature Communications, 2018. **9**(1): p. 570.
 21. Yang, M., Z. Li, M.O. Reese, O.G. Reid, D.H. Kim, S. Siol, T.R. Klein, Y. Yan, J.J. Berry, M.F.A.M. van Hest, and K. Zhu, *Perovskite ink with wide processing window for scalable high-efficiency solar cells*. Nature Energy, 2017. **2**: p. 17038.
 22. Yang, F., S. Cheng, X. Zhang, X. Ren, R. Li, H. Dong, and W. Hu, *2D Organic Materials for Optoelectronic Applications*. Adv Mater, 2018. **30**(2).
 23. Xu, K., C.C. Lin, X. Xie, and A. Meijerink, *Efficient and Stable Luminescence from Mn(2+) in Core and Core-Isocrystalline Shell CsPbCl₃ Perovskite Nanocrystals*. Chem Mater, 2017. **29**(10): p. 4265-4272.

24. Wei, H., Y. Fang, P. Mulligan, W. Chuirazzi, H.-H. Fang, C. Wang, B.R. Ecker, Y. Gao, M.A. Loi, L. Cao, and J. Huang, *Sensitive X-ray detectors made of methylammonium lead tribromide perovskite single crystals*. *Nature Photonics*, 2016. **10**: p. 333.
25. Smith, M.D. and H.I. Karunadasa, *White-Light Emission from Layered Halide Perovskites*. *Accounts of Chemical Research*, 2018.
26. Liu, F., Y. Zhang, C. Ding, S. Kobayashi, T. Izuishi, N. Nakazawa, T. Toyoda, T. Ohta, S. Hayase, T. Minemoto, K. Yoshino, S. Dai, and Q. Shen, *Highly Luminescent Phase-Stable CsPbI₃ Perovskite Quantum Dots Achieving Near 100% Absolute Photoluminescence Quantum Yield*. *ACS Nano*, 2017. **11**(10): p. 10373-10383.
27. Wang, S., K. Wang, Z. Gu, Y. Wang, C. Huang, N. Yi, S. Xiao, and Q. Song, *Solution-Phase Synthesis of Cesium Lead Halide Perovskite Microrods for High-Quality Microlasers and Photodetectors*. *Advanced Optical Materials*, 2017. **5**(11).
28. Saliba, M., J.P. Correa-Baena, M. Gratzel, A. Hagfeldt, and A. Abate, *Perovskite Solar Cells: From the Atomic Level to Film Quality and Device Performance*. *Angew Chem Int Ed Engl*, 2018. **57**(10): p. 2554-2569.
29. Filip, M.R. and F. Giustino, *The geometric blueprint of perovskites*. *Proceedings of the National Academy of Sciences*, 2018. **115**(21): p. 5397.
30. Bertolotti, F., L. Protesescu, M.V. Kovalenko, S. Yakunin, A. Cervellino, S.J.L. Billinge, M.W. Terban, J.S. Pedersen, N. Masciocchi, and A. Guagliardi, *Coherent Nanotwins and Dynamic Disorder in Cesium Lead Halide Perovskite Nanocrystals*. *ACS Nano*, 2017. **11**(4): p. 3819-3831.
31. Butkus, J., P. Vashishtha, K. Chen, J.K. Gallaher, S.K.K. Prasad, D.Z. Metin, G. Laufersky, N. Gaston, J.E. Halpert, and J.M. Hodgkiss, *The Evolution of*

- Quantum Confinement in CsPbBr₃ Perovskite Nanocrystals*. Chemistry of Materials, 2017. **29**(8): p. 3644-3652.
32. Saouma, F.O., D.Y. Park, S.H. Kim, M.S. Jeong, and J.I. Jang, *Multiphoton Absorption Coefficients of Organic–Inorganic Lead Halide Perovskites CH₃NH₃PbX₃ (X = Cl, Br, I) Single Crystals*. Chemistry of Materials, 2017. **29**(16): p. 6876-6882.
33. Saparov, B. and D.B. Mitzi, *Organic-Inorganic Perovskites: Structural Versatility for Functional Materials Design*. Chem Rev, 2016. **116**(7): p. 4558-96.
34. Jeon, T., S.J. Kim, J. Yoon, J. Byun, H.R. Hong, T.-W. Lee, J.-S. Kim, B. Shin, and S.O. Kim, *Hybrid Perovskites: Effective Crystal Growth for Optoelectronic Applications*. Advanced Energy Materials, 2017. **7**(19).
35. Mitzi, D.B. and K. Liang, *Preparation and Properties of (C₄H₉NH₃)₂EuI₄: A Luminescent Organic–Inorganic Perovskite with a Divalent Rare-Earth Metal Halide Framework*. Chemistry of Materials, 1997. **9**(12): p. 2990-2995.
36. Grimm, J., J.F. Suyver, E. Beurer, G. Carver, and H.U. Güdel, *Light-Emission and Excited-State Dynamics in Tm²⁺ Doped CsCaCl₃, CsCaBr₃, and CsCaI₃*. The Journal of Physical Chemistry B, 2006. **110**(5): p. 2093-2101.
37. Elliott, N. and L. Pauling, *The Crystal Structure of Cesium Aurous Auric Chloride, Cs₂AuAuCl₆, and Cesium Argentous Auric Chloride, Cs₂AgAuCl₆*. Journal of the American Chemical Society, 1938. **60**(8): p. 1846-1851.
38. Eperon, G.E., S.D. Stranks, C. Menelaou, M.B. Johnston, L.M. Herz, and H.J. Snaith, *Formamidinium lead trihalide: a broadly tunable perovskite for efficient planar heterojunction solar cells*. Energy & Environmental Science, 2014. **7**(3).

39. Kieslich, G., S. Sun, and A.K. Cheetham, *Solid-state principles applied to organic–inorganic perovskites: new tricks for an old dog*. Chemical Science, 2014. **5**(12): p. 4712-4715.
40. Huang, H., J. Raith, S.V. Kershaw, S. Kalytchuk, O. Tomanec, L. Jing, A.S. Susha, R. Zboril, and A.L. Rogach, *Growth mechanism of strongly emitting CH₃NH₃PbBr₃ perovskite nanocrystals with a tunable bandgap*. Nat Commun, 2017. **8**(1): p. 996.
41. Levchuk, I., A. Osvet, X. Tang, M. Brandl, J.D. Perea, F. Hoegl, G.J. Matt, R. Hock, M. Batentschuk, and C.J. Brabec, *Brightly Luminescent and Color-Tunable Formamidinium Lead Halide Perovskite FAPbX₃ (X = Cl, Br, I) Colloidal Nanocrystals*. Nano Lett, 2017. **17**(5): p. 2765-2770.
42. Park, Y.H., I. Jeong, S. Bae, H.J. Son, P. Lee, J. Lee, C.-H. Lee, and M.J. Ko, *Inorganic Rubidium Cation as an Enhancer for Photovoltaic Performance and Moisture Stability of HC(NH₂)₂PbI₃ Perovskite Solar Cells*. Advanced Functional Materials, 2017. **27**(16).
43. Hu, Y., E.M. Hutter, P. Rieder, I. Grill, J. Hanisch, M.F. Aygüler, A.G. Hufnagel, M. Handloser, T. Bein, A. Hartschuh, K. Tvingstedt, V. Dyakonov, A. Baumann, T.J. Savenije, M.L. Petrus, and P. Docampo, *Understanding the Role of Cesium and Rubidium Additives in Perovskite Solar Cells: Trap States, Charge Transport, and Recombination*. Advanced Energy Materials, 2018. **0**(0): p. 1703057.
44. Zu, F.-S., P. Amsalem, I. Salzmann, R.-B. Wang, M. Ralaiarisoa, S. Kowarik, S. Duhm, and N. Koch, *Impact of White Light Illumination on the Electronic and Chemical Structures of Mixed Halide and Single Crystal Perovskites*. Advanced Optical Materials, 2017. **5**(9).

45. Zhou, Y., F. Wang, H.-H. Fang, M.A. Loi, F.-Y. Xie, N. Zhao, and C.-P. Wong, *Distribution of bromine in mixed iodide-bromide organolead perovskites and its impact on photovoltaic performance*. *Journal of Materials Chemistry A*, 2016. **4**(41): p. 16191-16197.
46. Zhou, Y., F. Wang, Y. Cao, J.P. Wang, H.H. Fang, A. Loi Maria, N. Zhao, and C.P. Wong, *Benzylamine - Treated Wide - Bandgap Perovskite with High Thermal - Photostability and Photovoltaic Performance*. *Advanced Energy Materials*, 2017. **7**(22): p. 1701048.
47. Zhang, X., H. Liu, W. Wang, J. Zhang, B. Xu, K.L. Karen, Y. Zheng, S. Liu, S. Chen, K. Wang, and X.W. Sun, *Hybrid Perovskite Light-Emitting Diodes Based on Perovskite Nanocrystals with Organic-Inorganic Mixed Cations*. *Adv Mater*, 2017. **29**(18).
48. Unger, E.L., L. Kegelmann, K. Suchan, D. Sörell, L. Korte, and S. Albrecht, *Roadmap and roadblocks for the band gap tunability of metal halide perovskites*. *Journal of Materials Chemistry A*, 2017. **5**(23): p. 11401-11409.
49. Kitazawa, N., Y. Watanabe, and Y. Nakamura, *Optical properties of $CH_3NH_3PbX_3$ ($X = \text{halogen}$) and their mixed-halide crystals*. *Journal of Materials Science*, 2002. **37**(17): p. 3585-3587.
50. Noh, J.H., S.H. Im, J.H. Heo, T.N. Mandal, and S.I. Seok, *Chemical Management for Colorful, Efficient, and Stable Inorganic–Organic Hybrid Nanostructured Solar Cells*. *Nano Letters*, 2013. **13**(4): p. 1764-1769.
51. Amat, A., E. Mosconi, E. Ronca, C. Quarti, P. Umari, M.K. Nazeeruddin, M. Grätzel, and F. De Angelis, *Cation-Induced Band-Gap Tuning in Organohalide Perovskites: Interplay of Spin–Orbit Coupling and Octahedra Tilting*. *Nano Letters*, 2014. **14**(6): p. 3608-3616.

-
52. Saliba, M., T. Matsui, J.-Y. Seo, K. Domanski, J.-P. Correa-Baena, M.K. Nazeeruddin, S.M. Zakeeruddin, W. Tress, A. Abate, A. Hagfeldt, and M. Grätzel, *Cesium-containing triple cation perovskite solar cells: improved stability, reproducibility and high efficiency*. *Energy & Environmental Science*, 2016. **9**(6): p. 1989-1997.
53. Li, W., E. Ionescu, R. Riedel, and A. Gurlo, *Can we predict the formability of perovskite oxynitrides from tolerance and octahedral factors?* *Journal of Materials Chemistry A*, 2013. **1**(39): p. 12239-12245.
54. Xiao, Z., Z. Song, and Y. Yan, *From Lead Halide Perovskites to Lead-Free Metal Halide Perovskites and Perovskite Derivatives*. *Advanced Materials*, 2019. **0**(0): p. 1803792.
55. Adjokatse, S., H.-H. Fang, and M.A. Loi, *Broadly tunable metal halide perovskites for solid-state light-emission applications*. *Materials Today*, 2017. **20**(8): p. 413-424.
56. Yu, L. and A. Zunger, *Identification of Potential Photovoltaic Absorbers Based on First-Principles Spectroscopic Screening of Materials*. *Physical Review Letters*, 2012. **108**(6): p. 068701.
57. Yin, W.-J., T. Shi, and Y. Yan, *Unique Properties of Halide Perovskites as Possible Origins of the Superior Solar Cell Performance*. *Advanced Materials*, 2014. **26**(27): p. 4653-4658.
58. Yin, W.-J., J.-H. Yang, J. Kang, Y. Yan, and S.-H. Wei, *Halide perovskite materials for solar cells: a theoretical review*. *Journal of Materials Chemistry A*, 2015. **3**(17): p. 8926-8942.
59. Saba, M., M. Cadelano, D. Marongiu, F. Chen, V. Sarritzu, N. Sestu, C. Figus, M. Aresti, R. Piras, A.G. Lehmann, C. Cannas, A. Musinu, F. Quochi, A. Mura,

- and G. Bongiovanni, *Correlated electron-hole plasma in organometal perovskites*. Nat Commun, 2014. **5**: p. 5049.
60. Herz, L.M., *Charge-Carrier Dynamics in Organic-Inorganic Metal Halide Perovskites*. Annual Review of Physical Chemistry, 2016. **67**(1): p. 65-89.
61. Wright, A.D., R.L. Milot, G.E. Eperon, H.J. Snaith, M.B. Johnston, and L.M. Herz, *Band-Tail Recombination in Hybrid Lead Iodide Perovskite*. Advanced Functional Materials, 2017. **27**(29).
62. Johnston, M.B. and L.M. Herz, *Hybrid Perovskites for Photovoltaics: Charge-Carrier Recombination, Diffusion, and Radiative Efficiencies*. Acc Chem Res, 2016. **49**(1): p. 146-54.
63. Sarritzu, V., N. Sestu, D. Marongiu, X. Chang, Q. Wang, M.A. Loi, F. Quochi, M. Saba, A. Mura, and G. Bongiovanni, *Perovskite Excitonics: Primary Exciton Creation and Crossover from Free Carriers to a Secondary Exciton Phase*. Advanced Optical Materials, 2018. **6**(3).
64. Manser, J.S. and P.V. Kamat, *Band filling with free charge carriers in organometal halide perovskites*. Nature Photonics, 2014. **8**: p. 737.
65. Stranks, S.D., V.M. Burlakov, T. Leijtens, J.M. Ball, A. Goriely, and H.J. Snaith, *Recombination Kinetics in Organic-Inorganic Perovskites: Excitons, Free Charge, and Subgap States*. Physical Review Applied, 2014. **2**(3): p. 034007.
66. Wehrenfennig, C., M. Liu, H.J. Snaith, M.B. Johnston, and L.M. Herz, *Charge-carrier dynamics in vapour-deposited films of the organolead halide perovskite $CH_3NH_3PbI_{3-x}Cl_x$* . Energy & Environmental Science, 2014. **7**(7): p. 2269-2275.

67. Herz, L.M., *Charge-Carrier Mobilities in Metal Halide Perovskites: Fundamental Mechanisms and Limits*. ACS Energy Letters, 2017. **2**(7): p. 1539-1548.
68. deQuilettes, D.W., S. Koch, S. Burke, R.K. Paranj, A.J. Shropshire, M.E. Ziffer, and D.S. Ginger, *Photoluminescence Lifetimes Exceeding 8 μ s and Quantum Yields Exceeding 30% in Hybrid Perovskite Thin Films by Ligand Passivation*. ACS Energy Letters, 2016. **1**(2): p. 438-444.
69. Huang, J., Y. Yuan, Y. Shao, and Y. Yan, *Understanding the physical properties of hybrid perovskites for photovoltaic applications*. Nature Reviews Materials, 2017. **2**: p. 17042.
70. Im, J.-H., C.-R. Lee, J.-W. Lee, S.-W. Park, and N.-G. Park, *6.5% efficient perovskite quantum-dot-sensitized solar cell*. Nanoscale, 2011. **3**(10): p. 4088-4093.
71. Kim, H.-S., C.-R. Lee, J.-H. Im, K.-B. Lee, T. Moehl, A. Marchioro, S.-J. Moon, R. Humphry-Baker, J.-H. Yum, J.E. Moser, M. Grätzel, and N.-G. Park, *Lead Iodide Perovskite Sensitized All-Solid-State Submicron Thin Film Mesoscopic Solar Cell with Efficiency Exceeding 9%*. Scientific Reports, 2012. **2**: p. 591.
72. Lee, M.M., J. Teuscher, T. Miyasaka, T.N. Murakami, and H.J. Snaith, *Efficient Hybrid Solar Cells Based on Meso-Superstructured Organometal Halide Perovskites*. Science, 2012. **338**(6107): p. 643.
73. Liu, M., M.B. Johnston, and H.J. Snaith, *Efficient planar heterojunction perovskite solar cells by vapour deposition*. Nature, 2013. **501**: p. 395.
74. Cao, J., H. Yu, S. Zhou, M. Qin, T.-K. Lau, X. Lu, N. Zhao, and C.-P. Wong, *Low-temperature solution-processed NiOx films for air-stable perovskite solar cells*. Journal of Materials Chemistry A, 2017. **5**(22): p. 11071-11077.

75. Lamberti, F., L. Litti, M. De Bastiani, R. Sorrentino, M. Gandini, M. Meneghetti, and A. Petrozza, *High-Quality, Ligands-Free, Mixed-Halide Perovskite Nanocrystals Inks for Optoelectronic Applications*. *Advanced Energy Materials*, 2017. **7**(8).
76. Park, S.J., S. Jeon, I.K. Lee, J. Zhang, H. Jeong, J.-Y. Park, J. Bang, T.K. Ahn, H.-W. Shin, B.-G. Kim, and H.J. Park, *Inverted planar perovskite solar cells with dopant free hole transporting material: Lewis base-assisted passivation and reduced charge recombination*. *Journal of Materials Chemistry A*, 2017. **5**(25): p. 13220-13227.
77. Xue, Q., Y. Bai, M. Liu, R. Xia, Z. Hu, Z. Chen, X.-F. Jiang, F. Huang, S. Yang, Y. Matsuo, H.-L. Yip, and Y. Cao, *Dual Interfacial Modifications Enable High Performance Semitransparent Perovskite Solar Cells with Large Open Circuit Voltage and Fill Factor*. *Advanced Energy Materials*, 2017. **7**(9).
78. Becker, M.A., R. Vaxenburg, G. Nedelcu, P.C. Sercel, A. Shabaev, M.J. Mehl, J.G. Michopoulos, S.G. Lambrakos, N. Bernstein, J.L. Lyons, T. Stoferle, R.F. Mahrt, M.V. Kovalenko, D.J. Norris, G. Raino, and A.L. Efros, *Bright triplet excitons in caesium lead halide perovskites*. *Nature*, 2018. **553**(7687): p. 189-193.
79. Jaysankar, M., M. Filipic, B. Zielinski, R. Schmager, W. Song, W. Qiu, U.W. Paetzold, T. Aernouts, M. Debucquoy, R. Gehlhaar, and J. Poortmans, *Perovskite-silicon tandem solar modules with optimised light harvesting*. *Energy & Environmental Science*, 2018.
80. Jeon, N.J., J.H. Noh, Y.C. Kim, W.S. Yang, S. Ryu, and S.I. Seok, *Solvent engineering for high-performance inorganic–organic hybrid perovskite solar cells*. *Nature Materials*, 2014. **13**: p. 897.

81. Zhou, H., Q. Chen, G. Li, S. Luo, T.-b. Song, H.-S. Duan, Z. Hong, J. You, Y. Liu, and Y. Yang, *Interface engineering of highly efficient perovskite solar cells*. Science, 2014. **345**(6196): p. 542.
82. Jiang, Q., Y. Zhao, X. Zhang, X. Yang, Y. Chen, Z. Chu, Q. Ye, X. Li, Z. Yin, and J. You, *Surface passivation of perovskite film for efficient solar cells*. Nature Photonics, 2019. **13**(7): p. 460-466.
83. Li, D., J. Shi, Y. Xu, Y. Luo, H. Wu, and Q. Meng, *Inorganic–organic halide perovskites for new photovoltaic technology*. National Science Review, 2017.
84. Correa-Baena, J.-P., M. Saliba, T. Buonassisi, M. Grätzel, A. Abate, W. Tress, and A. Hagfeldt, *Promises and challenges of perovskite solar cells*. Science, 2017. **358**(6364): p. 739.
85. Park, N.-G., M. Grätzel, T. Miyasaka, K. Zhu, and K. Emery, *Towards stable and commercially available perovskite solar cells*. Nature Energy, 2016. **1**(11).
86. Leguy, A.M.A., Y. Hu, M. Campoy-Quiles, M.I. Alonso, O.J. Weber, P. Azarhoosh, M. van Schilfgaarde, M.T. Weller, T. Bein, J. Nelson, P. Docampo, and P.R.F. Barnes, *Reversible Hydration of CH₃NH₃PbI₃ in Films, Single Crystals, and Solar Cells*. Chemistry of Materials, 2015. **27**(9): p. 3397-3407.
87. Yusoff, A.R.b.M. and M.K. Nazeeruddin, *Low-Dimensional Perovskites: From Synthesis to Stability in Perovskite Solar Cells*. Advanced Energy Materials, 2017.
88. Kim, H.S., J.Y. Seo, and N.G. Park, *Material and Device Stability in Perovskite Solar Cells*. ChemSusChem, 2016. **9**(18): p. 2528-2540.
89. Wang, K., Z. Liang, X. Wang, and X. Cui, *Lead Replacement in CH₃NH₃PbI₃ Perovskites*. Advanced Electronic Materials, 2015. **1**(10): p. 1500089.

90. Tremblay, M.-H., F. Thouin, J. Leisen, J. Bacsa, A.R. Srimath Kandada, J.M. Hoffman, M.G. Kanatzidis, A.D. Mohite, C. Silva, S. Barlow, and S.R. Marder, *(4NPEA)2PbI4 (4NPEA = 4-Nitrophenylethylammonium): Structural, NMR, and Optical Properties of a 3×3 Corrugated 2D Hybrid Perovskite*. Journal of the American Chemical Society, 2019. **141**(11): p. 4521-4525.
91. Huo, C., B. Cai, Z. Yuan, B. Ma, and H. Zeng, *Two-Dimensional Metal Halide Perovskites: Theory, Synthesis, and Optoelectronics*. Small Methods, 2017. **1**(3).
92. Fu, W., J. Wang, L. Zuo, K. Gao, F. Liu, D.S. Ginger, and A.K.Y. Jen, *Two-Dimensional Perovskite Solar Cells with 14.1% Power Conversion Efficiency and 0.68% External Radiative Efficiency*. ACS Energy Letters, 2018. **3**(9): p. 2086-2093.
93. Chen, S. and G. Shi, *Two-Dimensional Materials for Halide Perovskite-Based Optoelectronic Devices*. Adv Mater, 2017. **29**(24).
94. Milot, R.L., R.J. Sutton, G.E. Eperon, A.A. Haghghirad, J. Martinez Hardigree, L. Miranda, H.J. Snaith, M.B. Johnston, and L.M. Herz, *Charge-Carrier Dynamics in 2D Hybrid Metal-Halide Perovskites*. Nano Lett, 2016. **16**(11): p. 7001-7007.
95. Saidaminov, M.I., O.F. Mohammed, and O.M. Bakr, *Low-Dimensional-Networked Metal Halide Perovskites: The Next Big Thing*. ACS Energy Letters, 2017. **2**(4): p. 889-896.
96. Hong, X., T. Ishihara, and A.V. Nurmikko, *Dielectric confinement effect on excitons in PbI_4 -based layered semiconductors*. Physical Review B, 1992. **45**(12): p. 6961-6964.
97. Stoumpos, C.C., D.H. Cao, D.J. Clark, J. Young, J.M. Rondinelli, J.I. Jang, J.T. Hupp, and M.G. Kanatzidis, *Ruddlesden – Popper Hybrid Lead Iodide*

- Perovskite 2D Homologous Semiconductors*. Chemistry of Materials, 2016. **28**(8): p. 2852-2867.
98. Chen, Y., Y. Sun, J. Peng, J. Tang, K. Zheng, and Z. Liang, *2D Ruddlesden-Popper Perovskites for Optoelectronics*. Adv Mater, 2018. **30**(2).
99. Wang, Z., Q. Lin, F.P. Chmiel, N. Sakai, L.M. Herz, and H.J. Snaith, *Efficient ambient-air-stable solar cells with 2D–3D heterostructured butylammonium-caesium-formamidinium lead halide perovskites*. Nature Energy, 2017. **2**: p. 17135.
100. Cao, D.H., C.C. Stoumpos, O.K. Farha, J.T. Hupp, and M.G. Kanatzidis, *2D Homologous Perovskites as Light-Absorbing Materials for Solar Cell Applications*. J Am Chem Soc, 2015. **137**(24): p. 7843-50.
101. Krishna, A., S. Gottis, M.K. Nazeeruddin, and F. Sauvage, *Mixed Dimensional 2D/3D Hybrid Perovskite Absorbers: The Future of Perovskite Solar Cells?* Advanced Functional Materials, 2019. **29**(8): p. 1806482.
102. Smith, I.C., E.T. Hoke, D. Solis-Ibarra, M.D. McGehee, and H.I. Karunadasa, *A Layered Hybrid Perovskite Solar-Cell Absorber with Enhanced Moisture Stability*. Angewandte Chemie, 2014. **126**(42): p. 11414-11417.
103. Tsai, H., W. Nie, J.C. Blancon, C.C. Stoumpos, R. Asadpour, B. Harutyunyan, A.J. Neukirch, R. Verduzco, J.J. Crochet, S. Tretiak, L. Pedesseau, J. Even, M.A. Alam, G. Gupta, J. Lou, P.M. Ajayan, M.J. Bedzyk, and M.G. Kanatzidis, *High-efficiency two-dimensional Ruddlesden-Popper perovskite solar cells*. Nature, 2016. **536**(7616): p. 312-6.
104. Zhang, X., X. Ren, B. Liu, R. Munir, X. Zhu, D. Yang, J. Li, Y. Liu, D.-M. Smilgies, R. Li, Z. Yang, T. Niu, X. Wang, A. Amassian, K. Zhao, and S. Liu, *Stable high efficiency two-dimensional perovskite solar cells via cesium doping*. Energy & Environmental Science, 2017. **10**(10): p. 2095-2102.

105. Liao, Y., H. Liu, W. Zhou, D. Yang, Y. Shang, Z. Shi, B. Li, X. Jiang, L. Zhang, L.N. Quan, R. Quintero-Bermudez, B.R. Sutherland, Q. Mi, E.H. Sargent, and Z. Ning, *Highly Oriented Low-Dimensional Tin Halide Perovskites with Enhanced Stability and Photovoltaic Performance*. *J Am Chem Soc*, 2017. **139**(19): p. 6693-6699.
106. Zhang, X., G. Wu, S. Yang, W. Fu, Z. Zhang, C. Chen, W. Liu, J. Yan, W. Yang, and H. Chen, *Vertically Oriented 2D Layered Perovskite Solar Cells with Enhanced Efficiency and Good Stability*. *Small*, 2017. **13**(33).
107. Zhang, X., G. Wu, W. Fu, M. Qin, W. Yang, J. Yan, Z. Zhang, X. Lu, and H. Chen, *Orientation Regulation of Phenylethylammonium Cation Based 2D Perovskite Solar Cell with Efficiency Higher Than 11%*. *Advanced Energy Materials*, 2018. **8**(14): p. 1702498.
108. Zimmermann, I., S. Aghazada, and M.K. Nazeeruddin, *Lead and HTM Free Stable Two-Dimensional Tin Perovskites with Suitable Band Gap for Solar Cell Applications*. *Angewandte Chemie International Edition*, 2019. **58**(4): p. 1072-1076.
109. Qiu, J., Y. Xia, Y. Zheng, W. Hui, H. Gu, W. Yuan, H. Yu, L. Chao, T. Niu, Y. Yang, X. Gao, Y. Chen, and W. Huang, *2D Intermediate Suppression for Efficient Ruddlesden–Popper (RP) Phase Lead-Free Perovskite Solar Cells*. *ACS Energy Letters*, 2019: p. 1513-1520.
110. Shi, Z., J. Guo, Y. Chen, Q. Li, Y. Pan, H. Zhang, Y. Xia, and W. Huang, *Lead-Free Organic-Inorganic Hybrid Perovskites for Photovoltaic Applications: Recent Advances and Perspectives*. *Adv Mater*, 2017. **29**(16).
111. Dou, Y., L. Zhang, X. Xu, Z. Sun, T. Liao, and S.X. Dou, *Atomically thin non-layered nanomaterials for energy storage and conversion*. *Chem Soc Rev*, 2017. **46**(23): p. 7338-7373.

-
112. Konstantakou, M. and T. Stergiopoulos, *A critical review on tin halide perovskite solar cells*. Journal of Materials Chemistry A, 2017. **5**(23): p. 11518-11549.
113. Ke, W., C.C. Stoumpos, and M.G. Kanatzidis, “*Unleaded*” *Perovskites: Status Quo and Future Prospects of Tin-Based Perovskite Solar Cells*. Advanced Materials, 2018. **0**(0): p. 1803230.
114. Noel, N.K., S.D. Stranks, A. Abate, C. Wehrenfennig, S. Guarnera, A.-A. Haghighirad, A. Sadhanala, G.E. Eperon, S.K. Pathak, M.B. Johnston, A. Petrozza, L.M. Herz, and H.J. Snaith, *Lead-free organic–inorganic tin halide perovskites for photovoltaic applications*. Energy & Environmental Science, 2014. **7**(9): p. 3061-3068.
115. Hao, F., C.C. Stoumpos, D.H. Cao, R.P.H. Chang, and M.G. Kanatzidis, *Lead-free solid-state organic–inorganic halide perovskite solar cells*. Nature Photonics, 2014. **8**: p. 489.
116. Shao, S., J. Liu, G. Portale, H.H. Fang, R. Blake Graeme, H. ten Brink Gert, L.J.A. Koster, and A. Loi Maria, *Highly Reproducible Sn - Based Hybrid Perovskite Solar Cells with 9% Efficiency*. Advanced Energy Materials, 2017. **8**(4): p. 1702019.
117. Stoumpos, C.C., L. Frazer, D.J. Clark, Y.S. Kim, S.H. Rhim, A.J. Freeman, J.B. Ketterson, J.I. Jang, and M.G. Kanatzidis, *Hybrid Germanium Iodide Perovskite Semiconductors: Active Lone Pairs, Structural Distortions, Direct and Indirect Energy Gaps, and Strong Nonlinear Optical Properties*. Journal of the American Chemical Society, 2015. **137**(21): p. 6804-6819.
118. Ju, M.G., J. Dai, L. Ma, and X.C. Zeng, *Lead-Free Mixed Tin and Germanium Perovskites for Photovoltaic Application*. J Am Chem Soc, 2017. **139**(23): p. 8038-8043.

119. Krishnamoorthy, T., H. Ding, C. Yan, W.L. Leong, T. Baikie, Z. Zhang, M. Sherburne, S. Li, M. Asta, N. Mathews, and S.G. Mhaisalkar, *Lead-free germanium iodide perovskite materials for photovoltaic applications*. Journal of Materials Chemistry A, 2015. **3**(47): p. 23829-23832.
120. Kopacic, I., B. Friesenbichler, S.F. Hoefler, B. Kunert, H. Plank, T. Rath, and G. Trimmel, *Enhanced Performance of Germanium Halide Perovskite Solar Cells through Compositional Engineering*. ACS Applied Energy Materials, 2018. **1**(2): p. 343-347.
121. Slavney, A.H., T. Hu, A.M. Lindenberg, and H.I. Karunadasa, *A Bismuth-Halide Double Perovskite with Long Carrier Recombination Lifetime for Photovoltaic Applications*. Journal of the American Chemical Society, 2016. **138**(7): p. 2138-2141.
122. Zhang, P., J. Yang, and S.-H. Wei, *Manipulation of cation combinations and configurations of halide double perovskites for solar cell absorbers*. Journal of Materials Chemistry A, 2018. **6**(4): p. 1809-1815.
123. Zhao, X.G., D. Yang, Y. Sun, T. Li, L. Zhang, L. Yu, and A. Zunger, *Cu-In Halide Perovskite Solar Absorbers*. J Am Chem Soc, 2017. **139**(19): p. 6718-6725.
124. McClure, E.T., M.R. Ball, W. Windl, and P.M. Woodward, *Cs₂AgBiX₆ (X = Br, Cl): New Visible Light Absorbing, Lead-Free Halide Perovskite Semiconductors*. Chemistry of Materials, 2016. **28**(5): p. 1348-1354.
125. Volonakis, G., A.A. Haghghirad, R.L. Milot, W.H. Sio, M.R. Filip, B. Wenger, M.B. Johnston, L.M. Herz, H.J. Snaith, and F. Giustino, *Cs₂InAgCl₆: A New Lead-Free Halide Double Perovskite with Direct Band Gap*. The Journal of Physical Chemistry Letters, 2017. **8**(4): p. 772-778.

126. Brenes, R., D. Guo, A. Osherov, N.K. Noel, C. Eames, E.M. Hutter, S.K. Pathak, F. Niroui, R.H. Friend, M.S. Islam, H.J. Snaith, V. Bulović, T.J. Savenije, and S.D. Stranks, *Metal Halide Perovskite Polycrystalline Films Exhibiting Properties of Single Crystals*. Joule, 2017. **1**(1): p. 155-167.
127. Yang, B., C.C. Brown, J. Huang, L. Collins, X. Sang, R.R. Unocic, S. Jesse, S.V. Kalinin, A. Belianinov, J. Jakowski, D.B. Geohegan, B.G. Sumpter, K. Xiao, and O.S. Ovchinnikova, *Enhancing Ion Migration in Grain Boundaries of Hybrid Organic-Inorganic Perovskites by Chlorine*. Advanced Functional Materials, 2017. **27**(26).
128. Zhou, Y., O.S. Game, S. Pang, and N.P. Padture, *Microstructures of Organometal Trihalide Perovskites for Solar Cells: Their Evolution from Solutions and Characterization*. The Journal of Physical Chemistry Letters, 2015. **6**(23): p. 4827-4839.
129. Im, J.-H., H.-S. Kim, and N.-G. Park, *Morphology-photovoltaic property correlation in perovskite solar cells: One-step versus two-step deposition of CH₃NH₃PbI₃*. APL Materials, 2014. **2**(8): p. 081510.
130. Song, Z., S.C. Watthage, A.B. Phillips, B.L. Tompkins, R.J. Ellingson, and M.J. Heben, *Impact of Processing Temperature and Composition on the Formation of Methylammonium Lead Iodide Perovskites*. Chemistry of Materials, 2015. **27**(13): p. 4612-4619.
131. Jung, H.S. and N.-G. Park, *Perovskite Solar Cells: From Materials to Devices*. Small, 2015. **11**(1): p. 10-25.
132. Eperon, G.E., V.M. Burlakov, P. Docampo, A. Goriely, and H.J. Snaith, *Morphological Control for High Performance, Solution-Processed Planar Heterojunction Perovskite Solar Cells*. Advanced Functional Materials, 2014. **24**(1): p. 151-157.

133. Wang, Q., Y. Shao, Q. Dong, Z. Xiao, Y. Yuan, and J. Huang, *Large fill-factor bilayer iodine perovskite solar cells fabricated by a low-temperature solution-process*. *Energy & Environmental Science*, 2014. **7**(7): p. 2359-2365.
134. Saliba, M., J.-P. Correa-Baena, C.M. Wolff, M. Stolterfoht, N. Phung, S. Albrecht, D. Neher, and A. Abate, *How to Make over 20% Efficient Perovskite Solar Cells in Regular (n-i-p) and Inverted (p-i-n) Architectures*. *Chemistry of Materials*, 2018. **30**(13): p. 4193-4201.
135. Fei, C., B. Li, R. Zhang, H. Fu, J. Tian, and G. Cao, *Highly Efficient and Stable Perovskite Solar Cells Based on Monolithically Grained CH₃NH₃PbI₃ Film*. *Advanced Energy Materials*, 2017. **7**(9).
136. Zhang, M., Z. Wang, B. Zhou, X. Jia, Q. Ma, N. Yuan, X. Zheng, J. Ding, and W.-H. Zhang, *Green Anti-Solvent Processed Planar Perovskite Solar Cells with Efficiency Beyond 19%*. *Solar RRL*, 2018. **2**(2).
137. Yang, Y., S. Feng, M. Li, F. Li, C. Zhang, Y. Han, L. Li, J. Yuan, L. Cao, Z. Wang, B. Sun, and X. Gao, *Enormously improved CH₃NH₃PbI₃ film surface for environmentally stable planar perovskite solar cells with PCE exceeding 19.9%*. *Nano Energy*, 2018. **48**: p. 10-19.
138. Chen, Q., H. Zhou, Z. Hong, S. Luo, H.-S. Duan, H.-H. Wang, Y. Liu, G. Li, and Y. Yang, *Planar Heterojunction Perovskite Solar Cells via Vapor-Assisted Solution Process*. *Journal of the American Chemical Society*, 2014. **136**(2): p. 622-625.
139. Warren, B.E., *X-ray Diffraction*. 1990: Courier Corporation.
140. Hodgson, J.N., *Optical Absorption and Dispersion in Solids*. 2012: Springer Science & Business Media.

-
141. Demtröder, W., *Laser Spectroscopy Vol 2: Experimental Techniques*. 2008, Springer Nature.
142. Weiner, A.M., *Ultrafast Optics*. 2011: John Wiley & Sons, Inc.
143. Grancini, G., *Ultrafast Dynamics at Organic Interfaces for Photovoltaics*, in *Physics Department*. 2012, Politecnico di Milano.
144. Fischer, M.C., J.W. Wilson, F.E. Robles, and W.S. Warren, *Invited Review Article: Pump-probe microscopy*. *Review of Scientific Instruments*, 2016. **87**(3): p. 031101.
145. Calió, L., S. Kazim, M. Grätzel, and S. Ahmad, *Hole-Transport Materials for Perovskite Solar Cells*. *Angewandte Chemie International Edition*, 2016. **55**(47): p. 14522-14545.
146. de Jong, M.P., L.J. van Ijzendoorn, and M.J.A. de Voigt, *Stability of the interface between indium-tin-oxide and poly(3,4-ethylenedioxythiophene)/poly(styrenesulfonate) in polymer light-emitting diodes*. *Applied Physics Letters*, 2000. **77**(14): p. 2255-2257.
147. Bakr, Z.H., Q. Wali, A. Fakharuddin, L. Schmidt-Mende, T.M. Brown, and R. Jose, *Advances in hole transport materials engineering for stable and efficient perovskite solar cells*. *Nano Energy*, 2017. **34**: p. 271-305.
148. Zhang, Y., W. Liu, F. Tan, and Y. Gu, *The essential role of the poly(3-hexylthiophene) hole transport layer in perovskite solar cells*. *Journal of Power Sources*, 2015. **274**: p. 1224-1230.
149. Cui, Y., B. Xu, B. Yang, H. Yao, S. Li, and J. Hou, *A Novel pH Neutral Self-Doped Polymer for Anode Interfacial Layer in Efficient Polymer Solar Cells*. *Macromolecules*, 2016. **49**(21): p. 8126-8133.

150. Elumalai, N.K. and A. Uddin, *Open circuit voltage of organic solar cells: an in-depth review*. Energy & Environmental Science, 2016. **9**(2): p. 391-410.
151. Ullrich Pietsch, V.H., Tilo Baumbach, *High-Resolution X-Ray Scattering: From Thin Films to Lateral Nanostructures*. 2004: Springer Science & Business Media.
152. Wang, J., H. Shen, W. Li, S. Wang, J. Li, and D. Li, *The Role of Chloride Incorporation in Lead-Free 2D Perovskite (BA)₂SnI₄: Morphology, Photoluminescence, Phase Transition, and Charge Transport*. Advanced Science, 2019. **6**(5): p. 1802019.
153. Wang, A., Y. Guo, Z. Zhou, X. Niu, Y. Wang, F. Muhammad, H. Li, T. Zhang, J. Wang, S. Nie, and Z. Deng, *Aqueous acid-based synthesis of lead-free tin halide perovskites with near-unity photoluminescence quantum efficiency*. Chemical Science, 2019. **10**(17): p. 4573-4579.
154. Lanzetta, L., J.M. Marin-Beloqui, I. Sanchez-Molina, D. Ding, and S.A. Haque, *Two-Dimensional Organic Tin Halide Perovskites with Tunable Visible Emission and Their Use in Light-Emitting Devices*. ACS Energy Letters, 2017. **2**(7): p. 1662-1668.
155. Chen, K., P. Wu, W. Yang, R. Su, D. Luo, X. Yang, Y. Tu, R. Zhu, and Q. Gong, *Low-dimensional perovskite interlayer for highly efficient lead-free formamidinium tin iodide perovskite solar cells*. Nano Energy, 2018. **49**: p. 411-418.
156. Stoumpos, C.C., L. Mao, C.D. Malliakas, and M.G. Kanatzidis, *Structure–Band Gap Relationships in Hexagonal Polytypes and Low-Dimensional Structures of Hybrid Tin Iodide Perovskites*. Inorganic Chemistry, 2017. **56**(1): p. 56-73.

157. Ma, L., M.-G. Ju, J. Dai, and X.C. Zeng, *Tin and germanium based two-dimensional Ruddlesden–Popper hybrid perovskites for potential lead-free photovoltaic and photoelectronic applications*. *Nanoscale*, 2018. **10**(24): p. 11314-11319.
158. Singh, J., *Optical Properties of Condensed Matter and Applications*. 2006: John Wiley & Sons.
159. Sarritzu, V., N. Sestu, D. Marongiu, X. Chang, S. Masi, A. Rizzo, S. Colella, F. Quochi, M. Saba, A. Mura, and G. Bongiovanni, *Optical determination of Shockley-Read-Hall and interface recombination currents in hybrid perovskites*. *Sci Rep*, 2017. **7**: p. 44629.
160. Würfel, P., *The Physics of Solar Cells: From Principles to New Concepts*. 2008: John Wiley & Sons, Inc.
161. Nelson, J., *The Physics of Solar Cells*. 2003: Imperial College Press.
162. Würfel, P., *The chemical potential of radiation*. *Journal of Physics C: Solid State Physics*, 1982. **15**(18): p. 3967-3985.